

### 3.2.3 The Muon Spectrometer

The muon spectrometer [64] is the outermost part of ATLAS. It is a set of detector chambers that are designed to specifically detect and measure the position and momenta of muons passing through the ID and calorimeters. In addition to detection, it is also designed to trigger on particles. The muon spectrometer contains four different kinds of detectors as shown in Figure 3.14: the Monitored Drift Tube Chambers (MDT), the Resistive Plate Chambers (RPC), the Thin Gap Chambers (TGC) and the Cathode Strip Chambers (CSC).

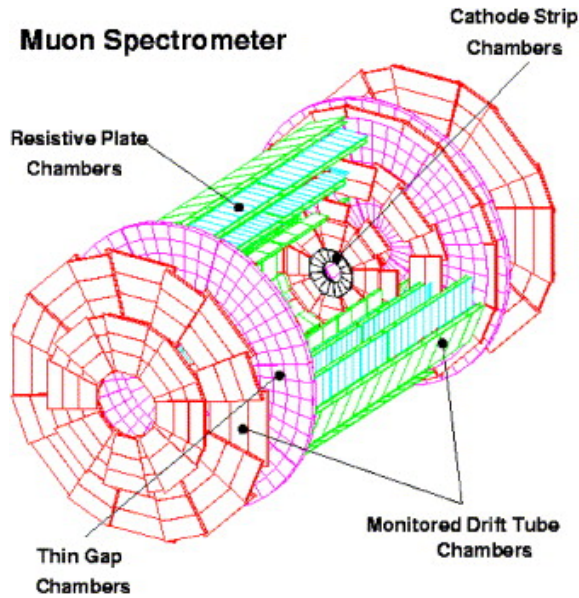


Figure 3.14: The detectors of the muon spectrometer [22].

For precision tracking in the barrel region, a combination of MDTs and RPCs are arranged in three concentric cylindrical shells around the beam pipe at radii of approximately 5 m, 7.5 m, and 10 m. The MDT chambers contain three to eight layers of 30 mm diameter, pressurized drift tubes operating with argon-CO<sub>2</sub> gas (93/7%) at 3 bar. The tube acts as the cathode and contains a 50 $\mu$ m gold-plated tungsten-rhenium wire which acts as the anode with a potential of 3 kV. Charged muons ionize the gas mixture in the tubes to create electrons (which are attracted to the wire) and

positive ions (which drift towards the cathode). The electrical signals obtained from the wire then provides information about the passing muon. Each MDT tube has a space resolution of  $80 \mu\text{m}$  and a time resolution of less than 1 ns. The RPCs consist of parallel electrode-plates made of phenolic-melaminic plastic laminate. Two resistive plates are separated by 2 mm using insulating spacers. The electric field between the plates allow electrical signals to form due to electron avalanches produced due to the ionizing muon tracks. They are kept at a potential difference of 9.8 kV and the chamber is filled with a gas mixture of  $\text{C}_2\text{H}_2\text{F}_4$ . The RPCs provide good time resolution (less than 2 ns) and are used to trigger on muons.

In the end-cap regions, the muon chambers are arranged in eight large wheels at distances of  $\pm 7.4 \text{ m}$ ,  $\pm 10.8 \text{ m}$ ,  $\pm 14 \text{ m}$ , and  $\pm 21.5 \text{ m}$  from the interaction point. The chambers used are the MDTs, the TGCs and the CSCs. The MDTs provide precision muon tracking and the TGCs provide muon trigger capabilities as well as the measurement of azimuthal coordinate to complement the MDT measurements. TGCs are multiwire proportional chambers filled with a highly quenching gas mixture of  $\text{CO}_2$  and  $n\text{-C}_5\text{H}_{12}$ . The wire-to-wire distance is 1.8 mm and the wire-to-cathode distance is 1.4 mm. These high voltage of the wires (2.9 kV) and the small distances between the wires and the cathode strips leads to a good time resolution of 4 ns. In the region of  $|\eta| < 2$ , the inner most wheels contain the CSC chambers. Like the TGCs, the CSC chambers are multiwire proportional chambers with wires running in the radial direction. The wires are kept at a voltage of 1.9 kV and are filled with a gas mixture of argon- $\text{CO}_2$  (80/20%). These chambers provide good tracking ( $60 \mu\text{m}$ ) and good timing resolution (less than 40 ns).

### 3.2.4 The Magnets

The ATLAS magnet system [65] provides magnetic fields over a volume of approximately  $12,000 \text{ m}^3$ . The magnetic fields bend charged particles, allowing their charge



and momentum to be measured. The magnet system consists of three large superconducting magnets: the barrel solenoid, the barrel toroid and the two end-cap toroid magnets. In total, the system stores 1.6 GJ of energy and is 22 m in diameter and 26 m in length.

The barrel solenoid magnet envelopes the ID and is surrounded by the EMB calorimeter. It is a single-layer coil made of 1,154 turns of 9 km of a high-strength aluminium-stabilized niobium-titanium conductor. It provides a 2 T axial field operating at a nominal current of approximately 7.7 kA. The thickness of its walls was optimized to be the smallest possible to reduce the amount of energy lost by particles entering the calorimeters. Figure 3.15 (a) shows the barrel solenoid magnet being inserted into the EMB calorimeter.

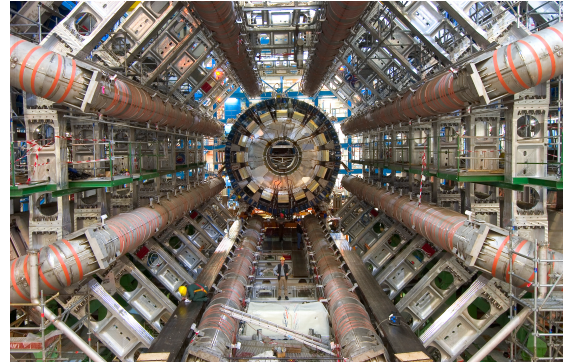
The volume surrounding the calorimeters and encasing the muon spectrometer is filled with magnetic fields produced by the barrel toroid magnet system. The system consists of eight coils encased in individual racetrack-shaped, stainless-steel vacuum vessels as shown in Figure 3.15 (b). Supported by eight inner and outer struts, the barrel toroid system is 25.3 m long with an inner and outer diameter of 9.4 m and 20.1 m respectively. The coils are made of 56 km of wound pure aluminium-stabilized niobium/titanium/copper conductor. Figure 3.15 (c) shows the transportation of one of the barrel toroid coils. The two end-cap toroids (one on each side of the detector) generate the magnetic field required for bending muons with high  $\eta$ . They are made using 13 km of the same conductor as the barrel toroids and are encased in an aluminium housing. Figure 3.15 (d) shows an encased and a non-encased end-cap toroid.

### 3.2.5 Trigger and Data Acquisition

Colliding proton bunches at a frequency of 40 MHz, the LHC produces approximately 1 billion collisions per second ( $40 \text{ million} \times \sim 25$  interactions per collision). Since it



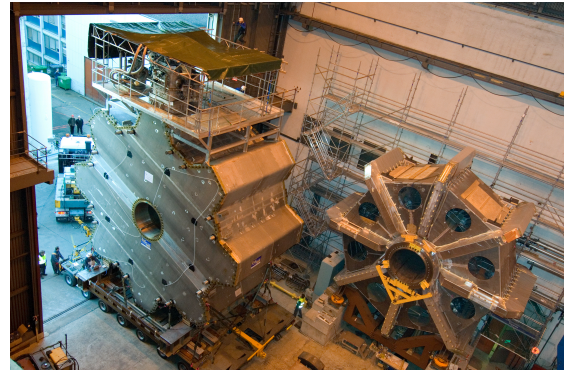
(a) The solenoid magnet



(b) The toroid magnet system



(c) Transporting a toroid magnet



(d) Moving the end-cap toroid magnet

Figure 3.15: (a) The solenoid magnet being inserted into the electromagnetic barrel calorimeter [23], (b) the installed toroidal magnet system [24], (c) transporting a toroid magnet [25], (d) transporting the end-cap toroid magnet [26].

is impossible to record all the collisions, there needs to be a system to filter out the uninteresting collisions<sup>5</sup> from the interesting ones. The ATLAS trigger system [66] is designed to do exactly this. It consists of a hardware-based trigger called Level-1 Trigger (L1) and a software-based trigger known as the High Level Trigger (HLT). The L1 trigger uses coarse-granularity calorimeter and muon detector information to determine Regions-of-Interest (RoIs) in the detector. It reduces the event rate from the LHC bunch crossing of 40 MHz to 100 kHz and makes a decision to keep or reject an event in  $2.5 \mu\text{s}$ . The RoIs are passed to the HLT which uses full-granularity detector information and sophisticated algorithms to further accept or reject events. It reduces the event rate from the L1 rate of 100 kHz to approximately 1 kHz and makes a decision in 200 ms.

The data retained by the trigger system amounts to approximately 1 petabyte per year. This data needs to be distributed efficiently across the world to thousands of physicists. This is done by the Worldwide LHC Computing Grid (WLCG) [67]. The WLCG is a global collaboration of over 170 computer centers spanning 41 countries. Figure 3.16 shows the WLCG connections across the world.

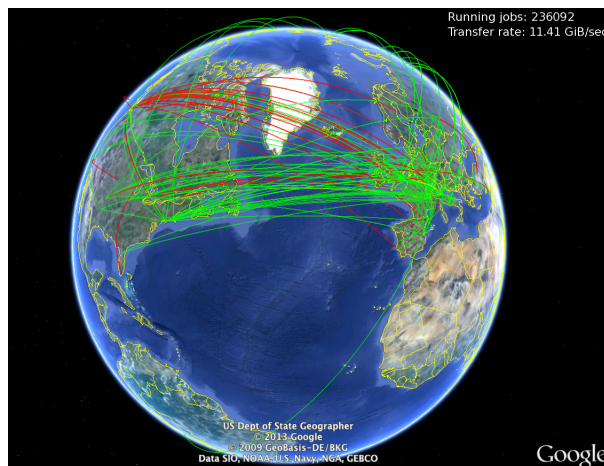


Figure 3.16: The Worldwide LHC Computing Grid connections across the earth [27].

The centers are arranged in four levels, or *Tiers*, known as 0, 1, 2 and 3. Tier 0 is

---

<sup>5</sup>These constitute the majority of the LHC collisions

the central hub through which all the data from the LHC passes and it is located at CERN. After the trigger system selects events, the Tier 0 is responsible for the first pass of reconstructing the raw data produced by the millions of digital readings from all the CERN detectors. The reconstruction involves creating energy clusters from the calorimeter cells and towers and tracks and vertices from space-time detector hits. The Tier 0 passes the raw and reconstructed data to the 13 Tier 1 centers across the world using optical-fiber links working at 10 gigabits per second. The Tier 1 sites are responsible for sharing, storing, processing and transmitted the data to the Tier 2 sites. The 155 Tier 2 sites are located at universities and scientific institutes and contribute to the further processing and storage of analysis-specific data as well as simulated data. At last there are the Tier 3 sites, through which scientists can access and analyze the LHC data via their computers and laptops.

## CHAPTER 4

# Measurement of Hadronic Jets in the ATLAS Detector

During the Large Hadron Collider's (LHC) high-energy proton-proton collisions, quarks and gluons are scattered out of the colliding protons. They are not observed directly, but materialize as collimated sprays of particles known as jets. Jets are the dominant objects arising from these collisions and they play a major role in understanding Standard Model (SM) processes and searching for new phenomena beyond the Standard Model (BSM). Thus, obtaining accurately measured and well-calibrated jets is of prime importance. This chapter will describe the reconstruction and calibration of jets in ATLAS.

### 4.1 Jet Production

The high energy partons (quarks and gluons) produced from the hard scattering collision at the interaction point instantaneously fragment into a cascade of multiple particles (as sketched in Figure 4.1). Due to color confinement, these particles recombine to form colorless hadrons (mostly  $\pi$  and  $K$  mesons). This process is known as *hadronization* and it occurs within  $10^{-15}$  m of the interaction point. At this stage, the collection of collimated hadrons are known as *hadron jets*. These jets cannot be measured experimentally as they have not yet encountered any material of the

detector. They are studied in MC simulations, where they are known as *truth jets*. As the hadron jets continue to travel outwards, they cross the multiple layers of the ID which record their tracks (only charged hadrons) in its three subdetector systems. Jets created from the tracks (with momenta from the ID measurements) are known as *track jets* and are mostly used for systematic studies and calibration. After the ID, the outgoing hadrons encounter the finely-segmented electromagnetic (ECal) and hadronic calorimeter (HCal), in which they deposit all of their energy by interacting with the material of the calorimeters. Jets created from the energy deposited in the calorimeter cells are known as *calorimeter jets* and are used for SM measurements and Beyond the Standard Model (BSM) searches. The dijet search presented in this thesis uses calorimeter jets. Their reconstruction and calibration will be discussed in detail next.

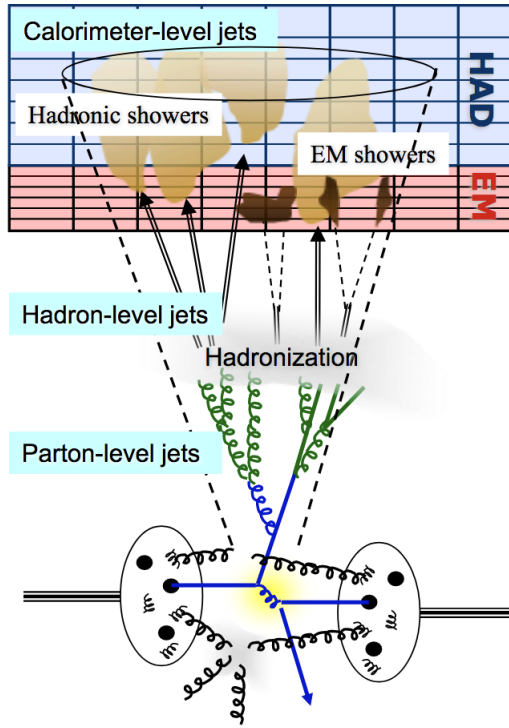


Figure 4.1: Jet production from a LHC proton-proton collision [28].

## 4.2 Jet Reconstruction

### 4.2.1 Topo-clusters

Calorimeter jets are formed by first combining several topologically adjacent calorimeter cell clusters into *topo-clusters* [68]. Topo-clusters are created to extract the energy of the relevant decay particles from a background of irrelevant collisions and electronic noise. They are formed by a growing-volume algorithm where neighboring cells are clustered around the most energetic cells (known as the seed cells). The algorithm starts by identifying seed cells as cells with electromagnetic energy ( $E_{\text{cell}}^{\text{EM}}$ ) larger than four times the average expected noise ( $\sigma_{\text{noise,cell}}^{\text{EM}}$ ) in the cell, i.e. seed cells have  $|E_{\text{cell}}^{\text{EM}}| > 4 \sigma_{\text{noise,cell}}^{\text{EM}}$ . The cell energy and noise are measured at the Electromagnetic (EM) energy scale, i.e. assuming that all incident particles are electromagnetically interacting. Each seed cell forms a *proto-cluster* and neighboring cells with  $|E_{\text{cell}}^{\text{EM}}| > 2 \sigma_{\text{noise,cell}}^{\text{EM}}$  are collected into each corresponding proto-cluster. The proto-clusters grow in size by further collecting neighbors of the neighboring cells and can span several calorimeter cells in the same layer or multiple layers. This process results in topo-clusters with high-energy core cells enveloped by cells of decreasing energy. Topo-clusters are characterized by four-vectors  $P_{\text{clus}}^{\text{EM}}$ , expressed as,

$$\begin{aligned} P_{\text{clus}}^{\text{EM}} &= E_{\text{clus}}^{\text{EM}}, p_{x,\text{clus}}^{\text{EM}}, p_{y,\text{clus}}^{\text{EM}}, p_{z,\text{clus}}^{\text{EM}} \\ &= E_{\text{clus}}^{\text{EM}}(1, \sin \theta_{\text{clus}} \cos \phi_{\text{clus}}, \sin \theta_{\text{clus}} \sin \phi_{\text{clus}}, \cos \theta_{\text{clus}}) \end{aligned} \quad (4.1)$$

where  $E_{\text{clus}}^{\text{EM}}$  is the geometrically weighted ( $w_{\text{cell}}^{\text{geo}}$ ) sum of cell energies,  $\theta_{\text{clus}}$  is the polar angle and  $\phi_{\text{clus}}$  is the azimuthal angle of the cluster. The polar angle is calculated from the pseudorapidity ( $\eta_{\text{clus}}$ ) of the cluster. Weighted by the geometric weights and cell energies, the energy, pseudo-rapidity and azimuthal angle of the cluster is defined



as the following,

$$E_{\text{clus}}^{\text{EM}} = \sum_{i=1}^{N_{\text{cell}}} w_{\text{cell},i}^{\text{geo}} \cdot E_{\text{cell},i}^{\text{EM}} \quad (4.2)$$

$$\eta_{\text{clus}} = \frac{\sum_{i=1}^{N_{\text{cell}}} w_{\text{cell},i}^{\text{geo}} \cdot |E_{\text{cell},i}^{\text{EM}}| \cdot \eta_{\text{cell},i}}{\sum_{i=1}^{N_{\text{cell}}} w_{\text{cell},i}^{\text{geo}} \cdot |E_{\text{cell},i}^{\text{EM}}|} \quad (4.3)$$

$$\phi_{\text{clus}} = \frac{\sum_{i=1}^{N_{\text{cell}}} w_{\text{cell},i}^{\text{geo}} \cdot |E_{\text{cell},i}^{\text{EM}}| \cdot \phi_{\text{cell},i}}{\sum_{i=1}^{N_{\text{cell}}} w_{\text{cell},i}^{\text{geo}} \cdot |E_{\text{cell},i}^{\text{EM}}|} \quad (4.4)$$

In  $\eta - \phi$  space, the distance between two topo-clusters is defined as,

$$R_{ij}^2 = (\eta_i - \eta_j)^2 + (\phi_i - \phi_j)^2 \quad (4.5)$$

## 4.2.2 Jet Clustering

After the topo-clusters are formed, they are clustered together to form jets. In order for the reconstructed jets to be well-defined at all orders of perturbation theory, the clustering algorithm needs to satisfy two conditions:

- Infrared safety: In the presence of soft radiation, i.e. gluon splitting, the clustering algorithm should always reconstruct the same number of jets in the event.
- Collinear safety: The splitting one parton into two partons should not change the results of the jet clustering.

Out of the various clustering algorithms that exist, ATLAS uses an Infrared-Collinear safe algorithm known as the *anti- $k_T$*  algorithm [29]. It is a sequential clustering algorithm that groups topo-clusters by combining their four-vectors. It works by defining two distance variables in momentum space:  $d_{ij}$  and  $d_{iB}$ . The former represents the distance between two topo-clusters  $i$  and  $j$ , and the latter the distance between the

beam axis and topo-cluster  $i$ . They are calculated as

$$d_{ij} = \min \left( \frac{1}{p_{Ti}^2}, \frac{1}{p_{Tj}^2} \right) \times \frac{R_{ij}^2}{R^2} \quad (4.6)$$

$$d_{iB} = \frac{1}{p_{Ti}^2}, \quad (4.7)$$

where  $p_T$  stands for the transverse momentum of a cluster and  $R$  is the radius parameter that determines the final size of the jet. The anti- $k_T$  algorithm works by first creating a list of  $d_{ij}$  for each pair combination of topo-clusters and  $d_{iB}$  for each topo-cluster. From the list  $(d_{ij}, d_{iB})$ , it identifies the pair of clusters with the smallest distance and if  $d_{ij} < d_{iB}$ , it combines the four-vectors of the two cluster into one four-vector. After removing these clusters from the list, it repeats the process for the next pair of clusters with the smallest distance. If at some point  $d_{iB} < d_{ij}$ ,  $i$  is called the final jet and is removed from the event. Continuing this way, all the clusters in an event are grouped into jets. As an example, figure 4.2 shows jets clustered using the anti- $k_T$  algorithm on a sample parton-level event with  $R = 1.0$ .

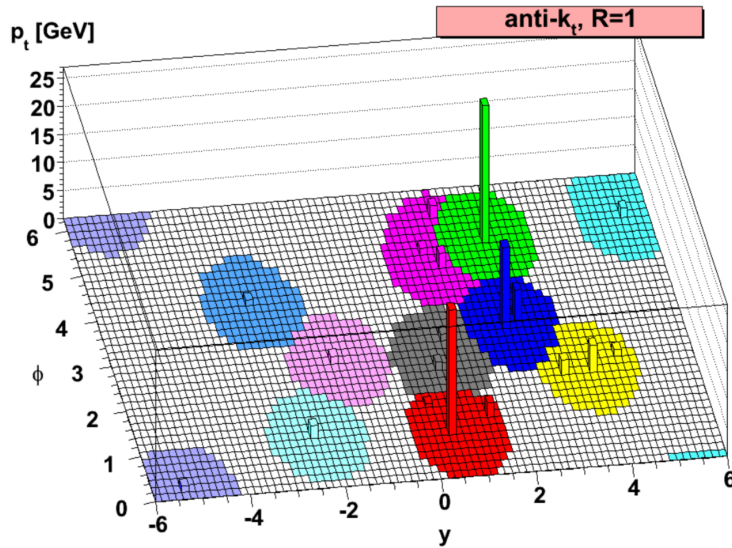


Figure 4.2: Jets produced using the anti- $k_T$  algorithm on a sample parton-level event using  $R = 1.0$ . [29].

Due to the  $1/p_T$  dependence in Equation 4.6, the anti- $k_T$  algorithm prefers to cluster high energy clusters first. This leads to well-defined jet boundaries that are resilient to the deformations due to emission of soft radiation. Thus, the anti- $k_T$  algorithm is ideal for clustering high energy jets and is used as the jet clustering algorithm for the analysis presented in this thesis. The radius parameter  $R$  is chosen to be 0.4.

## 4.3 Jet Calibration

After the jets are reconstructed at the EM scale, they are calibrated. The jet energy calibration restores the jet energy measured with the ATLAS calorimeters to the true energy of the corresponding jet (i.e. the truth jet) of stable particles entering the detector. It also corrects for the differences observed in the data and MC jet reconstruction. The truth jets for the various calibration stages are obtained from several MC simulations. They are reconstructed using the anti- $k_T$  algorithm with  $R = 0.4$  using final-state particles produced from MC generators as inputs.

As shown in Figure 4.3, the steps of the calibration procedure include origin correction, pile-up correction, absolute correction, global sequential correction and residual *in-situ* calibration. The first four steps use truth and reconstructed jets from MC simulation only. The last step uses both data and MC jets. At each stage of the calibration, corrections are applied to the full four-momenta of the reconstructed jets. The subsequent sections will detail each stage of the calibration procedure.

### 4.3.1 Origin Correction

After clustering, jets point to the center of the detector. However, they truly originate from the hard-scatter vertex which generally does not coincide with the detector center. The origin correction takes this difference into account by recalculating the

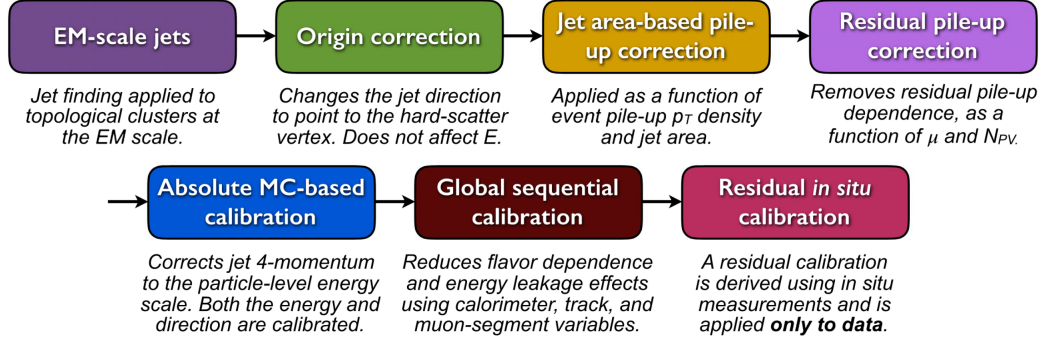


Figure 4.3: Calibration stages for EM-scale jets. [30].

four-momenta of the jets to point to the primary vertex instead of the detector center. The primary vertex is defined as the vertex that consists of the highest scalar sum of the transverse momentum square of tracks ( $\sum p_{T^2}(track)$ ) in an event and is considered to be the hard-scatter vertex. This correction changes the direction of the jet while keeping its energy constant. It improves the angular resolution of the jets.

### 4.3.2 Pile-up Corrections

The pile-up correction removes the excess energy of the jets due to in-time and out-of-time pile-up. It consists of two parts: the jet-area-based  $p_T$  density subtraction and a residual pile-up correction. For each event, the jet-area-based correction subtracts the pile-up contribution to the  $p_T$  of each jet according to its area,  $A$ . The area of a jet is calculated using ghost association where simulated “ghost” particles are added to an event before jet reconstruction. The area is then measured by the number of ghost particles contained in the jet. The pile-up contribution to the  $p_T$  of each jet is calculated from the median  $p_T$  density  $\rho$  of jets in the  $\eta - \phi$  plane with  $|\eta| < 2$ . As the area-based correction is derived from the central calorimeter region with lower occupancy, it does not correctly describe the pile-up levels in the forward calorimeter regions or the high-occupancy cores of high  $p_T$  jets. Hence, after this correction, a dependency of the jet  $p_T$  on the in-time pile-up and out-of-time pile-up is still

observed. To correct for this, a residual pile-up correction is applied. The effect of the two pile-up corrections on the jet  $p_T$  as a function of  $\eta$  is shown in Figure 4.4.

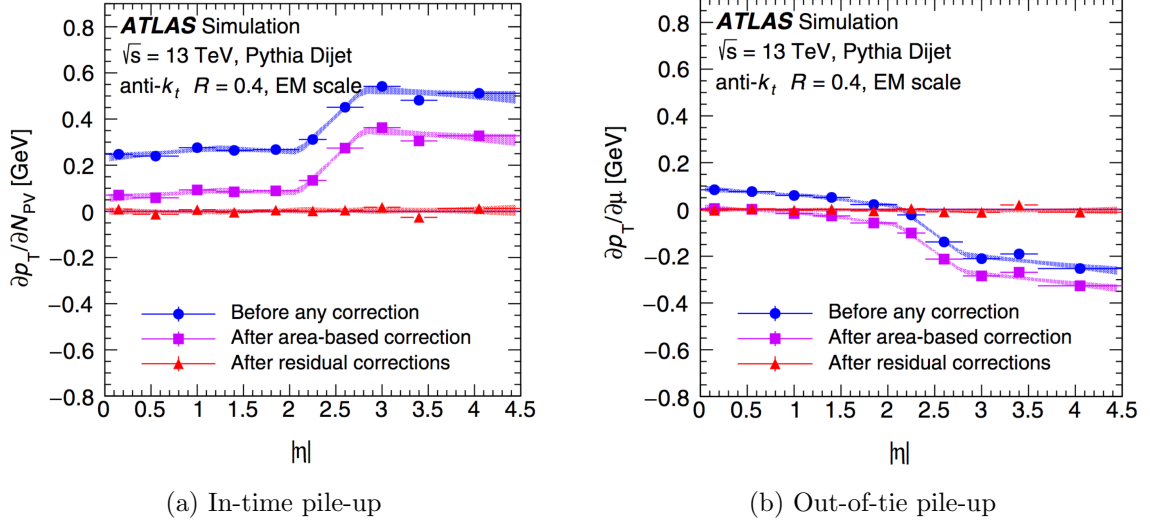


Figure 4.4: The dependence of EM-scale anti- $k_T$  jet  $p_T$  on (a) in-time pile up and (b) out-of-time pile-up as a function of  $\eta$  for  $p_T^{\text{truth}} = 25$  GeV. The blue dots show the dependence before the correction, the pink squares show the dependence after the area-based correction and the red triangles show the dependence after the residual correction.

### 4.3.3 Absolute MC-based Corrections

The absolute MC-based corrections consist of two components: the absolute Jet Energy Scale Jet Energy Scale (JES) and the  $\eta$  calibration correction. These corrections take into account differences caused by different detector granularities, transition regions between the different detector technologies, etc. They correct the reconstructed jet energy  $E^{\text{reco}}$  and pseudorapidity  $\eta^{\text{reco}}$  to the truth jet energy  $E^{\text{truth}}$  and pseudorapidity  $\eta^{\text{truth}}$  using correction factors derived from the PYTHIA [69] dijet MC simulation. PYTHIA is a particle collision simulation program that is capable of simulating hard and soft scatters, fragmentation, decays, multiple interactions and much more. The correction factors are calculated after the origin and pile-up corrections are applied.

The JES correction works by first geometrically matching isolated, reconstructed jets to truth jets within a distance of  $\Delta R = 0.3$ . The distribution of the ratio of the reconstructed energy  $E^{\text{reco}}$  and the truth energy  $E^{\text{truth}}$  is fit to a Gaussian function. The mean of the fit is called the average energy response and is calculated for different values of truth energy  $E^{\text{truth}}$  and detector  $\eta_{\text{det}}$ . Figure 4.5 (a) shows the energy response as a function of  $\eta_{\text{det}}$ . The dips and gaps seen at  $|\eta_{\text{det}}| \sim 1.4$  and  $|\eta_{\text{det}}| \sim 3.1$  show lower energy response due to absorbed or undetected particles in the detector transition regions. The  $|\eta_{\text{det}}| \sim 1.4$  and  $|\eta_{\text{det}}| \sim 3.1$  regions correspond to the barrel-endcap and endcap-forward transition regions respectively. The JES correction is then derived by numerically taking the inverse of the energy response [70].

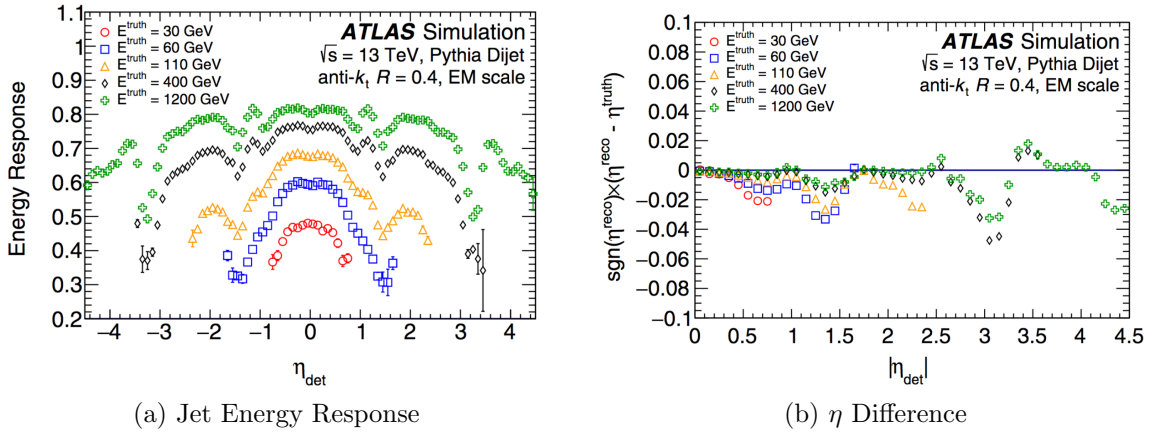


Figure 4.5: (a) The average energy response ( $E^{\text{reco}}/E^{\text{truth}}$ ) as a function of detector  $\eta_{\text{det}}$  in bins of  $E^{\text{truth}}$  is shown. (b) The difference between the truth jet  $\eta^{\text{truth}}$  and reconstructed jet  $\eta^{\text{reco}}$  is shown.

Figure 4.5 (b) shows a bias in the reconstructed jet  $\eta^{\text{reco}}$  as a function of  $\eta_{\text{det}}$ . Larger differences can be seen in the two transition regions again. To account for this difference, the  $\eta$  calibration correction is derived from the difference between the reconstructed  $\eta^{\text{reco}}$  and the truth  $\eta^{\text{truth}}$  as a function of  $\eta_{\text{det}}$ .

### 4.3.4 Global Sequential Calibration

After the preceding calibrations are applied, residual dependencies of the jet energy on the longitudinal and transverse features of the jet are observed. These are primarily caused by the difference in the initiating particle of the jet, i.e. quark-initiated vs gluon-initiated. To correct for these differences, a series of independent and sequential corrections are applied to the jet four-momentum based on a set of five observables. This set of five corrections is known as the Global Sequential Calibration (GSC) and it is derived as a function of  $p_T^{\text{truth}}$  and  $\eta_{\text{det}}$ . Like the JES correction factors, the GSC correction is calculated by inverting the reconstructed jet response for the five observables in MC events. The five observables are the following:

1.  $f_{\text{Tile0}}$ : the fraction of jet energy deposited in the first layer of the hadronic Tile calorimeter with  $|\eta_{\text{det}}| < 1.7$ ,
2.  $f_{\text{LAR3}}$ : the fraction of jet energy deposited in the third layer of the electromagnetic LAr calorimeter with  $|\eta_{\text{det}}| < 3.5$ ,
3.  $n_{\text{trk}}$ : the number of tracks with  $p_T > 1$  GeV associated with the jet with  $|\eta_{\text{det}}| < 2.5$ ,
4.  $W_{\text{trk}}$ : the average  $p_T$  weighted transverse distance in the  $\eta - \phi$  plane between the jet-axis and all the  $n_{\text{trk}}$  with  $|\eta_{\text{det}}| < 2.5$ ,
5.  $n_{\text{segments}}$ : the number of muon track segments associated to the jet with  $|\eta_{\text{det}}| < 2.7$ .

The effect of each correction is to remove the dependence of the jet response to each of the five observables while maintaining the mean energy response obtained in the JES correction stage. After the full GSC correction is applied, the dependence of the jet response on each observable is reduced to less than 2%.



### 4.3.5 Residual In-situ Calibration

The last stage of the jet calibration procedure is known as the residual in-situ calibration and it accounts for the differences in the jet response between the data and MC simulation. The calibration is derived by balancing the  $p_T$  of a jet against a well-measured reference object in data and MC and is defined as,

$$c = \frac{\mathcal{R}_{\text{data}}}{\mathcal{R}_{\text{MC}}} = \frac{\langle \frac{p_T^{\text{jet}}}{p_T^{\text{ref}}} \rangle_{\text{data}}}{\langle \frac{p_T^{\text{jet}}}{p_T^{\text{ref}}} \rangle_{\text{MC}}} \quad (4.8)$$

The in-situ calibration consists of four stages, each of which is derived and applied sequentially, with systematic uncertainties propagating through the procedure. The four stages (in order) are: the  $\eta$  intercalibration, the  $Z$ +jet balance, the  $\gamma$ +jet balance and the multijet balance.

The  $\eta$  intercalibration corrects the response of the forward jets ( $0.8 < |\eta_{\text{det}}| < 4.5$ ) to the well measured central jets ( $|\eta_{\text{det}}| < 0.8$ ) using dijet events. Using the central jet as the reference jet and the forward jet as the probe jet, the correction is obtained from the  $p_T$  responses of the jets in data and MC as a function of  $p_T$  and  $\eta_{\text{det}}$ . Figure 4.6 (a) and (b) show the relative  $p_T$  jet response of the two jets from data and two MC simulation samples. The data was collected in 2015 and 2016 and the two MC generators used are POWHEG+PYTHIA [69, 71] and SHERPA [72], where the former is used as the nominal MC generator and the latter is used to derive the systematic uncertainty associated to this correction.

The  $Z/\gamma$ +jet balance calibration uses well-calibrated  $Z$  bosons or photons to measure the  $p_T$  response of the recoiling jet with  $|\eta| < 0.8$ . Due to the excellent reconstruction of leptons,  $Z$  bosons decaying into pairs of muons and electrons are used for the  $Z$ +jet balance. The calibration is obtained in a  $p_T$  range of 20 to 500 GeV. For the  $\gamma$ +jet balance, the well-measured photon is balanced against the recoiling jet and the calibration is derived for a range of  $36 < p_T < 950$  GeV.

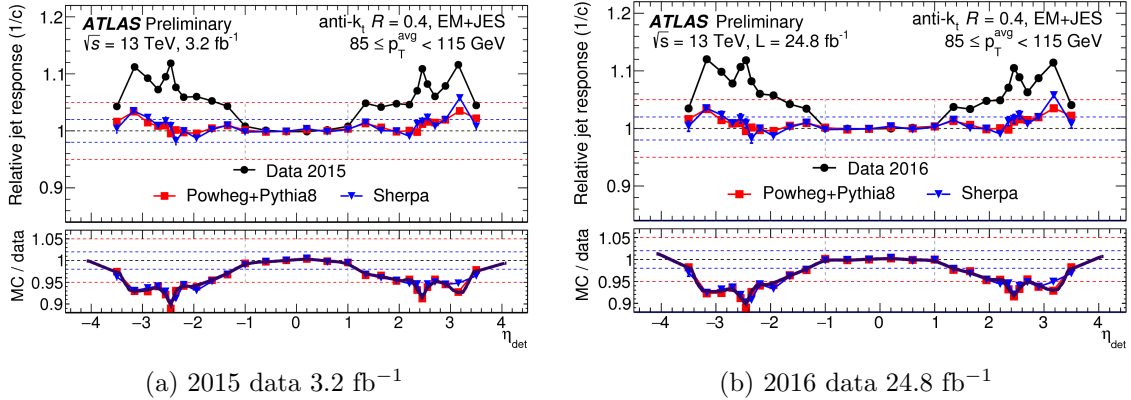


Figure 4.6: Jet response of reference and probe jets during the  $\eta$  intercalibration as a function of detector  $\eta_{\text{det}}$  for  $85 < p_T^{\text{average}} < 115$  GeV for (a) 2015 data [31] and (b) 2016 data [32].  $p_T^{\text{average}}$  is the average transverse momentum of the reference and probe jets.

To extend the calibration region up to 2 TeV, the multijet balance calibration is performed. Events with multiple jets are used and a high  $p_T$  jet is balanced against a recoil system composed of several low- $p_T$  jets. The leading jet in each event is taken to be the high  $p_T$  jet and it calibrated up to the  $\eta$  intercalibration level. The recoil system is obtained by summing the four-vectors of all the subleading jets, which are fully calibrated up to the  $Z/\gamma$ +jet balance level. This process is repeated iteratively where each newly calibrated high- $p_T$  jet is used to calibrate even higher  $p_T$  jets.

The data/MC ratio and its uncertainties for the  $Z$ +jet,  $\gamma$ +jet and multijet balance calibrations are combined over the  $p_T$  regions. They are reproduced with finer  $p_T$  binning by interpolating second-order polynomial spline fits as shown in Figure 4.7. The inverse of the data/MC ratio is taken to be the in-situ correction and is applied to the data.

#### 4.3.6 Systematic Uncertainties on the Jet Calibration

After the jet calibration is performed, its systematic uncertainties are evaluated. This amounts to a total of 80 uncertainties as summarized in Table 4.1 out of which the

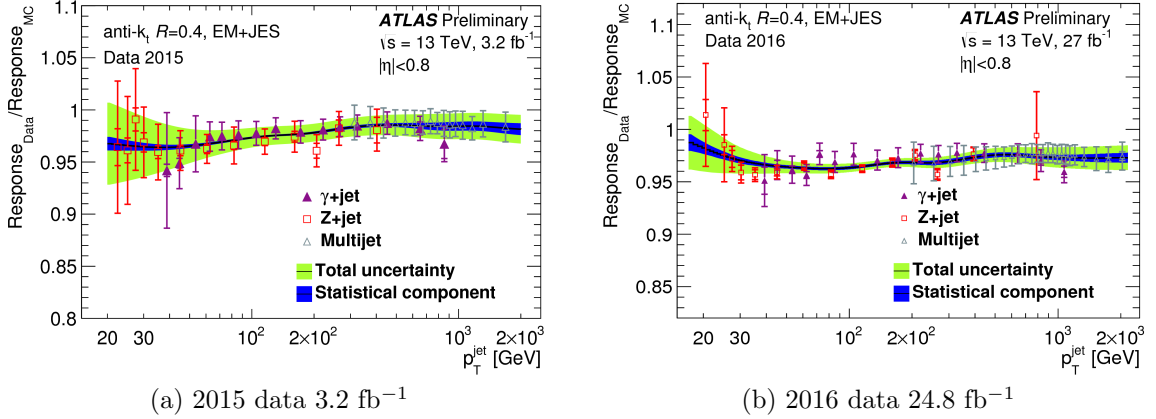


Figure 4.7: Ratio of the EM+JES jet response in 2015 and 2016 data to that in the MC simulation as a function of jet  $p_T$  for the combined *in situ* calibrations:  $Z$ +jet,  $\gamma$ +jet and multijet balance. The combined correction is shown by the black line and the green and blue bands are its total and statistical uncertainties respectively.

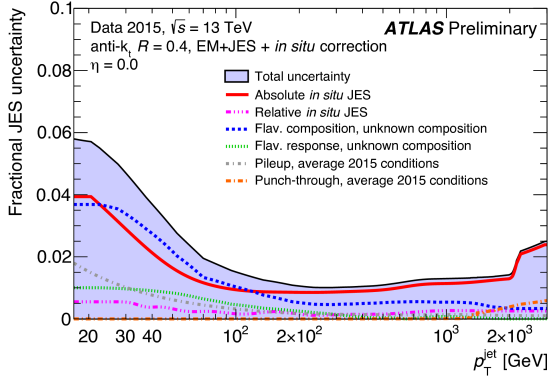
in-situ calibrations ( $Z/\gamma$ +jet, multijet) make up the majority (67). The remaining 13 originate from various other sources: three from  $\eta$  intercalibration, four from pile-up calibrations, three from jet flavor, one from the global sequential calibration (GSC) punch-through correction, one from the Atlfast-II (AFII) MC generator [73] samples and the last one from the single-particle response. The jet flavor uncertainties take into account the differences in jet response of gluon-initiated jets and b-quark initiated jets. They also assign an uncertainty to the flavor composition of the jet, i.e. gluon-initiated or quark-initiated. This uncertainty is derived from MC simulations and is either analysis-dependent or is taken to be 100% with 50% quark and 50% gluon initiated jets. AFII stands for Atlfast-II and it is a fast and full detector simulation technique that is used for fast MC simulation production. The AFII uncertainty accounts for the differences in the JES calibration of AFII sample jets and is only applied to the AFII samples. The last uncertainty is obtained from single-particle response studies [74] where the calorimeter response to isolated charged hadrons is studied. The estimates on the response of single particles is used to derive the response of high- $p_T$  jets (past 2 TeV) and an uncertainty on this is derived.

Table 4.1: List of systematic uncertainties in the JES calibration.

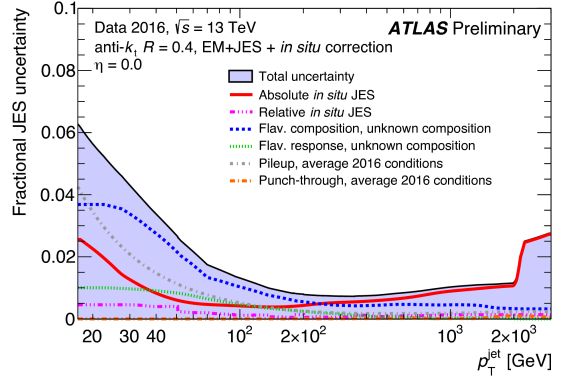
Name	Description
<b>Z + jet</b>	
Electron scale	Uncertainty in the electron energy scale
Electron resolution	Uncertainty in the electron energy resolution
Muon scale	Uncertainty in the muon momentum scale
Muon resolution (ID)	Uncertainty in muon momentum resolution in the ID
Muon resolution (MS)	Uncertainty in muon momentum resolution in the MS
MC generator	Difference between MC event generators
JVT	Jet vertex tagger uncertainty
$\Delta\phi$	Variation of $\Delta\phi$ between the jet and Z boson
2nd jet veto	Radiation suppression through second-jet veto
Out-of-cone	Contribution of particles outside the jet cone
Statistical	Statistical uncertainty over 13 regions of jet $p_T$
<b><math>\gamma</math> + jet</b>	
Photon scale	Uncertainty in the photon energy scale
Photon resolution	Uncertainty in the photon energy resolution
MC generator	Difference between MC event generators
JVT	Jet vertex tagger uncertainty
$\Delta\phi$	Variation of $\Delta\phi$ between the jet and $\gamma$
2nd jet veto	Radiation suppression through second-jet veto
Out-of-cone	Contribution of particles outside the jet cone
Photon purity	Purity of sample in $\gamma$ + jet balance
Statistical	Statistical uncertainty over 15 regions of jet $p_T$
<b>Multijet balance</b>	
$\alpha^{\text{MJB}}$ selection	Angle between leading jet and recoil system
$\beta^{\text{MJB}}$ selection	Angle between leading jet and closest subleading jet
MC generator	Difference between MC event generators
$p_T^{\text{asymmetry}}$ selection	Second jet's $p_T$ contribution to the recoil system
Jet $p_T$ threshold	Jet $p_T$ threshold
Statistical components	Statistical uncertainty over 16 regions of $p_T^{\text{leading}}$
<b><math>\eta</math>-intercalibration</b>	
Physics mismodeling	Envelope of the MC, pile-up, and event topology variations
Nonclosure	Nonclosure of the method in the $2.0 <  \eta_{\text{det}}  < 2.6$ region
Statistical component	Statistical uncertainty
<b>Pile-up</b>	
$\mu$ offset	Uncertainty of the $\mu$ modeling in MC simulation
$N_{\text{PV}}$ offset	Uncertainty of the $N_{\text{PV}}$ modeling in MC simulation
$\rho$ topology	Uncertainty of the per-event $p_T$ density modeling in MC simulation
$p_T$ dependence	Uncertainty in the residual $p_T$ dependence
<b>Jet flavor</b>	
Flavor composition	Uncertainty in the jet composition between quarks and gluons
Flavor response	Uncertainty in the jet response of gluon-initiated jets
$b$ -jet	Uncertainty in the jet response of $b$ -quark-initiated jets
Punch-through	Uncertainty in GSC punch-through correction
AFII non-closure	Difference in the absolute JES calibration using AFII
Single-particle response	High- $p_T$ jet uncertainty from single-particle and test-beam measurements

Figure 4.8 shows the full combination of all the JES uncertainties for the 2015 and 2016 data, first as a function of  $p_T$  for  $\eta = 0$  and second as a function of  $\eta$  for  $p_T = 60$  GeV. The 80 uncertainties are combined into 6 groups and are shown by the different colored lines. The uncertainties that contribute most to the combination as a function of  $p_T$  are the absolute in-situ JES uncertainty in red and the flavor composition uncertainty in blue. For the 2016 data, the pile-up uncertainty increases by a factor of two at lower  $p_T$  values due to the doubling of the average pile-up observed. The absolute in-situ JES uncertainty includes the  $Z/\gamma$ +jet, multijet and single particle uncertainties. It is high at low  $p_T$  and high again at high  $p_T$  due to statistical uncertainties associated to the in-situ calibration and it sharply increases past 2 TeV due to the contribution of the single particle uncertainty. As a function of  $\eta$ , the uncertainties that contribute the most are the flavor composition uncertainty in blue and the relative *in situ* JES uncertainty in pink. The relative *in situ* JES uncertainty represents the  $\eta$  intercalibration uncertainty and it spikes in the region of  $2.0 < |\eta| < 2.6$ . This is due to the residual  $\eta$  intercalibration difference that remains after the calibration is applied to jets, due to the non-perfect jet reconstruction in the calorimeter transition regions.

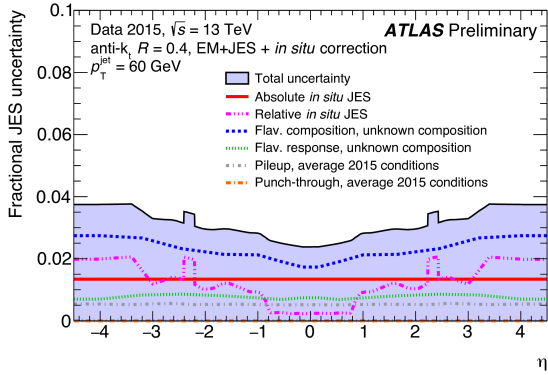
Even though the set of the 80 uncertainties fully describe the JES uncertainty, it is hard for jet analyses to take them all into account by introducing 80 variables while searching for new physics. In addition to the difficulty of handling a vast number of variables, not all uncertainties have equal weight, i.e. out of the 80 uncertainties, a certain portion would drive the overall JES uncertainty. Taking these points into account, the full set of uncertainties is reduced to four sets of strongly reduced Nuisance Parameter (NP)s that preserve as precisely as possible the bulk of the correlations across jet  $p_T$  and  $\eta$ . This reduction occurs in two steps. First the 67 *in situ* uncertainties are reduced to 6 uncertainties by diagonalizing the correlation matrix. Then, the remaining 19 uncertainties (6 reduced *in situ* and 13 others) are reduced to four



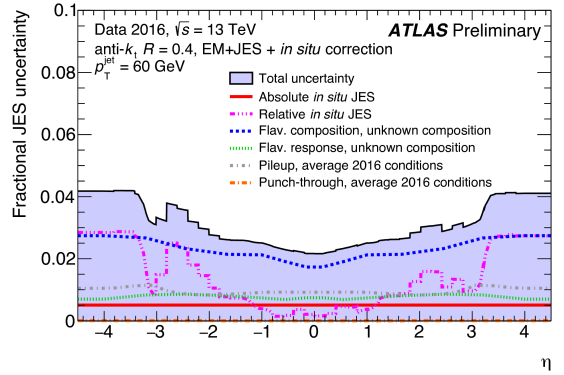
(a) 2015 data  $3.2 \text{ fb}^{-1}$  as a function of  $p_T$



(b) 2016 data  $24.8 \text{ fb}^{-1}$  as a function of  $p_T$



(c) 2015 data  $3.2 \text{ fb}^{-1}$  as a function of  $\eta$



(d) 2016 data  $24.8 \text{ fb}^{-1}$  as a function of  $\eta$

Figure 4.8: The combined JES uncertainties as a function of  $p_T$  (a, b) and  $\eta$  (c, d) for 2015 and 2016 data. The individual uncertainties are combined into 6 groups and are shown by the different colored lines.

NPs by combining the uncertainties in different ways (in different  $p_T$  and  $\eta$  regions) while minimizing the correlation loss.

In the analysis presented in this thesis, the first strongly-reduced NP combination is used to account for the JES uncertainty. This choice was made after confirming the negligible effect on signal limits produced by using the four different NPs.



## CHAPTER 5

# The Two Jet Final State: Standard Model Prediction and New Physics

This chapter will open the curtains to the search for new phenomena decaying to two jets. Before discussing the signatures for new phenomena, it is crucial to understand the Standard Model (SM) distribution (the background) over which these new phenomena would emerge. Hence, after defining some kinematic variables, the production of the SM dijet background is discussed. After this, the signature for new phenomena, i.e. the appearance of narrow structures over the smooth background, is detailed with emphasis on excited quarks ( $q^*$ ) and heavy gauge bosons ( $W'$ ). The use of Gaussian shapes to model any new physics signals is also described. The search results for  $q^*$  and  $W'$  from past dijet analyses are also summarized. Following this, the “traditional” dijet analysis strategy and the challenges it faces are discussed.

### 5.1 Standard Model Dijet Production

Jets are by far the most common product of energetic proton collisions. The vast majority are produced via the strong force (QCD) through  $2 \rightarrow 2$  parton interactions i.e. two incoming particles collide and interact and produce two outgoing particles. This results in the production of a large number of two-jet events, known as dijet events. Before discussing the dijet cross-section and kinematics in detail, some discussion

about variables that are useful to describe  $2 \rightarrow 2$  scattering is in order.

As discussed in Chapter 2, the scattering of two partons from the colliding hadrons produces two outgoing partons that experimentally appear as jets. This relatively simple two-body relativistic system is shown in Figure 5.1 and can be written as

$$p_1 + p_2 \rightarrow p_3 + p_4, \quad (5.1)$$

where  $p_1, p_2$  are the four-momenta of the two incoming partons and  $p_3, p_4$  are the four-momenta of the two outgoing partons. The four-momenta of the four partons fully characterizes the system. In terms of the energy ( $E$ ) and momenta ( $\vec{p}$ ) of each parton, it can be expressed as

$$P = (E, \vec{p}) = (E, p_x, p_y, p_z). \quad (5.2)$$

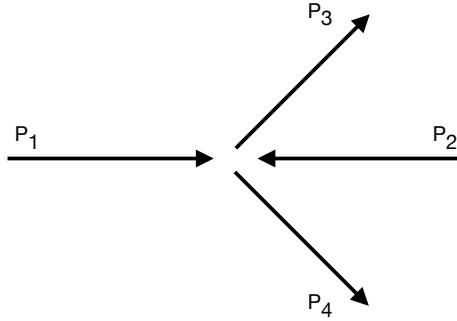


Figure 5.1: A dijet event. The incoming partons have four-momenta  $P_1$  and  $P_2$  and the outgoing jets have four-momenta  $P_3$  and  $P_4$ .

The center of mass frame of the parton-parton scattering is generally boosted, i.e. it has some momentum along the longitudinal axis (parallel to the beam-pipe). This occurs due to the unequal momenta of the two incoming partons. Thus, it is convenient to define the four-momenta in terms of variables that transform simply under longitudinal boosts. These variables are the rapidity  $y$ , the azimuthal angle  $\phi$  and the transverse momentum  $p_T$ . The transverse momentum is the component of

the parton's momentum perpendicular to the beam pipe. In terms of the polar angle  $\theta$ , it is defined as,  $p_T = p \sin \theta$ . Similarly, the longitudinal momentum is parallel to the beam pipe,  $p_L = p \cos \theta$ . In terms of these variables, the four-momenta of each parton can be written as

$$P = (E, p_x, p_y, p_z) \quad (5.3)$$

$$= (m_T \cosh y, p_T \sin \phi, p_T \cos \phi, m_T \sinh y), \quad (5.4)$$

where  $m_T$  is the transverse mass and is defined as  $m_T = \sqrt{p_T^2 + m^2}$ .

The information about the energy and momentum of the partons can be encoded in Lorentz-invariant variables known as the Mandelstam variables. These are

$$\hat{s} = (p_1 + p_2)^2 \quad (5.5)$$

$$\hat{t} = (p_1 - p_3)^2 \quad (5.6)$$

$$\hat{u} = (p_2 - p_3)^2.$$

These variables also serve as labels for Feynman diagrams that show the three ways in which two partons can interact. As seen in Figure 5.2, these are the *s-channel*, *t-channel* and the *u-channel*.

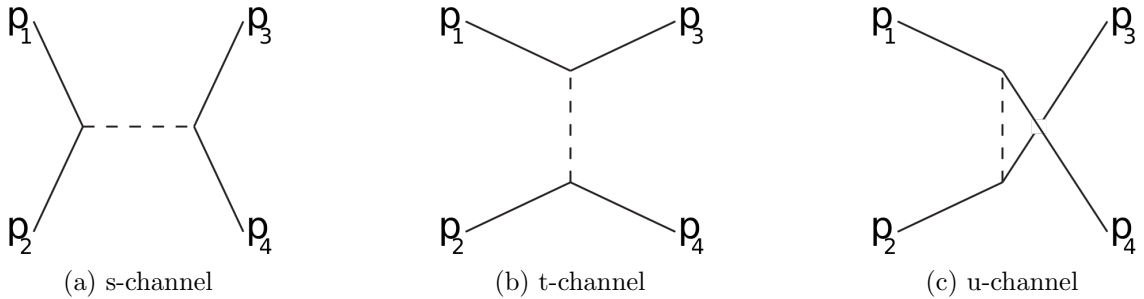


Figure 5.2: Feynman diagrams for the three ways in which two partons can interact at leading-order [33–35].

The s-channel diagram represents the annihilation of the two incoming partons

(partons 1 and 2) to an intermediate (also known as virtual) particle that decays into two outgoing partons (partons 3 and 4). This is the sole process responsible for the production of resonance phenomena, both known and unknown. The t-channel channel diagram represents the scattering process where one incoming parton (e.g. 1) emits a virtual particle and converts to an outgoing parton (e.g. 3). The virtual particle is absorbed by parton 2 that then converts to parton 4. The u-channel process is the same as the t-channel process but with the outgoing partons exchanged. The t- and u-channel processes are responsible for most of the QCD dijet events that represent the background for searches for new resonance phenomena.

### 5.1.1 Dijet Kinematics

All of dijet experimental variables of interest can be derived from the four-momenta of the two outgoing jets. The most important variables are the angular variable  $y^*$ , the center-of-mass boost variable  $y_B$  and the dijet invariant mass  $m_{jj}$ .

The angular separation of the two jets is measured by  $y^*$ . It is defined in terms of the rapidities  $y_3$  and  $y_4$  of the two jets as following

$$y^* = \frac{y_3 - y_4}{2}. \quad (5.7)$$

It is a Lorentz-invariant quantity (i.e. the same in all inertial frames) for boosts in the z-direction and is related to the scattering angle  $\theta^*$  in the center-of-mass frame by  $\theta^* = \tanh y^*$ . In the center-of-mass frame the rapidities of the jets are  $\pm y^*$ .

In a collision, the interacting partons generally have different momenta. The imbalance in the longitudinal momenta gives rise to a longitudinal boost with respect

to the lab frame. This boost is known as  $y_B$  and is defined as

$$\begin{aligned} y_B &= \frac{y_3 + y_4}{2} \\ &= \frac{1}{2} \ln \left( \frac{x_1}{x_2} \right), \end{aligned} \tag{5.8}$$

where  $x_1$  and  $x_2$  are the longitudinal momentum fractions of the incoming partons.

The most important dijet variable is the dijet invariant mass  $m_{jj}$ . It is calculated by taking the square root of the magnitude of the sum of the four vectors of the two jets

$$m_{jj} = \sqrt{(E_3 + E_4)^2 - |\vec{p}_3 + \vec{p}_4|^2}, \tag{5.9}$$

where  $E_3, \vec{p}_3$  and  $E_4, \vec{p}_4$  are the energy and momentum of the two outgoing jet. Like  $y^*$ , it is a Lorentz-invariant quantity and can also be expressed as

$$m_{jj} = \sqrt{\hat{s}} = 2 p_T \cosh y^*. \tag{5.10}$$

### 5.1.2 Dijet Cross-Section

The cross-section (denoted by  $\sigma$ ) is a constant of proportionality that gives the number of events ( $N$ ) as a function of integrated luminosity  $\int \mathcal{L} dt$ :

$$N = \sigma \int \mathcal{L} dt. \tag{5.11}$$

It is measured in units of area called barns ( $1 \text{ barn} = 10^{-24} \text{ cm}^2$ ) and for two interacting particles, it represents the probability of a scattering interaction between them. Classically, the cross-section provides a measure of the area transverse to the motion of the particles. When a cross-section is defined as a function of some variable, such as the mass or angle, it is known as a *differential cross-section*. By integrating the

differential cross-section over the variable (or variables incase of multiple variables), a *total cross-section* is obtained.

The double-differential cross-section for dijet production as a function of  $m_{jj}^2$  and  $\cos \theta^*$  can be written as

$$\frac{d^2\sigma}{dm_{jj}^2 d\cos\theta^*} = \sum_{i,j=q,\bar{q},g} \int_0^1 dx_1 dx_2 f_i(x_1, \mu^2) f_j(x_2, \mu^2) \delta(x_1 x_2 s - m_{jj}^2) \frac{d\hat{\sigma}^{ij}}{d\cos\theta^*}, \quad (5.12)$$

with

$$\frac{d\hat{\sigma}^{ij}}{d\cos\theta^*} = \sum_{k,l} \frac{1}{32\pi m_{jj}^2} \overline{|\mathcal{M}(ij \rightarrow kl)|^2} \frac{1}{1 + \delta_{kl}}, \quad (5.13)$$

where  $i, j, k$  and  $l$  are labels for partons 1, 2, 3 and 4 respectively. The angle  $\theta^*$  represents the scattering angle in the center-of-mass frame. Partons 3 and 4 are reconstructed as the two jets with mass  $m_{jj}$  and angular separation  $y^*$ . The hard-scattering cross-section  $\hat{\sigma}$  is described by a matrix element  $\mathcal{M}$  that encodes the transition probability of all  $ij \rightarrow kl$  processes.  $\overline{|\mathcal{M}^2|}$  represents averaging and summing the square of the matrix-element over the initial- and final-state spins and colors, respectively. The Kronecker delta function  $\delta$  inside  $\hat{\sigma}$  accounts for identical final state partons. Since the incoming partons carry a fraction of the parent proton's momenta ( $x_1$  and  $x_2$ ), their energy is  $\sqrt{x_1 x_2 s}$ . Thus, the delta function  $\delta(x_1 x_2 s - m_{jj}^2)$  selects initial states that produce events with the specified  $m_{jj}$ .

The leading-order Feynman diagrams that contribute to  $\mathcal{M}$  can be obtained from those shown in Figure 5.3. In terms of the Mandelstam variables, the expressions for  $\overline{|\mathcal{M}^2|}$  for various diagrams can be seen in Table 5.1. To demonstrate the relative importance of the diagrams, the last column of the table shows their values ( $\hat{\theta}$ ) for the following conditions:  $\theta^* = \pi/2$ ,  $\hat{t} = \hat{u} = -\hat{s}/2$ . They are calculated using the

following relation between the Mandelstam variables and  $\theta^*$ :

$$\begin{aligned}\hat{t} &= -\frac{1}{2}\hat{s}(1 - \cos \theta^*) \\ \hat{u} &= -\frac{1}{2}\hat{s}(1 + \cos \theta^*).\end{aligned}\tag{5.14}$$

The most important dijet production processes are  $gg \rightarrow gg$ ,  $qg \rightarrow qg$  and  $q\bar{q} \rightarrow q\bar{q}$ .

The differential cross-section as a function of  $\cos \theta^*$  for each of these processes is

$$\frac{d\hat{\sigma}^{ij}}{d \cos \theta^*} \sim \frac{1}{\sin^4(\theta^*/2)}.\tag{5.15}$$

This is nothing but the Rutherford scattering behavior at small angles that characterizes the exchange of a massless vector bosons in the t-channel.

Table 5.1: The matrix element squared expressions and values  $\hat{\theta}$  (evaluated for  $\theta^* = \pi/2$ ,  $\hat{t} = \hat{u} = -\hat{s}/2$ ) for dijet processes. The color and spin indices are averaged and summed over respectively. [36]

Process	$\overline{\sum}  \mathcal{M} ^2 / g^4$	$\hat{\theta}$
$qq' \rightarrow qq'$	$\frac{4}{9} \frac{\hat{s}^2 + \hat{u}^2}{\hat{t}^2}$	2.22
$q\bar{q}' \rightarrow q\bar{q}'$	$\frac{4}{9} \frac{\hat{s}^2 + \hat{u}^2}{\hat{t}^2}$	2.22
$qq \rightarrow qq$	$\frac{4}{9} \left( \frac{\hat{s}^2 + \hat{u}^2}{\hat{t}^2} + \frac{\hat{s}^2 + \hat{t}^2}{\hat{u}^2} \right) - \frac{8}{27} \frac{\hat{s}^2}{\hat{u}\hat{t}}$	3.26
$q\bar{q} \rightarrow q'\bar{q}'$	$\frac{4}{9} \frac{\hat{t}^2 + \hat{u}^2}{\hat{s}^2}$	0.22
$q\bar{q} \rightarrow q\bar{q}$	$\frac{4}{9} \left( \frac{\hat{s}^2 + \hat{u}^2}{\hat{t}^2} + \frac{\hat{t}^2 + \hat{u}^2}{\hat{s}^2} \right) - \frac{8}{27} \frac{\hat{u}^2}{\hat{s}\hat{t}}$	2.59
$q\bar{q} \rightarrow gg$	$\frac{32}{27} \frac{\hat{t}^2 + \hat{u}^2}{\hat{t}\hat{u}} - \frac{8}{3} \frac{\hat{t}^2 + \hat{u}^2}{\hat{s}^2}$	1.04
$gg \rightarrow q\bar{q}$	$\frac{1}{6} \frac{\hat{t}^2 + \hat{u}^2}{\hat{t}\hat{u}} - \frac{3}{8} \frac{\hat{t}^2 + \hat{u}^2}{\hat{s}^2}$	0.15
$gq \rightarrow gq$	$-\frac{4}{9} \frac{\hat{s}^2 + \hat{u}^2}{\hat{s}\hat{u}} + \frac{\hat{u}^2 + \hat{s}^2}{\hat{t}^2}$	6.11
$gg \rightarrow gg$	$\frac{9}{2} \left( 3 - \frac{\hat{t}\hat{u}}{\hat{s}^2} - \frac{\hat{s}\hat{u}}{\hat{t}^2} - \frac{\hat{s}\hat{t}}{\hat{u}^2} \right)$	30.4



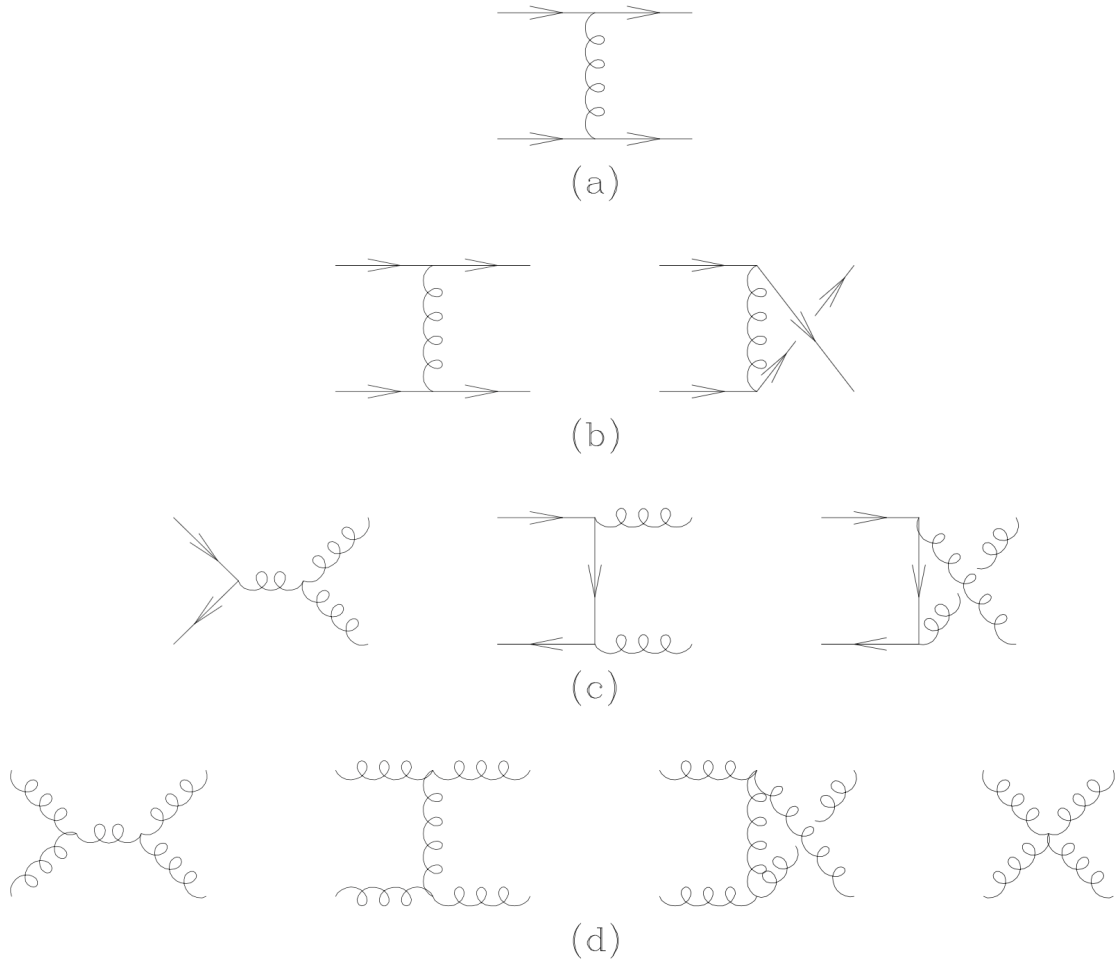


Figure 5.3: Leading-order Feynman diagrams for dijet production [36].

Figure 5.4 shows a comparison of the measured double differential dijet cross-section with respect to next-to-leading order (NLO) perturbative QCD predictions [37]. It is shown as a function of  $m_{jj}$  and  $y^*$  for anti- $k_T$  jets with  $R = 0.4$ . The shaded grey areas show the experimental systematic uncertainties and the yellow boxes represent the theoretical predictions with their uncertainties. In general, the agreement between the data and prediction is quite good.

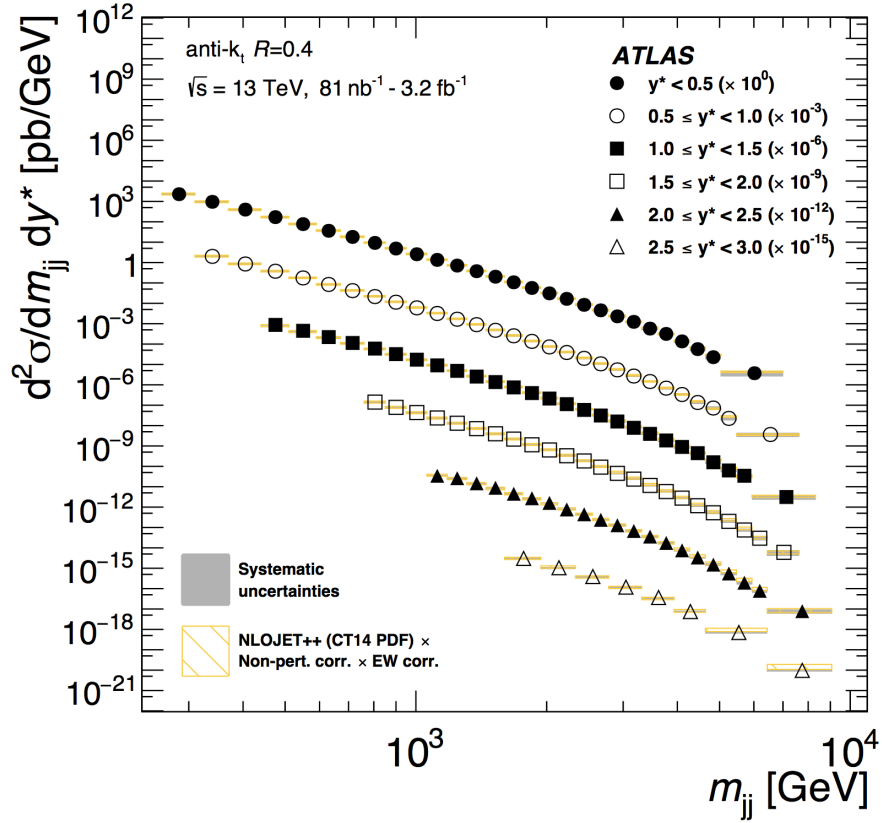


Figure 5.4: Dijet cross-section as a function of  $m_{jj}$  and  $y^*$  for anti- $k_T$  jets with  $R = 0.4$ . It is compared to NLO pQCD predictions. [37]

Figure 5.5 shows a grand comparison of the total cross-sections of all the SM processes that have been measured by the ATLAS detector. At  $\sqrt{s} = 13$  TeV (as shown by the pink square in the second bin of the figure), the dijet production cross-section is  $\sim 30 \mu\text{b}$  and is the largest of all the SM processes. This results in the large production of dijet events, increasing the chances of observing new phenomena.



## 5.2 Search for New Physics in the Dijet Mass Distribution

The invariant mass of a dijet event is given by Equation 5.9 and 5.10. Its distribution (i.e. number of dijet events as a function of  $m_{jj}$ ) is smooth and monotonically decreasing. It is dominated by dijet events produced via t-channel scattering where the jets are produced with high rapidities, i.e. more along the beam pipe. Its monotonically decreasing shape can be inferred from the behavior of the PDFs. Due to the steeply-falling shape of the PDFs (as a function of parton momentum fraction), it is more probable to see a large number events with low  $m_{jj}$  and fewer events at higher  $m_{jj}$ .

Many new physics theories propose new particles of definite mass that present themselves as localized excesses - i.e. resonances - above the smooth QCD dijet background. Such particles would be produced by the annihilation of partons from the colliding protons via s-channel diagrams and would decay to two jets with invariant mass equal to the mass of the particle. This would result in an excess of events over the smooth background located at the mass of the new particle. Due to the non-perfect detector resolution and the finite width <sup>1</sup> of the particle, the excess would be spread around its true mass with a width  $\sigma$ . As these resonances are produced via annihilation, they tend to decay isotropically and thus be central, i.e. the two decay jets are produced with low rapidities. This angular characteristic can be used to separate the resonances from the QCD background.

An example invariant mass distribution is shown in Figure 5.6. A narrow excess with width  $\sigma$  can be seen at mass  $M_X$  over the smooth QCD dijet distribution, which represents the background. The blue curve shows a parameterization of the background.

---

<sup>1</sup>The particle's width  $\Gamma$  is related to its lifetime  $\tau$  by,  $\Gamma = \hbar/\tau$ , where  $\hbar$  is the reduced Planck constant with value  $6.58 \times 10^{-22}$ MeVs.

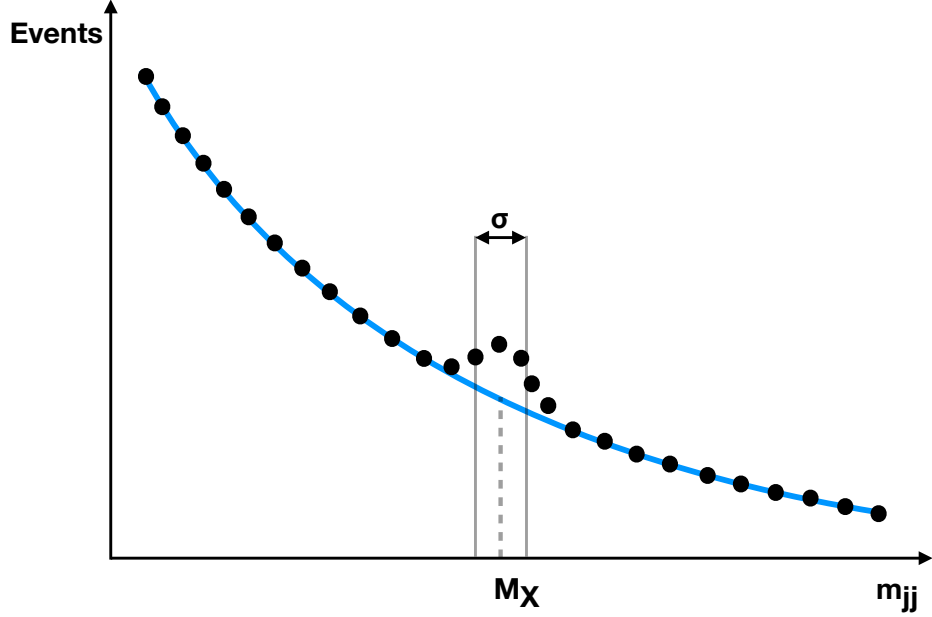


Figure 5.6: An example resonance with mass  $M_X$  and width  $\sigma$  over the smooth dijet invariant mass background distribution predicted by QCD.

Thus, the dijet analysis amounts to searching for a narrow resonance shape over a smooth background. The specific new physics signals that are the focus of this thesis are the excited quarks  $q^*$  and heavy gauge bosons  $W'$ . Each one of these models is associated to a specific signal shape that changes as a function of signal mass. The theoretical details for these new physics models will be discussed next. This thesis also presents general searches for Gaussian shapes, which are a good approximation to many new physics signals. This is useful because the Gaussian distribution is the lowest-order approximation for resonance signals.

### 5.2.1 Excited Quarks

As per our current understanding, quarks are fundamental particles. However, if this were not true - if quarks had substructure - it would be possible to observe heavy excited quark states,  $q^*$ .

Excited quarks have been thoroughly searched for in dijet searches since their

proposal in the 1980s [39] [75]. The model predicts the existence of excited quark states that couple to the vector gauge bosons with SM-like couplings. They can be produced at the LHC if the  $q^*$  compositeness scale (the characteristic energy scale),  $\Lambda$ , is less than the LHC center-of-mass energy. Requiring weak isospin gauge symmetry (analogous to the SM quarks), the effective Lagrangian for spin 1/2 excited quarks is given by

$$\mathcal{L}_{eff} = \frac{1}{2M^*} \bar{q}^* \sigma^{\mu\nu} [g_s f_s \frac{\lambda^2}{2} F_{\mu\nu}^a + g f \frac{\vec{\tau}}{2} \vec{W}_{\mu\nu} + g' f' \frac{Y}{2} B_{\mu\nu}] q_L + h.c. , \quad (5.16)$$

where  $h.c.$  stands for Hermitian conjugate. Here  $\bar{q}^*$  and  $q_L$  represent the weak isospin doublets of the excited and the SM left-handed quarks. The mass of the excited quark state is denoted by  $M^*$ . Here, the compositeness scale  $\Lambda$  is set equal to  $M^*$ . Each term of the Lagrangian shows the coupling of  $q^*$  and  $q_L$  with the vector gauge bosons: gluons  $F^a$ , SU(2) bosons  $W$  and the U(1) boson  $B$ .  $g_s$ ,  $g$  and  $g'$  are the gauge coupling constants and  $f_s$ ,  $f$  and  $f'$  are free parameters determined by the composite dynamics.

At the LHC,  $q^*$  states would be predominantly produced from quark and gluon interactions via the s-channel diagram. This can be seen in Figure 5.7 where the  $q^*$  production cross-section from the various channels is shown as a function of the  $q^*$  mass. The solid lines, dashed lines and dotted lines represent the  $qg$ ,  $qZ$  and  $q\gamma$  production modes. Curves for three collider center of mass energies (1.8 TeV, 17 TeV and 40 TeV) are shown.

Excited quarks can decay to the following states:  $qg$ ,  $qW$ ,  $qZ$  and  $q\gamma$ . Assuming that  $M^*$  is heavier than the mass of the  $W$  and  $Z$  gauge bosons and ignoring the SM

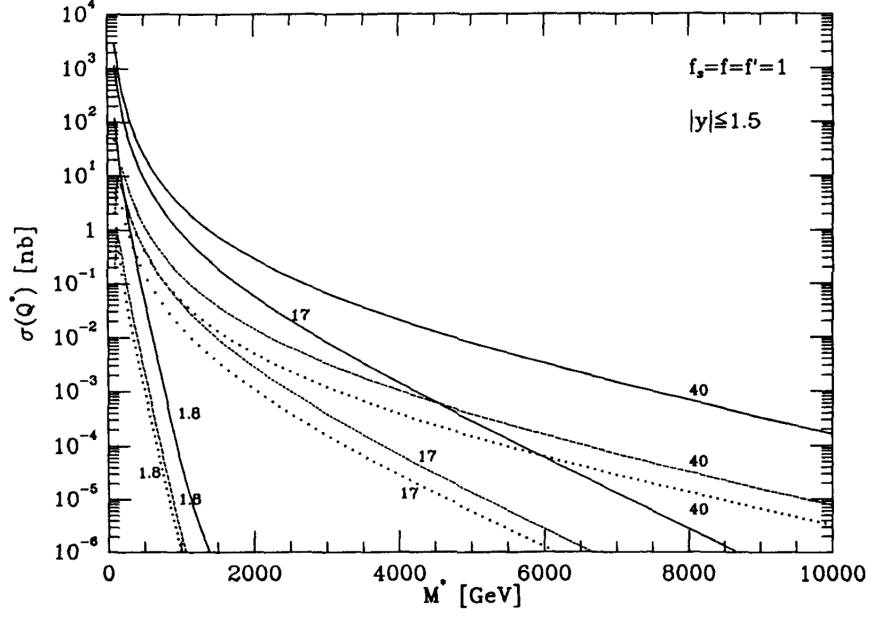


Figure 5.7:  $q^*$  production cross-section for various channels: solid lines  $qg$ , dashed lines  $qZ$  and dotted lines  $q\gamma$  and various center-of-mass energies: 1.8 TeV, 17 TeV and 40 TeV [39].

quark masses, the decay rates of  $q^*$  can be calculated from Equation 5.16:

$$\Gamma(q^* \rightarrow qg) = \frac{1}{3} \alpha_s f_s^2 M^* \quad (5.17)$$

$$\Gamma(q^* \rightarrow qW) = \frac{1}{8} \frac{g_W^2}{4\pi} f_W^2 M^* \left(1 - \frac{m_W^2}{M^{*2}}\right)^2 \left(2 + \frac{m_W^2}{M^{*2}}\right)^2 \quad (5.18)$$

$$\Gamma(q^* \rightarrow qZ) = \frac{1}{8} \frac{g_Z^2}{4\pi} f_Z^2 M^* \left(1 - \frac{m_Z^2}{M^{*2}}\right)^2 \left(2 + \frac{m_Z^2}{M^{*2}}\right)^2 \quad (5.19)$$

$$\Gamma(q^* \rightarrow q\gamma) = \frac{1}{4} \alpha f_\gamma^2 M^* , \quad (5.20)$$

where

$$f_\gamma = fT_3 + f'\frac{Y}{2} \quad (5.21)$$

$$f_W = \frac{f}{\sqrt{2}} \quad (5.22)$$

$$f_Z = fT_3 \cos^2 \theta_W - f'\frac{Y}{2} \sin^2 \theta_W \quad (5.23)$$

$$g_W = \frac{\sqrt{4\pi\alpha}}{\sin \theta_W} \quad (5.24)$$

$$g_Z = \frac{g_W}{\cos \theta_W} . \quad (5.25)$$

Here,  $\alpha_s$ ,  $\alpha$ ,  $g_W$  and  $g_Z$  are the strong, electromagnetic, and weak (W and Z boson) coupling strengths.  $T_3$  is the third component of the weak isospin,  $Y$  is the hypercharge and  $\theta_W$  is the weak mixing angle. Setting  $f_s = f = f'$ , the total  $q^*$  width is approximately

$$\Gamma(q^*) \approx 0.04f^2M^* . \quad (5.26)$$

If  $f$  is of order one, then the width of the  $q^*$  signal shape is narrow- 4% of its mass.

The dominant  $q^*$  decay state is  $qg$ . Experimentally, these would appear as two jets whose invariant mass would be equal to the mass of the excited quark. Table 5.2 shows the final state decay probabilities for a  $q^*$  of mass 1 TeV assuming exact SM couplings. These probabilities are known as *branching ratios*.

To search for  $q^*$  signals in the dijet invariant mass distribution, their signal shapes are required. These are obtained from MC simulations. Before showing the search results, Chapter 8 discusses the simulation and the experimental signature of  $q^*$  signals.



Table 5.2: Branching ratios for excited quarks of mass 1 TeV ( $u^*$  and  $d^*$ ) for  $f_s = f = f'$  and  $\alpha_s = 0.1$ .

Decay Mode	Branching Ratio (%)
$u^* \rightarrow ug$	83.4
$u^* \rightarrow dW$	10.9
$u^* \rightarrow uZ$	3.5
$u^* \rightarrow u\gamma$	2.2
$d^* \rightarrow dg$	83.4
$d^* \rightarrow uW$	10.9
$d^* \rightarrow dZ$	5.1
$d^* \rightarrow d\gamma$	0.5

## 5.2.2 Heavy Gauge Bosons

Heavier versions of the vector gauge bosons, known as  $W'$  and  $Z'$ , are hypothesized to exist in multiple theories that attempt to extend the electroweak sector of the SM [76–79]. In this thesis, a search for the heavy gauge boson  $W'$  is conducted by using a simplified model described in [80]. The model assumes that the heavy gauge bosons have the same coupling to fermions and bosons as the SM gauge bosons  $W$  and  $Z$ . For the  $W'$  these include:  $W'q\bar{q}$ ,  $W'l\bar{l}$  and  $W'^{\pm}W^{\pm}Z$ . This assumption leads to a large production cross-section from fermions (i.e. high production rate at hadrons colliders) and a decay to the SM particles.

The  $W'$  decay width to gauge bosons  $W^{\pm}Z$  and fermions  $f\bar{f}'$  ( $f, f' =$  leptons or quarks) is given by

$$\Gamma(W'^{\pm} \rightarrow ZW^{\pm}) = \frac{\alpha}{48} \cot^2 \theta_W M_{W'^{\pm}} \frac{M_{W'^{\pm}}^4}{M_Z^2 M_W^2} \quad (5.27)$$

$$\begin{aligned} & \times \left[ \left( 1 - \frac{M_Z^2 - M_W^2}{M_{W'^{\pm}}^2} \right) - 4 \frac{M_W^2}{M_{W'^{\pm}}^2} \right]^{3/2} \\ & \times \left[ 1 + 10 \left( \frac{M_W^2 + M_Z^2}{M_{W'^{\pm}}^2} \right) + \frac{M_W^4 + M_Z^4 + 10M_W^2 M_Z^2}{M_{W'^{\pm}}^4} \right] \\ \Gamma(W'^{\pm} \rightarrow f\bar{f}') &= \frac{\alpha}{12} N_c \frac{M_{W'^{\pm}}}{\sin^2 \theta_W}, \quad (5.28) \end{aligned}$$

where  $M_{W'\pm}$  is the mass of the  $W'$  and  $N_c$  is equal to 3 for quarks and 1 for leptons.

The  $W'$  states are created from  $q\bar{q}'$  annihilations via the s-channel diagram. Even though this particular model predominantly decays to  $WZ$ , its shape is a useful proxy for the more general family of  $W'$  models. The  $W'$  signal shapes used in this thesis are shown in Chapter 8.

### 5.2.3 General New Physics Signal Shapes

For a narrow resonance of any kind, the signal will be well approximated by a Gaussian shape with width given by the experimental resolution. More generally, to a first approximation, any new particle can be characterized by a mass and a width. Hence, generic Gaussian shapes are useful to quantify excesses in a model-independent way. Due to their simplicity, they provide convenient and easy-to-produce shapes for conducting resonance searches. Furthermore, their width can be readily adjusted, hence they can be used to model both narrow and wide signals (here, narrow signals mean those with width smaller than the dijet mass resolution). Narrow signals are modeled using Gaussian shapes whose width is consistent with the mass resolution. For wide signals, Gaussian shapes with varying widths are used.

The model-independent 95% confidence level upper limits provided by the Gaussian shapes can be used to infer approximate limits for any new physics model.

## 5.3 Previous Searches for $q^*$ and $W'$

The dijet analysis is a flagship analysis for hadron colliders. Due to the wealth of data and the great potential for discovering new phenomena, the analysis has been conducted ever since the invention of hadron colliders. Table 5.3 summarizes the dijet analyses conducted by different experiments colliding hadrons at different center-of-mass energies  $\sqrt{s}$ . The total amount of data analyzed, the dijet mass  $m_{jj}$  range, and

the excluded mass intervals for  $q^*$  and  $W'$  models are shown. UA1 (Underground Area 1) and UA2 (Underground Area 2) were detectors that operated on CERN's Super Proton-Antiproton collider (Sp $\bar{p}$ S) that collected data from 1981 to 1990. The Sp $\bar{p}$ S was modified to the present SPS that feeds protons to the LHC. CDF (Collider Detector at Fermilab) and D0 were experiments that analyzed hadron collisions from the Tevatron, the world's former highest energy particle accelerator at Fermilab in Illinois, USA. The Tevatron collected data from 1984 to 2011.

Table 5.3: Dijet resonance searches from past experiments. The name of the experiment, the year of the analysis publication, the center-of-mass energy, the amount of data analyzed and the dijet mass range covered are shown for each experiment. Also shown are the excluded mass intervals for  $q^*$  and  $W'$  models.

Experiment	Year	$\sqrt{s}$ ( TeV)	$\int \mathcal{L}dt$ ( pb $^{-1}$ )	$m_{jj}$ ( TeV)	$q^*$ ( TeV)	$W'$ ( TeV)	Reference
UA1	1986	0.63	0.26	0.07 – 0.3	–	–	[81]
UA1	1988	0.63	0.49	0.11 – 0.3	–	–	[82]
CDF	1990	1.8	0.026	0.06 – 0.5	–	–	[83]
UA2	1991	0.63	4.7	0.05 – 0.3	–	0.10 – 0.16	[84]
CDF	1993	1.8	4.2	0.14 – 1.0	–	–	[85]
UA2	1993	0.63	11	0.05 – 0.3	0.14 – 0.29	0.13 – 0.26	[86]
CDF	1995	1.8	19	0.15 – 0.9	0.20 – 0.56	–	[87]
CDF	1997	1.8	106	0.18 – 1.0	0.20 – 0.52	0.30 – 0.42	[88]
”	”	”	”	”	0.58 – 0.76	”	”
D0	2004	1.8	109	0.18 – 1.2	0.20 – 0.78	0.30 – 0.80	[89]
CDF	2009	1.96	1130	0.18 – 1.3	0.26 – 0.87	0.28 – 0.84	[90]
ATLAS	2010	7	0.32	0.20 – 1.7	0.30 – 1.26	–	[91]
CMS	2010	7	2.9	0.22 – 2.1	0.50 – 1.58	–	[92]
ATLAS	2011	7	36	0.50 – 2.8	0.60 – 2.15	–	[93]
CMS	2011	7	1000	0.84 – 3.7	1.00 – 2.49	1.00 – 1.51	[94]
ATLAS	2011	7	1000	0.72 – 4.1	0.80 – 2.99	–	[95]
ATLAS	2015	8	2030	0.25 – 4.5	0.80 – 4.06	0.80 – 2.45	[96]
CMS	2015	8	1970	0.89 – 5.2	1.20 – 3.50	1.20 – 1.90	[97]
ATLAS	2016	13	3600	1.10 – 7.1	2.00 – 5.20	1.50 – 2.60	[98]
CMS	2016	13	2400	1.20 – 6.3	1.50 – 5.00	1.50 – 2.60	[99]
CMS	2017	13	12900	0.45 – 2.0	0.60 – 5.40	0.60 – 2.70	[100]
”	”	”	”	1.06 – 8.0	”	”	”
ATLAS	2017	13	37000	1.10 – 8.2	2.00 – 6.00	1.50 – 3.60	[50]
CMS	2017	13	36000	0.49 – 2.0	0.60 – 6.00	0.60 – 3.30	[101]
”	”	”	”	1.25 – 8.0	”	”	”

These analyses have remained conceptually similar. The QCD background was modeled using either MC simulations (by UA1 and CDF before 1995) or fit functions (starting with UA2 in 1990, continued by CDF in 1995 and used until the present by ATLAS and CMS). The new physics resonances were modeled using a simple lineshape (before 1993) - Breit-Wigner functions convoluted with Gaussian signals - or by using shapes from MC simulations (after 1995).

The family of so-called ‘dijet functions’ has been particularly successful in parameterizing the QCD background in past analyses [90, 91, 93, 94, 96, 100]. These are defined as

$$f(z) = p_1(1 - z)^{p_2} z^{p_3 + p_4 \log z + p_5 (\log z)^2}, \quad (5.29)$$

where  $z = m_{jj}/\sqrt{s}$  and  $p_i$  are the parameters. These functions are physically motivated: the  $(1 - z)^{p_2}$  term is related to the leading-order QCD matrix element and the  $z^p$  term follows the form of the steeply-falling PDFs as a function of momentum. Depending on the number of parameters used, the functions are called the 3 parameter ( $p_4 = p_5 = 0$ ), the 4 parameter ( $p_5 = 0$ ), and the 5 parameter dijet function. Higher-order functions (with more  $\log z$  terms) can also be made.

Traditionally (starting from 2010), the search for dijet resonances by the ATLAS collaboration has been conducted by performing a model-independent search using the BUMP HUNTER algorithm [102]. A background model is produced by parameterizing the binned dijet data mass distribution using one of the forms of the dijet function (Equation 5.29). BUMP HUNTER is then used to identify the region (in terms of a group of adjacent bins) in the data that is the most discrepant with respect to the background model. If the significance of the excess is large, then the search results in the observation of an “interesting” excess. However, if no excess is found, then 95% CL limits are calculated for specific theory models and general Gaussian signals using

a Bayesian statistical method. These are used to rule out the theory models below the calculated 95% upper limit. More details on the BUMP HUNTER search method will be discussed later in Chapter 8.

## 5.4 Challenges in the Dijet Search

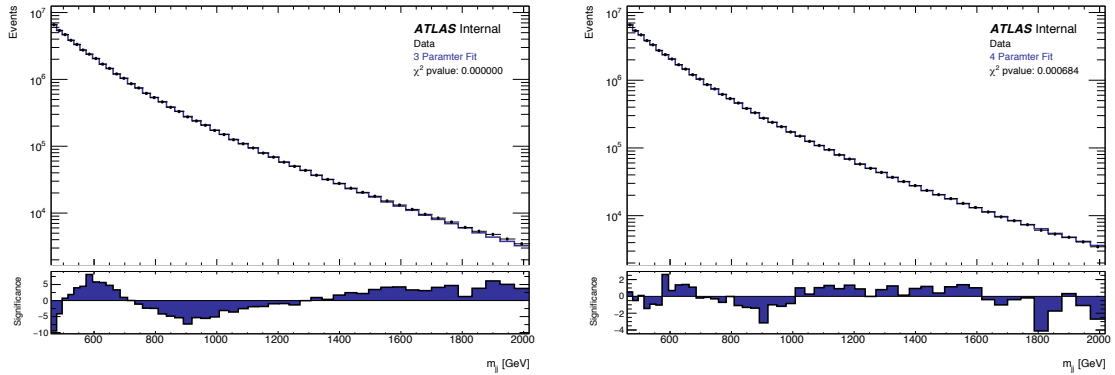
As described in the previous section, resonance searches in the dijet channel at ATLAS are conducted by looking for a localized excess above a smooth background. The smooth background is obtained by fitting the entire dijet mass distribution with ad-hoc functions, such as the dijet functions. The problem with this approach is that these functions do not necessarily reflect the true underlying mass distribution. They have been successfully used until now due to the relatively smaller datasets and by increasing the dijet mass distribution's starting point. With increasing data, however, their approximate nature becomes apparent and obtaining a background model using fits becomes increasingly challenging, especially when the data can span more than 6 orders of magnitude!

This challenge is clearly illustrated in Figure 5.8 where the low-mass dijet data distribution [40] is fitted using three dijet functions with different numbers of parameters. The distribution is obtained from  $3.4 \text{ fb}^{-1}$  of data collected in 2015 and contains approximately 50 millions events between 450 - 2000 GeV.

The 3, 4 and 5-parameter fits in this range are shown in Figure 5.8 (a), (b) and (c) respectively. The second panel of each plot shows the significance, defined as the difference between the data and the fit divided by the square root of the data. The difference is quantified using the  $\chi^2$  p-value as shown on the plots <sup>2</sup>. These values are unacceptably small indicating that the data is inconsistent with these fits. The swings in the significance, particularly with the 3-parameter function, also demonstrates the

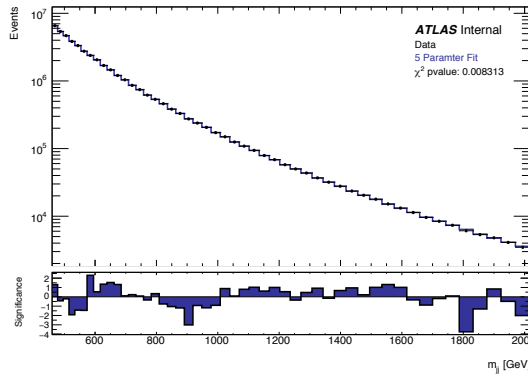
---

<sup>2</sup>As a point of comparison, p-values of 0.01, 0.001, 0.0001 and 0.00001 correspond to a  $2.3\sigma$ ,  $3\sigma$ ,  $3.7\sigma$  and  $4.2\sigma$  disagreement.



(a) 3-parameter fit

(b) 4-parameter fit



(c) 5-parameter fit

Figure 5.8: Fits to the low-mass dijet invariant mass distribution obtained from  $3.4 \text{ fb}^{-1}$  data collected in 2015 [40]. The functions used are (a) the 3-parameter, (b) the 4-parameter and (c) the 5-parameter dijet functions. The significant swings seen in second panel of (a) shows the inability of the 3-parameter function to model the data. The higher-order functions ((b) and (c)) perform better, however the region between 1 - 1.6 TeV is poorly modeled.

inability of the functions to model the data well.

One way to cope with such large statistics is to keep adding parameters until a good fit to the data is obtained. Alternatively, one might test/invent new functions. A third way to solve this problem is to reduce the fit range and consequentially reduce the pressure on the fit functions, This would allow one to perform a localized resonance search without fitting the entire data distribution. The method based around this idea, i.e. the use of smaller window sizes, came to be know as SWIFT and the next chapter is dedicated to describing it.

## CHAPTER 6

# Sliding Window Fits

This chapter will present a general-purpose statistical tool for conducting resonance searches: Sliding Window Fits (SWiFT). It was designed to address the difficulties faced by the traditional resonance search method in the face of increasing data statistics.

SWiFT solves the problem in two ways. It provides a method for conducting model-dependent resonance searches by sliding over the data distribution in small, overlapping, auto-sized windows. In each window, it checks for the presence of a new particle by performing a series of fits. After a full slide, it provides,

- a likelihood-ratio-based local p-value scan for a given signal shape,
- 95% confidence level upper limits on the extracted signal using the profiled likelihood method,
- the SWiFT background - a global background estimation created using a novel technique.

The SWiFT background can also be used to conduct a model-independent search using the BUMPHUNTER algorithm.



## 6.1 Statistical Concepts

Before describing SWIFT, this section will summarize several statistical concepts that will be utilized later.

### 6.1.1 Likelihood Fits

SWIFT performs its fits by minimizing the negative log likelihood (LLH). The likelihood (LH) function quantifies the probability of the model (specified by its parameter values), given specific data. When the data is represented by a binned histogram and the model is described in terms of parameters  $\vec{p}$ , the LH can be described using Poisson statistics:

$$\text{LH}(\vec{p} | x) = \prod_{i=1}^N e^{-\lambda_i(\vec{p})} \frac{(\lambda_i(\vec{p}))^{x_i}}{x_i!}, \quad (6.1)$$

where  $N$  is the total number of bins,  $x_i$  and  $\lambda_i$  are the content of the data histogram and the model in the  $i$ 'th bin, respectively.

As the LH consists of a product of very small numbers, working with it directly is a recipe for numerical disaster. Hence, instead of maximizing the LH, the negative LLH is minimized to avoid these issues. The negative logarithm is a strictly decreasing function of its argument, and so the negative log of a function reaches its minimum value at the same point as the function itself. The negative LLH is described by

$$-\text{LLH}(\vec{p} | x) = \sum_{i=1}^N [\lambda_i(\vec{p}) - x_i \ln(\lambda_i(\vec{p})) + \ln(x_i!)] . \quad (6.2)$$

Systematic uncertainties that alter the shape of the model are accounted for by incorporating them into likelihood. Each uncertainty is associating to a nuisance parameter (NP) that directly affects the model. For example, NPs associated to the JES uncertainties change the shape of the signal model and the NP associated to the

luminosity changes the relationship between the yield and cross-section. In general, there is prior knowledge of the acceptable values of the NPs. This is incorporated by adding a Gaussian penalty term for each NP to the likelihood function:

$$-\text{LLH}(\vec{\theta} | x) = \sum_{i=1}^N [\lambda_i(\vec{p}) - x_i \ln(\lambda_i(\vec{p})) + \ln(x_i!)] + \sum_j \frac{(\text{NP}_j)^2}{2}, \quad (6.3)$$

where  $j$  is the number of NPs and  $\vec{\theta}$  is the function parameters  $\vec{p}$  together with all the NP. The penalty terms disfavor drastic changes to the NPs. Note that the NPs are scaled such that the variance of each is equal to one.

The minimizer then minimizes this penalized LLH and determines the best values for the  $\vec{\theta}$ . The minimization is conducted by a numerical minimizer that adjusts the model's parameters until it finds the combination that has the smallest negative LLH value. This is the form of the model that best represents the data.

The minimizer used to perform the fits is MINUIT [103]. MINUIT is a numerical minimization package written specifically for high-energy physics applications in C++<sup>1</sup>. It contains implementations of several different minimization algorithms. SWIFT uses the SIMPLEX and MIGRAD algorithms. SIMPLEX uses the Nelder-Mead method [104] to find an approximate fit from which the MIGRAD minimization is initialized. MIGRAD uses a variable-metric minimization method [105]. The combination of the two minimization methods provides robust fitting, even in the cases where the initial conditions are far away from the minimum.

### 6.1.2 Types of Fits

SWIFT performs two kinds of fits: background-only, and signal+background. The comparison of these two fits allows one to quantify the significance of an excess, as will be described later.

---

<sup>1</sup>MINUIT was originally written in FORTRAN in the 1970s but was later ported to C++.

The background-only fits provide a model for the smooth dijet background under the assumption that there is no signal present in the data. The functions used are the 3- and 4-parameter dijet functions (Equation 5.29).

The signal+background fits are performed under the assumption that there might be signal present in the data. The model is a sum of a signal component and a background component. The signal component could be any of the shapes of interest, e.g. the Gaussian or excited quark ( $q^*$ ) signal shape, and the background component is the 3- or 4-parameter dijet function. Note that the background-only function is a special case of the signal+background function (when the signal component is fixed to zero).

### 6.1.3 $\chi^2$ p-value

The  $\chi^2$  p-value provides a goodness-of-fit measure by comparing the data to a fit. It is based on a quantity known as the *chi-squared*, which, given a data histogram with  $N$  bins, can be defined as

$$\chi^2 = \sum_{i=1}^N \frac{(x_i - \lambda_i)^2}{\sigma_i}. \quad (6.4)$$

Here,  $x_i$  and  $\lambda_i$  are the content of the data histogram and the fit in the  $i$ th bin, respectively, and  $\sigma_i$  is the variance of  $\lambda_i$ . If in each bin, the data has statistically small differences with respect to the fit, then each term in the  $\chi^2$  equation would be of order one and the total  $\chi^2$  would be around  $N$ . However, if the data is very different as compared to the prediction, then the  $\chi^2$  value can become much larger than  $N$ .

To convert the  $\chi^2$  value to a p-value (a probability), the probability distribution

of the  $\chi^2$  is used. For  $\nu$  degrees of freedom, the  $\chi^2$  distribution is defined as

$$f(\chi^2) = \frac{1}{2^{\nu/2}\Gamma(\nu/2)} e^{-\chi^2/2} (\chi^2)^{(\nu/2)-1}, \quad (6.5)$$

where  $\Gamma$  is the gamma function. Figure 6.1 shows  $\chi^2$  distributions for three values of  $\nu$ .

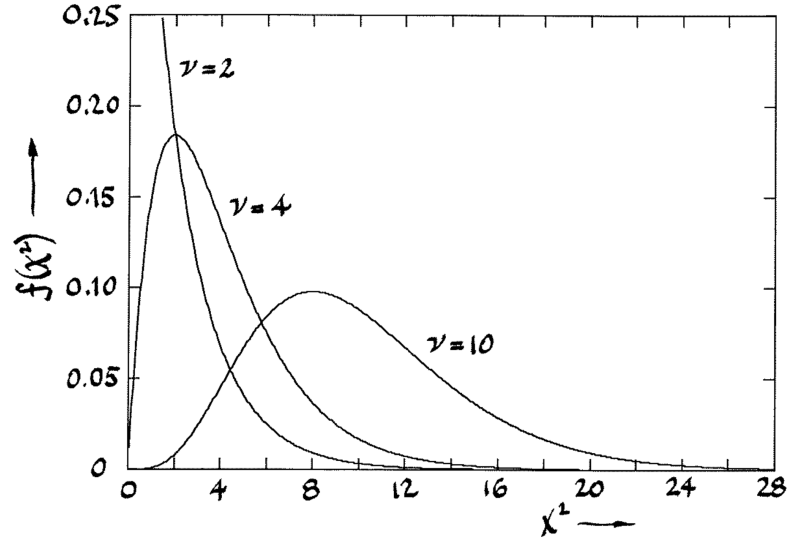


Figure 6.1: The  $\chi^2$  probability distributions for  $\nu = 2, 4$  and  $10$ . Here  $\nu$  is the number of degrees of freedom. [41]

For a data histogram (with  $N$  bins) that is fit with a function with  $P$  parameters, the number of degrees of freedom is  $\nu = N - P$ . Thus, knowing  $\nu$  and the  $\chi^2$  of the data with respect to the fit (from Equation 6.4), the  $\chi^2$  p-value can be calculated as

$$\chi^2 \text{ p-value} = \int_{\chi^2}^{\infty} f(\chi^2) d\chi^2. \quad (6.6)$$

If the experiment could be repeated a large number of times and the data from each experiment fit to the same function, the p-value would give the probability of obtaining a  $\chi^2$  greater than or equal to what was observed in the actual data. A  $\chi^2$  p-value of 1 would mean that all the repeated experiments would have a  $\chi^2$  greater than what was seen in the data. A  $\chi^2$  p-value of 0.05 would mean that only 5% of

the repeated experiments would have a  $\chi^2$  greater than the data. Thus, a  $\chi^2$  p-value of order 1 represents a good fit to the data. The smaller the p-value, the worse the fit.

#### 6.1.4 The Log Likelihood Ratio and The Local P-value

The log likelihood ratio (LLHR) is obtained by taking the log of ratio of the likelihoods of two functions. Using the signal+background and background-only functions, it can be defined as,

$$\text{LLHR} = \ln \frac{\text{LH}(\text{signal+background})}{\text{LH}(\text{background-only})}. \quad (6.7)$$

The LLHR provides a powerful and robust measure of how much better the signal+background fit models the data than the background-only fit. In the presence of a signal, the likelihood of the signal+background fit will be substantially better than that of the background-only fit, resulting in a large LLHR value. If there is no excess, then both functions will perform similarly, and the LLHR value would be small.

Wilks' theorem [106], which is applicable to the present application, can be used to convert the LLHR to a p-value. It states that, for a pair of nested functions, in the limit of large statistics, two times the negative LLHR will be chi-square distributed with degrees of freedom ( $\nu$ ) equal to the difference in dimensions of the functions:

$$-2 \times \text{LLHR} = \chi_\nu^2. \quad (6.8)$$

Here  $\nu$  is equal to one as the signal+background function has one extra free parameter - the signal normalization.

The p-value derived from the LLHR is known as a *local p-value*. Assume that the background-only hypothesis is true, but an excess at a specific point  $M$  is observed with a LLHR p-value  $P_M$ . If the experiment were to be repeated multiple times,  $P_M$

gives the probability of seeing a LLHR (at point  $M$ ) greater than or equal to what was actually observed. This quantifies the odds of observing a given excess by chance alone.

### 6.1.5 The Global P-value

The local p-value quantifies the odds of observing an excess by chance alone *at a specific point*. However, one typically tests many points and in principle an excess (due to a statistical fluctuation) could have been observed at any of them. This is known as the look-elsewhere effect [107], and a p-value that accounts for it is known as a *global p-value*.

The global p-value is calculated from *pseudo-experiments (PE)*. PEs are created from a binned distribution that is presumed to provide a good model for the binned data. This could be a MC model, a single parametric fit to the data, the SWIFT background model, etc.

A PE is created by randomly varying the bin contents of the model using Poisson statistics. The global p-value is obtained by repeating the full statistical analysis on each PE. It is calculated by counting the fraction of PEs that have a LLHR (at *any* point) equal to or greater than what was observed in the data:

$$\text{global p-value} = \frac{\# \text{ PEs with LLHR} > \text{LLR of data}}{\text{Total} \# \text{ PEs}}. \quad (6.9)$$

The global p-value is always larger (i.e. less significant) than the local p-value. It provides a more realistic estimation of the significance of an excess.

### 6.1.6 95% CL Limits

A 95% CL limit on a theory model corresponds to the largest amount of signal ( $N_{95}$ ) consistent with the data at the 5% level. A simple example that illustrates the concept

is the following. Supposing some signal shape, one extracts 15 signal events from a signal+background fit. The 95% CL limit is the number of signal events such that 15 is  $2\sigma$  down from  $N_{95}$ . Assuming Gaussian statistics, this would be 25 events, since  $25 - 2\sqrt{25} = 15$ . Here the  $2\sigma$  uncertainty on 25 events is  $2\sqrt{25} = 10$  events.

Rather than the number of events, limits are customarily expressed in terms of a cross-section  $\sigma_{95}$ . The 95% CL limit calculated from the data is known as the observed limit. On the other hand, the limit calculated from the background model (i.e. assuming zero signal events) is known as the expected limit. Typically, the expected limit is shown with its  $1\sigma$  and  $2\sigma$  uncertainties.

The 95% CL limits calculated by SWIFT use the profiled likelihood method (a frequentist approach). In this method, the NPs representing the uncertainties are accounted for by profiling, i.e. by fitting them away. The starting point for the limit-setting procedure is the best signal+background fit, the fit with signal normalization  $N_{\text{best}}$  and parameter values  $\vec{\theta}^2$  that minimize the negative LLH. The 95% CL limit  $N_{95}$  is defined as the the signal such that the LLH of  $N_{95}$  is worse than the best LLH by a specified value  $\Delta\text{LLH}$ :

$$\begin{aligned}
 -\text{LLH} \left( N_{95}, \vec{\theta} \mid x \right) &= -\text{LLH} \left( N_{\text{best}}, \vec{\theta} \mid x \right) + \Delta\text{LLH} & (6.10) \\
 \Delta\text{LLH} &= \frac{[\Phi^{-1}(0.95)]^2}{2},
 \end{aligned}$$

where  $\Phi^{-1}$  is the inverse of the cumulative distribution function (also known as the quantile function) of the normal distribution. For a probability  $c$ , it is defined in terms of the error function erf:

$$\Phi^{-1}(c) = \sqrt{2} \operatorname{erf}^{-1}(2c - 1) \quad (6.11)$$

For  $c = 0.95$ ,  $\Delta\text{LLH}$  is equal to a value of 1.92073. Hence, the 95% CL limit amounts

---

<sup>2</sup> $\vec{\theta}$  includes the background parameters  $\vec{p}$  and NPs for each uncertainty.

to determining  $N_{95}$  such that the yield extracted from the data is approximately  $2\sigma$  below  $N_{95}$ .

## 6.2 SWiFt in a Nutshell

SWiFT searches for localized excesses in data histograms by performing fits in many small and overlapping windows. The window sizes are automatically determined (as will be described later) around each bin of the histogram, called the window *center* from now on. After the size for each window is determined, SWiFT checks for the presence of an excess at the window center by comparing a signal+background and background-only fits as described above.

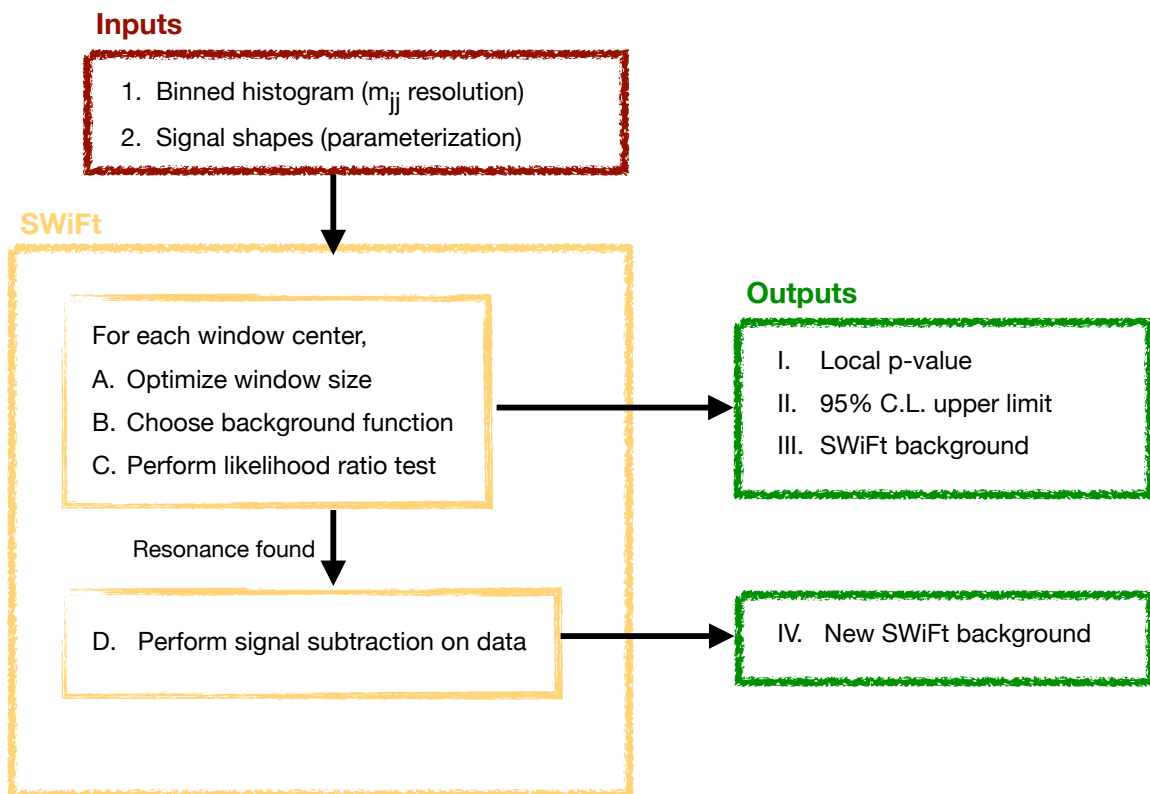


Figure 6.2: Flow chart for the SWiFT procedure.

The entire SWiFT procedure is summarized in Figure 6.2. SWiFT takes a data histogram and a set of signal shape parameterizations as inputs and performs its



slide. The data histogram is binned according to the  $m_{jj}$  resolution (see Figure 7.12). The signal parameterizations are obtained by interpolating the limited number of shapes obtained from MC simulations as described in Appendix B. During the slide, the data distribution is analyzed window-by-window for the presence of an excess. After the full slide, the LLHR based local p-values and 95% confidence limits as a function of the window center are calculated. The SWIFT background estimation for the full data distribution is also produced. If a “significant” excess is found, SWIFT recalculates the background estimation by removing the excess from the data. The next sections will describe the steps of the procedure in more detail.

### 6.2.1 The Slide and the Fits

The slide starts at the lower end of the data histogram. The first center is located several bins in to steer clear of edge-effects. SWIFT then picks a window size around the center and performs its fits within the window. After the fits finish, SWIFT slides the window center one bin to the right and re-optimizes the window size around the new center. The initial parameters of the fits in the new window are initialized from the fits in the previous window. Repeating this process, the window center slides across the histogram bin-by-bin.

In each window, the following two pairs of fits are performed (that differ only in the background function used):

- A **nominal** signal+background and a **nominal** background-only fit. These two fits are called nominal as they use the 3 parameter dijet function as the background component.
- An **alternate** signal+background and an **alternate** background-only fit. These fits are called alternate as they use the 4 parameter dijet function as the background component.

The first two windows of the slide on a hypothetical distribution are shown in Figure 6.3. The vertical green lines show the window centers and the shaded boxes show the window sizes. Bin edges around the red dots represent the 15 window centers that SWiFT will slide over and the black dots show the bins that are not used as window centers. The blue curves show the background-only fits in the windows.

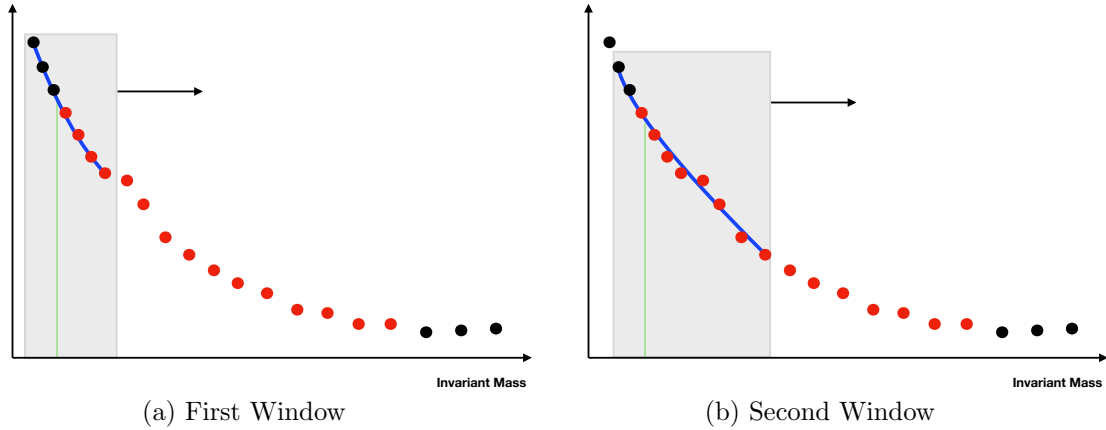


Figure 6.3: First two windows of the SWiFT slide over a hypothetical mass distribution. The vertical green lines show the window centers (which match the bin-edges) and the grey boxes represent the window size. Bin edges around the red dots show all the possible window centers and the blue curves show background-only fits.

## 6.2.2 Picking the Window Sizes

The window sizes are automatically selected around each window center. This is done by performing multiple nominal background-only fits with different window sizes. The size with the best  $\chi^2$  p-value is chosen. The  $\chi^2$  p-value is used to correctly account for the differences in the numbers of degrees of freedom (NDF) between different window sizes. The NDF is equal to the number of bins in the window minus the number of parameters of the function<sup>3</sup>. This procedure identifies a window size that ensures good fits without fitting away the signal. It also performs well in the presence of a signal. More details on this are provided later in this chapter.

<sup>3</sup>Without taking the NDF into account, the smallest window size would always be preferred.

A reasonable lower limit is set on the sizes tested to prevent SWiFT from picking very small windows. The lower limit is set to be at least three times larger than the width of the widest signal of interest. The selection procedure is designed to ensure a smooth evolution of the window sizes.

### 6.2.3 The Likelihood Ratio Scan

After the window sizes are fixed, the two pairs of the nominal and alternate signal+background and background-only fits are performed in each window. Figure 6.4 shows examples of these four fits for a window of a hypothetical data distribution. The nominal background-only fit (blue curve) and nominal signal+background fit (red curve) are shown in Figure 6.4 (a) and the alternate background-only fit (cyan curve) and alternate signal+background fit (orange curve) are displayed in Figure 6.4 (b).

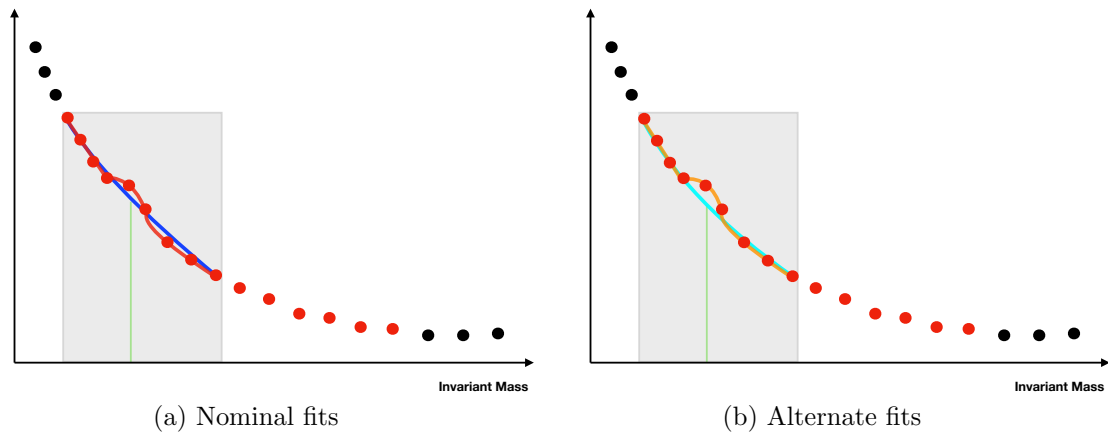


Figure 6.4: Two windows of the SWiFT slide over the mass distribution. The vertical green lines show the window centers (which match the bin-edges) and the grey boxes represent the window size. Bin edges around the red dots show all the possible window centers. The blue (nominal, e.g. 3-parameter) and cyan (alternate, e.g. 4-parameter) curves show background-only fits. The red (nominal, e.g. 3-parameter + signal) and orange (alternate, e.g. 4-parameter + signal) curves show the two signal+background fits.

At this stage, SWiFT chooses to keep either the set of nominal functions or the set of alternate ones. The choice is made based on the  $\chi^2$  p-value of the two sig-

nal+background fits (i.e. the red and orange curves from Figure 6.4 (a) and Figure 6.4 (b), respectively). Using the  $\chi^2$  p-value takes into account the number of degrees of freedom. This allows for a fair comparison between the two signal+background functions without always favoring the higher order one (hence preventing over-fitting).

After the choice between the nominal and alternate functions is made for a window, the LLHR is constructed by taking the log of the likelihood ratio of the chosen set of signal+background and background-only fits as shown in Equation 6.7. This is converted to a local p-value using Wilks' theorem (Equation 6.8).

At the end of the slide, SWIFT outputs a local p-value scan as a function of the window center. Windows with low p-values correspond to excesses with larger significances. SWIFT identifies the window with the lowest local p-value and calculates the corresponding global p-value.

### 6.2.4 The 95% Confidence Level Limits

After the local p-value calculation, SWIFT calculates the 95% CL limit on the signal extracted from the signal+background fit. It is calculated using a binary search algorithm which is sketched in Figure 6.5. In the figure, the likelihood is shown as a function of the number of signal events. The red dots represent the number of extracted signal events from the signal+background fit and the likelihood that corresponds to this number of signal events is called the minimum likelihood.

For positive signal (Figure 6.5 (a)), the green dot represents the 95% CL limit on the extracted signal. The purpose of the binary search is to start from the extracted number of events (the red dot) and determine out the 95% CL limit (the green dot). In each step of the search, the binary search increases/decreases the number of signal events until it converges on the 95% CL limit. The steps are shown by the grey dots and arrows in the figure.

For negative signals, the search for the 95% CL limit is performed by scanning

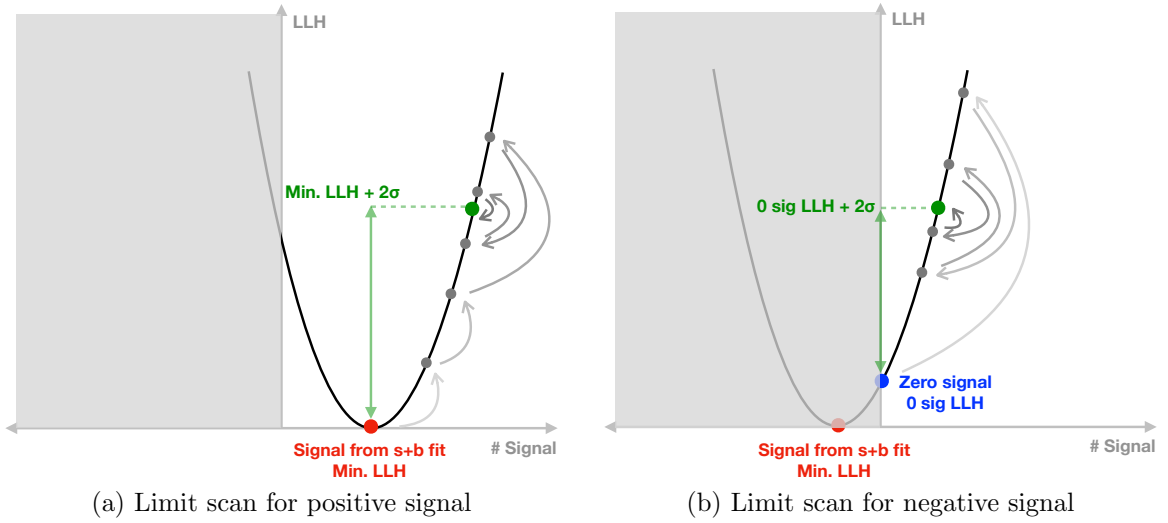


Figure 6.5: 95% C.L. limit calculation procedure for (a) positive extracted signal and (b) negative extracted signal.

above the background-only fit (i.e. zero extracted signal events). This is demonstrated in Figure 6.5 (b) where the blue dot represents zero signal events and the green dot shows the target likelihood, worse by  $2\sigma$  w.r.t. the zero signal likelihood.

During each step of the search, all parameters except for the signal normalization are free and are allowed to float to their best values. This is known as profiling and it accounts for the systematic uncertainties by fitting them away.

The expected 95% limit is calculated from the same pseudo-experiments used for the global p-value calculation. For each pseudo-experiment, a full SWiFT search is performed and 95% CL limits are calculated. The expected limit is then obtained by taking the median of all the limits from the pseudo-experiments. The  $1\sigma$  and  $2\sigma$  uncertainties on the expected limits are obtained by determining the range within which 68% and 95% pseudo-experiments lie, respectively.

## 6.2.5 Systematic Uncertainties

The following systematic uncertainties are profiled during the fitting procedure:

1. Background parameters: The uncertainties on the background parameters are taken into account by allowing them to float during all the fits.
2. Signal shape: The signal shape is parameterized as a function of three JES nuisance parameters. A gaussian penalty term for each is added to the likelihood as described above. These uncertainties alter the signal shape.
3. PDF and Scale: A 1% flat systematic is applied to account for the PDF and scale uncertainties. These uncertainties largely affect the normalization of the signal and are applied as flat multiplicative scale factors.
4. Luminosity: A flat 3.2% flat uncertainty is added for the luminosity uncertainty. It is also applied as a flat multiplicative scale factor.

The last two uncertainties (i.e. the flat ones) are added in quadrature and a combined nuisance parameter is used to represent them. The effects of the JES nuisance parameters on the signal shapes are obtained by varying the jet calibrations in accord with their  $\pm 1\sigma$  uncertainties. The varied shapes are fit to the same parameterization as the nominal shapes (using the signal morphing procedure detailed in Appendix B). The parameterizations at other values of the nuisance parameters are obtained by linearly interpolating the parameters of the JES-varied shapes.

The procedure also accounts for the systematic uncertainty associated to the choice of the function used to model the background. There are multiple ad-hoc functions that can be used to parameterize the background in each window. The uncertainty on the choice is taken into account by allowing the background function to swap between a nominal and an alternate function. In principle more functions could be added but there is little gain (i.e. little improvement in the background model) from doing so.

## 6.2.6 The SWiFt Background

SWiFt tests for the presence of new physics in each window by calculating local p-values using the signal+background and background-only fits. For bump hunting, there is no need for a single background estimation that spans the entire data distribution. However, it is useful to have one in order to compute the global p-values, the expected 95% CL limits, and to perform the model-independent search.

The SWiFt background is extracted from the data bin-by-bin as SWiFt slides over the data distribution. It is constructed as follows. In each window, (after the choice to keep the nominal set or alternate set of functions is made) the background-only fit is evaluated at the window center. This provides the SWiFt background estimation in only one bin, i.e. at the window center. As the window slides across the distribution bin-by-bin, the SWiFt background is constructed by stitching together the evaluations of each background-only fit at each window center. For the very first and last windows, in addition to evaluating the background-only fit at the window centers, bins that are below (for first window) and above (for last window) the window centers are evaluated. This gives the SWiFt background estimation for bins at the edges of the data distribution that are not window centers.

A few steps in this procedure can be seen in Figure 6.6 where the red dots represent the bins that are considered as window centers. The black dots are too close to the edges and are not considered. Figure 6.18 (a) and (d) show the extraction of the SWiFt background in the first and last window. Here, the background-only fits are evaluated at the window centers (shown by the vertical green lines) and the edge bins (black dots). Figure 6.18 (b) and (c) show two intermediate windows where the SWiFt background is obtained by evaluating the fits at the window centers only.

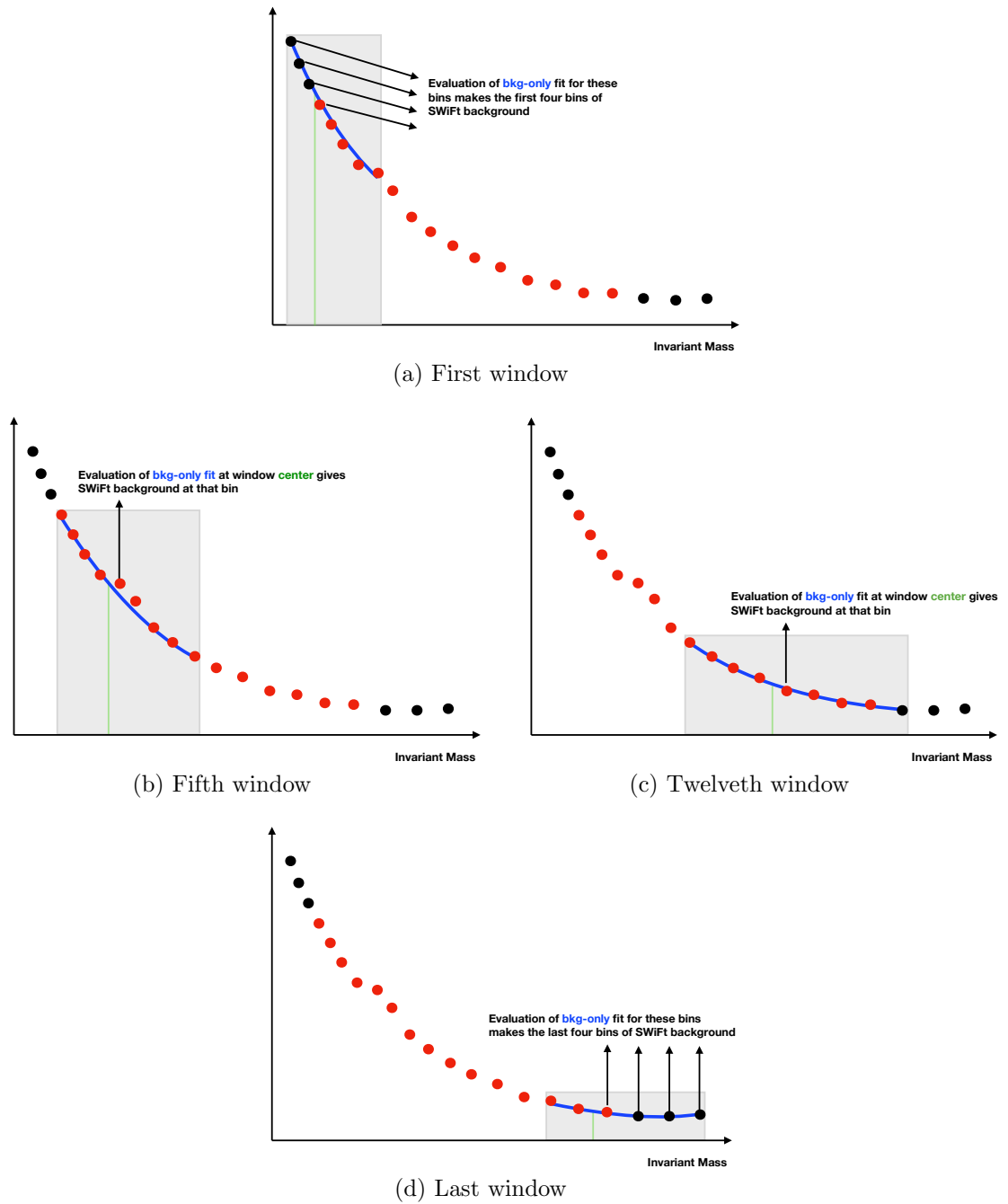


Figure 6.6: Bin-by-bin construction of the SWiFT background. The vertical green lines show the bin-edges that are window centers. The red dots show the data around the window centers and the black dots are the bins close to the edges. (a) & (d) First and last windows. The background-only fit (blue curve) is evaluated at the window center and the three edge bins. (b) & (c) Intermediate windows where the background-only fit is evaluated at the window centers only.



## 6.2.7 Steps Performed if a Signal is Detected

An excess is “interesting” if the window with the lowest p-value in the scan has a value less than 0.001<sup>4</sup>. If such an excess is found, a new SWiFT background is created after subtracting the signal (extracted from the window) from the data distribution. This removes the bias in the background produced due to the presence of the signal. The bias-free background can then be used to calculate the correct global p-value and expected limits.

An example of this is shown in Figure 6.7. The black dots show the local p-value calculated for each window and the red dot shows the window with the lowest p-value.

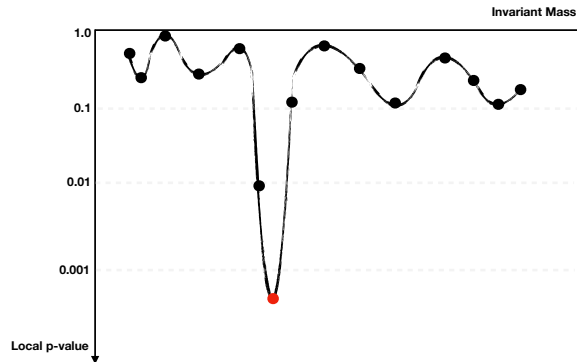


Figure 6.7: Example of local p-value scan produced at the end of the SWiFT slide. The red dot shows the window with the most significant excess. If the local p-value of the most significant excess is less than 0.001 (roughly  $3\sigma$ ), SWiFT’s signal subtraction stage is triggered and a new SWiFT background estimation is produced.

## 6.3 SWiFT Validation

In this section, the performance of the SWiFT method is quantified using a test distribution and the following are discussed:

1. concrete results from one pseudo-experiment drawn from the test distribution,

---

<sup>4</sup>This roughly corresponds to an excess with a local significance of  $3\sigma$ .

2. the performance of the window size selection procedure and the SWIFT background,
3. the spurious signal (i.e. the amount of signal extracted in the absence of a true signal),
4. linearity (i.e. linear trend between the number of injected and extracted signal events),
5. signal injection studies (i.e. performance of SWIFT in the presence of signal).

### 6.3.1 The Test Distribution

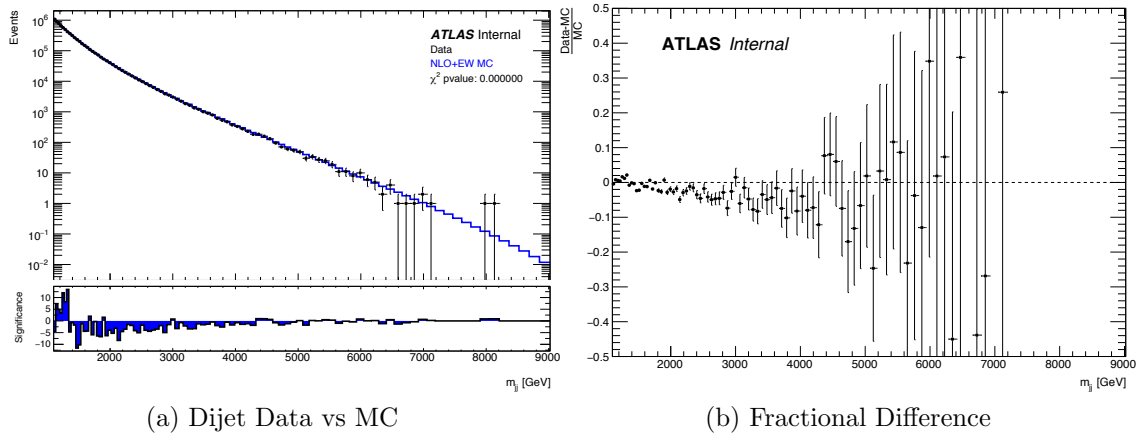


Figure 6.8: (a)  $37.0 \text{ fb}^{-1}$  dijet data compared to NLO+EW MC scaled to data. Bottom panel shows the significance, defined as the difference between the data and the MC divided by the square root of the data. (b) Fractional difference between data and MC dijet spectra.

To test the SWIFT procedure, it would be ideal to use the dijet mass spectrum from a MC simulation. Unfortunately this is not possible due to limited MC statistics. This can be seen in Figure 6.8, where the dijet mass spectrum from the Pythia MC simulation is compared to the data. The large spikes in the significance at low mass (lower panel of Figure 6.8 (a)) are due to limited MC statistics. Furthermore, the

fractional difference between the data and the MC, as shown in Figure 6.8 (b), shows an evident mis-modeling of the data.

Given these problems, the dijet MC simulation cannot be used as a test distribution directly. However, it can be smoothed with a global fit and that in turn can be used as the parent distribution for pseudo-experiments. Thus, to obtain test distributions, the MC is fitted with a 6-parameter dijet function (the red curve in Figure 6.9). In the rest of this section, this 6-parameter fit to the MC will be called the *smoothed MC*. Even though the shape of this fit differs from the data, it nonetheless provides a signal-free mass distribution for testing the SWIFT procedure.

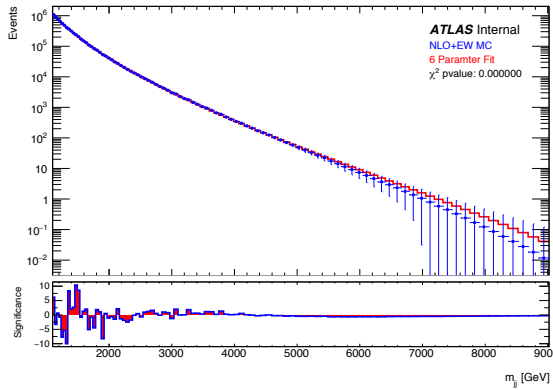


Figure 6.9: MC spectrum fit to 6-parameter dijet function. The bin errors of the MC are set to  $\sqrt{N_{MC}}$ . Pseudo-experiments drawn from the fit are used to perform SWIFT tests.

To characterize the procedure’s response to the presence of a signal, signals with different normalizations are added to the smoothed MC fit, and then pseudo-experiments are drawn from the fit + signal distribution.

For the results shown next, the dijet distributions start at 1100 GeV. SWIFT starts its slide from a window center of 1416 GeV and ends at 6407 GeV. The window selection procedure scans sizes from 30% to 100% of the window center. The nominal and alternate background functions are the 3- and 4-parameter dijet functions, respectively.

### 6.3.2 A Demonstration of SWiFt

In this section, results from one pseudo-experiment are shown to familiarize the reader with the SWiFt outputs. Results from a distribution with and without injected signal will be shown side-by-side. The no-signal-injected distribution, Figure 6.10 (a), is created by performing a pseudo-experiment with seed 106 (randomly picked) from the smoothed MC. To produce the signal-injected distribution, Figure 6.10 (b), a resolution-width Gaussian is injected into the smoothed MC at 4070 GeV with 250 events. The distribution is then varied according to Poisson statistics.

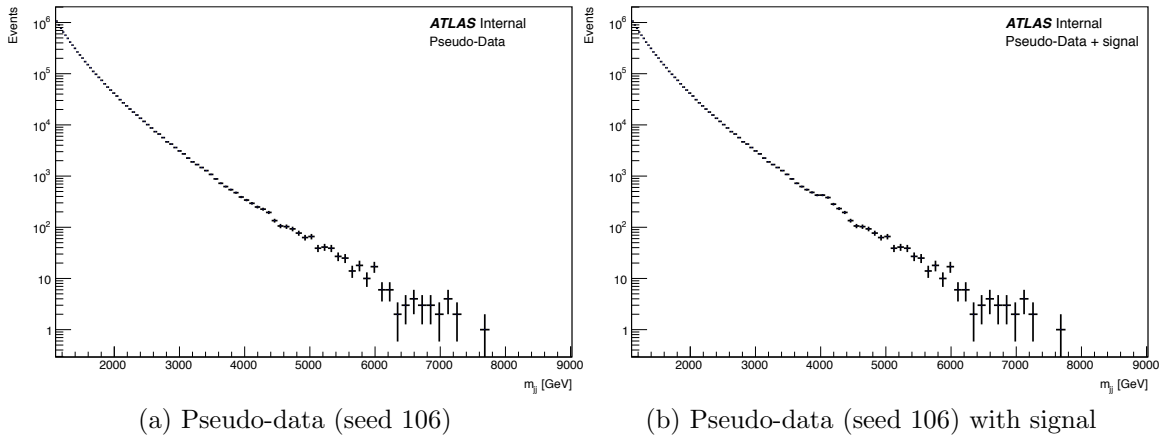


Figure 6.10: Pseudo-data distributions with (a) no injected signal and (b) injected signal. The injected signal is a resolution-width Gaussian with 250 events at 4070 GeV. The binning of the histograms is equal to the dijet mass resolution (see Figure 7.12).

#### 6.3.2.1 Window Selection

Starting from a window center of 1416 GeV and sliding up to 6407 GeV, SWiFt first selects a window size for each window center. The selection is made from 20 window sizes, linearly spaced, in a range of 30% to 100% of the window center. For each window center, multiple nominal background-only fits are performed with different window sizes and the one with the best  $\chi^2$  p-value is picked. The size selected (in percentage) around each window center is shown in Figure 6.11. The corresponding

mass ranges are shown in Figure 6.12. The red lines show the upper and lower edges of the window and the diagonal line represents the window centers.

For the signal-injected case, an interesting observation can be made. In Figure 6.12 (b), the window size increases up to 2.6 TeV, decreases from 2.6 TeV to 3.1 TeV, and increases once again beyond 3.1 TeV. This is caused by the injected signal moving into and then across the window. At first, the window selection procedure tries its best to keep the signal out of the window (seen by the decrease from 2.6 TeV to 3.1 TeV). After a certain point, it can no longer avoid including the signal. Beyond that point the window size increases. This pattern will be seen again in the signal injection studies detailed later.

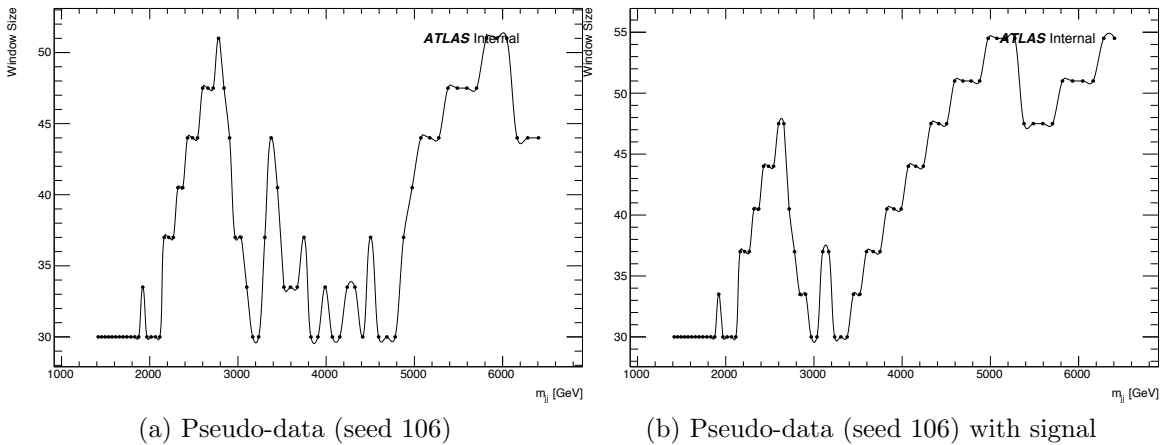


Figure 6.11: The y-axis represents the window size (as a percentage of the window center) picked for each window center (range from 1416 – 6407 GeV). The choice is made by picking the window size that gives the best  $\chi^2$  p-value for the nominal background-only fit. (a) No injected signal. (b) Resolution-width Gaussian with 250 events injected at 4070 GeV.

### 6.3.2.2 Resonance Search

After the window sizes are fixed, the resonance search is performed using resolution-width Gaussian signals. Figure 6.13 shows which set of functions are selected for each window - nominal or alternate. Notice that for the signal-injected case (Figure 6.13

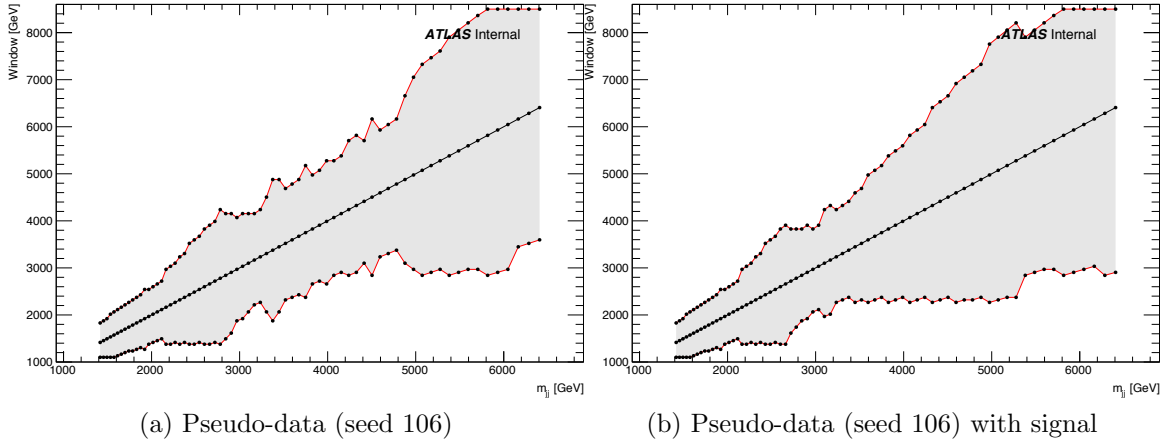


Figure 6.12: The y-axis represents the window size (in GeV) picked for each window center (range from 1416-6407 GeV). The upper red curve shows the high-mass edge and the lower red curve shows the low-mass edge. The diagonal black line represents the window centers. The choice is made by picking the window size that gives the best  $\chi^2$  p-value for the nominal background-only fit. (a) No injected signal. (b) Resolution-width Gaussian with 250 events injected at 4070 GeV.

(b)), when the signal starts to enter the window from the right at 3.1 TeV, the 4-parameter function is preferred. This is because, having some extra flexibility, the 4-parameter function is better able to handle a fluctuation at the window edge. With no signal present (Figure 6.13 (a)), the 3-parameter function is chosen at the same mass.

The  $\chi^2$  p-values for the chosen set of functions are shown in Figure 6.14. As in the previous plots, the effect of the injected signal is clear. At 3.1 TeV, the injected signal is just at the right edge and this causes the  $\chi^2$  p-value to become worse. As the injected signal slides into the window, the  $\chi^2$  p-value becomes substantially worse yet. When the window is centered at the injected signal mass at 4.07 TeV, the  $\chi^2$  p-value of the signal+background fit recovers completely<sup>5</sup>. The structures visible in Figure 6.14 (b) are a universal characteristic of the presence of a signal. This is

<sup>5</sup>A negative signal is extracted as a result of performing a signal+background fit right next to the injected signal. The background component is pulled upwards due to the presence of the injected signal. This causes the signal component to extract a negative signal to the left and right side of the injected signal.

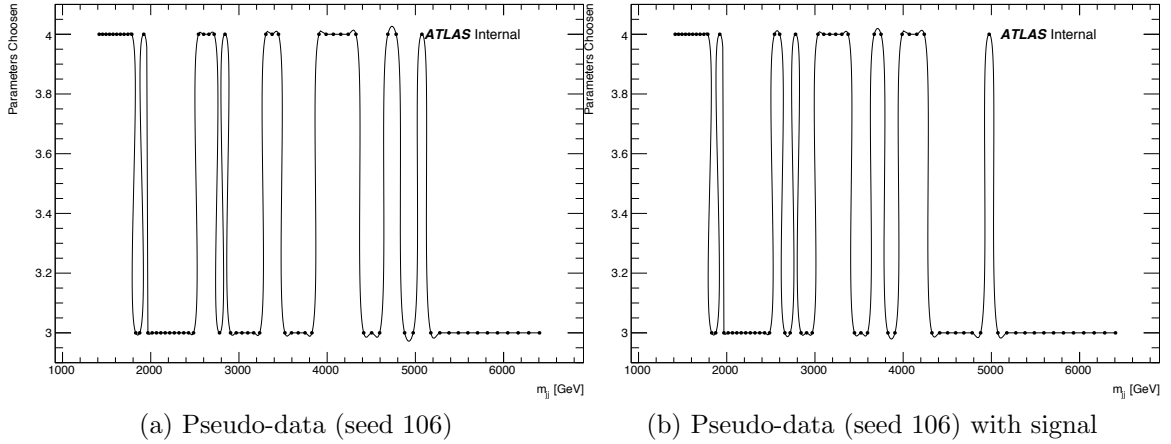


Figure 6.13: The y-axis represents the background function (nominal or alternate) selected at each window center. The nominal and alternate functions are the 3 and 4-parameter dijet functions, respectively. (a) No injected signal. (b) Resolution-width Gaussian with 250 events injected at 4070 GeV.

expected when the signal that one is fitting is not located at the true signal.

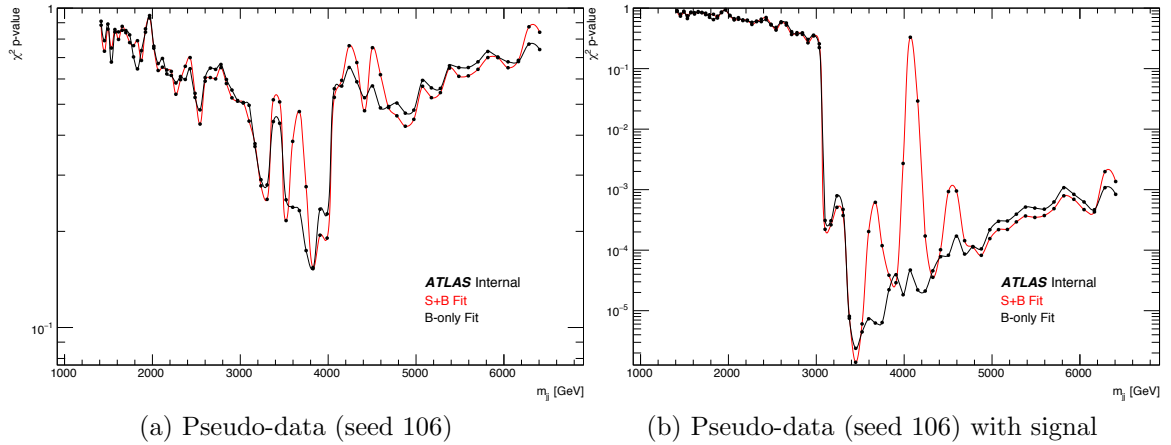


Figure 6.14: The y-axis shows the  $\chi^2$  p-value for the signal+background (in red) and background-only (in black) fits chosen in each window (Note: a p-value of 0.02 is roughly  $2\sigma$ ). (a) No injected signal. (b) Resolution-width Gaussian with 250 events injected at 4070 GeV.

The signal extracted from the signal+background fits is shown in Figures 6.16. The corresponding local p-values are shown in Figures 6.15. Figure 6.15 (b) suggests that a  $6\sigma$  signal is present in the distribution, which is, of course, the injected signal!

The best-fit window, centered at 4070 GeV, is shown in Figure 6.17. The signal

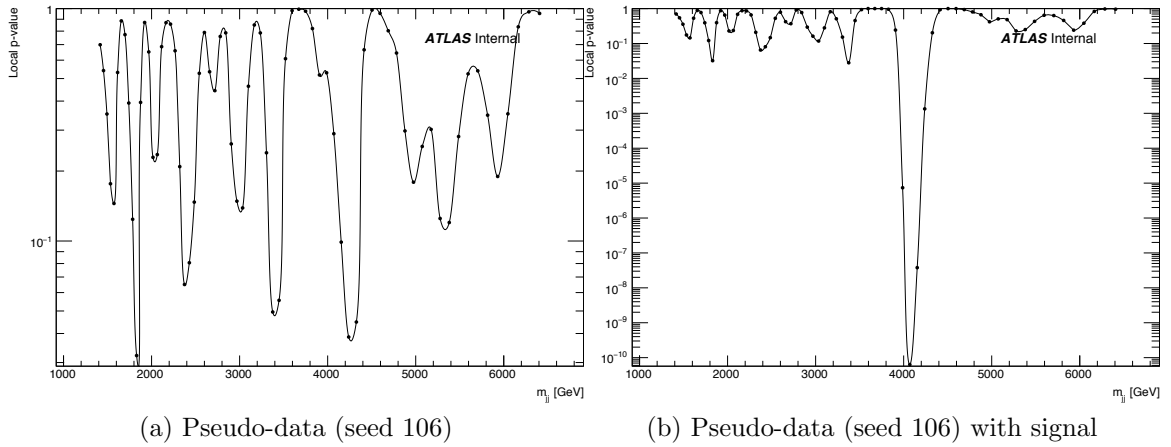


Figure 6.15: The y-axis shows the local p-value calculated from the LLHR at each window center. (a) No injected signal. (b) Resolution-width Gaussian with 250 events injected at 4070 GeV. The injected signal is seen with a local p-value of  $6e^{-10}$  ( $6\sigma$ ).

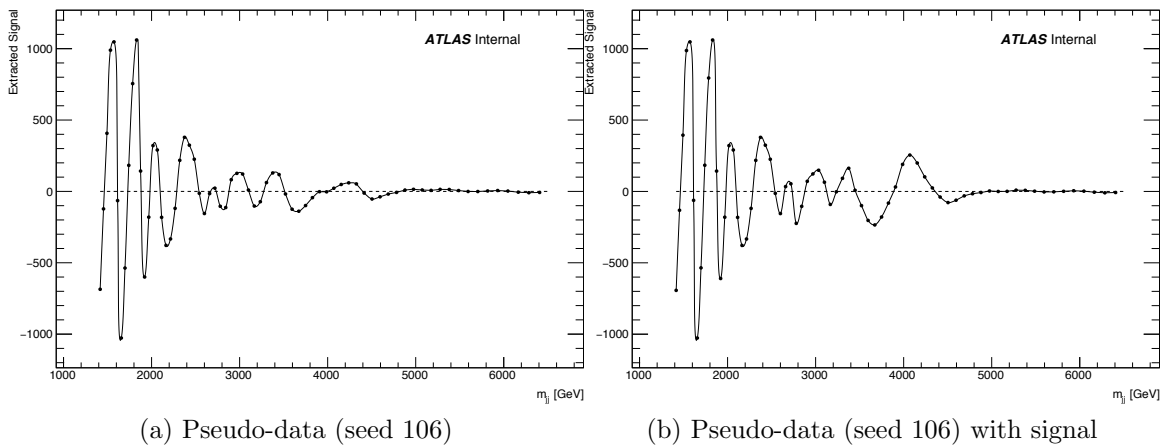


Figure 6.16: The y-axis shows the signal extracted by the signal+background fit at each window center. (a) No injected signal. (b) Resolution-width Gaussian with 250 events injected at 4070 GeV.



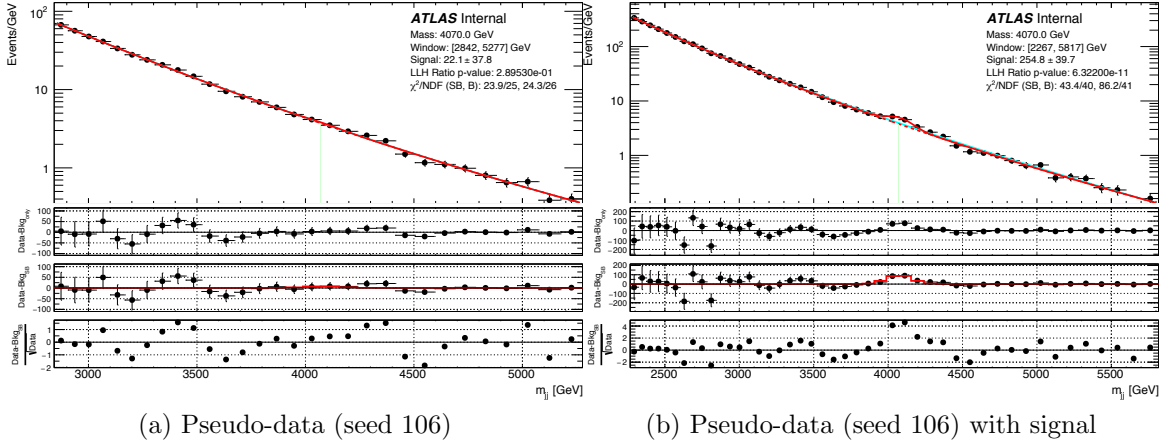


Figure 6.17: Window centered around 4070 GeV. (a) No injected signal. (b) Resolution-width Gaussian with 250 events injected at 4070 GeV. The signal extracted is  $255 \pm 40$  events.

extracted in Figure 6.17 (b) is  $255 \pm 40$  events, very consistent with the 250 injected events.

### 6.3.2.3 The SWiFt Background

At last, the SWiFt background is produced. Figure 6.18 (a) shows the background estimation for the no-signal-injected case and Figure 6.18 (b) shows a global 4-parameter fit to the pseudo-experiment. It is seen that the SWiFt background produces a much better model for the pseudo-experiment than the global 4-parameter fit.

Figure 6.19 shows the SWiFt background for the signal-injected distribution. Since a significant excess was identified (p-value less than 0.001), signal subtraction is performed. Figure 6.19 (a) shows the SWiFt background compared to the pseudo-experiment. Figure 6.19 (b) shows the SWiFt background compared to the true background (i.e., the pseudo-experiment without the signal). For comparison, Figure 6.19 (c) shows the global 4-parameter fit to the signal-injected pseudo-experiment.

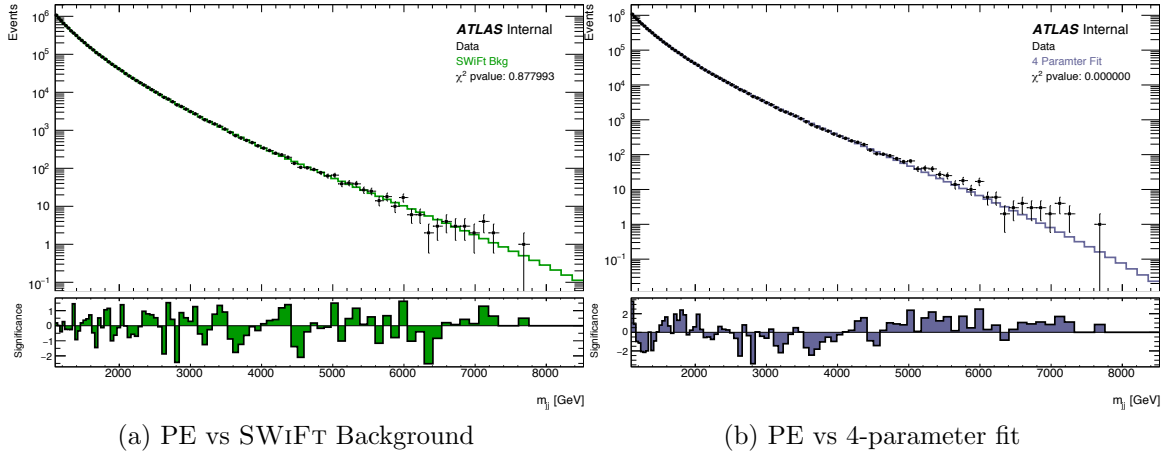


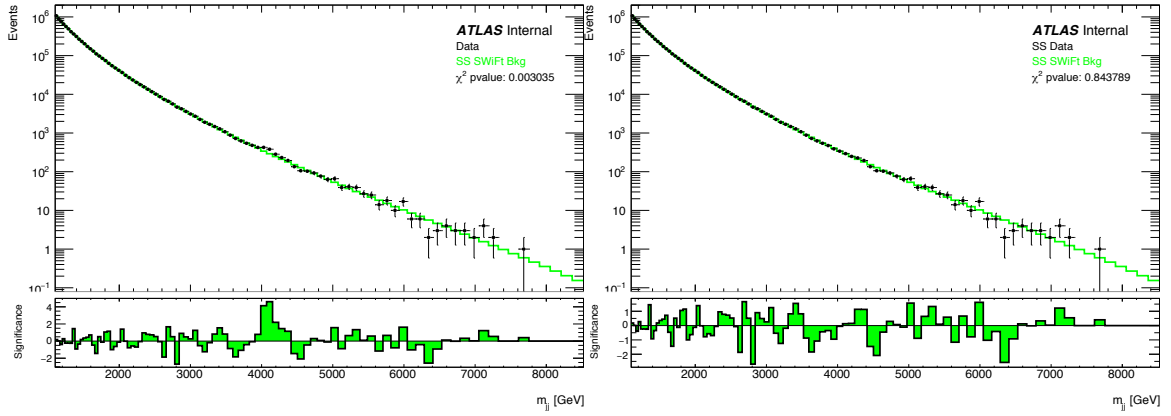
Figure 6.18: (a) The SWiFT background for Pseudo-data (seed 106) with no injected signal. (b) 4-parameter dijet function global fit. Note the difference in the scale of the significance plots at the bottom of the two figures.

### 6.3.3 Average Window Size and the SWiFT Background

The SWiFT results obtained from one pseudo-experiment in the previous section appear promising. However, a result from one distribution is not sufficient to fully characterize the performance of the method. Thus, in this and the following sections, results are shown by averaging over SWiFT results from many pseudo-experiments drawn from the smoothed MC.

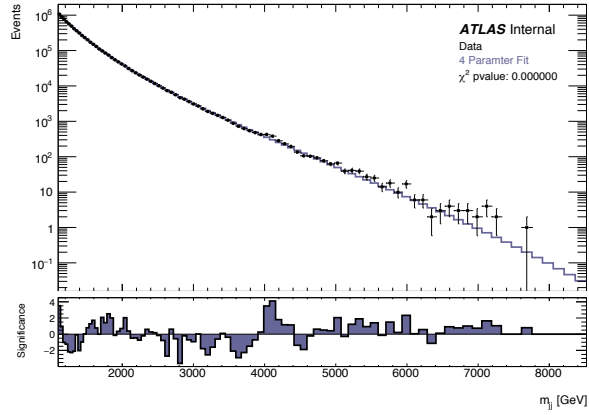
Figure 6.20 shows the window size averaged over 1000 pseudo-experiments. The solid black curve in Figure 6.20 (a) shows the average window as a percentage of the window center. Figure 6.20 (b) shows the window size in GeV - the dotted black line represents the window center and the two black curves show the average window edges for each window center. The grey curves show the windows for each of the 1000 pseudo-experiments overlaid. This demonstrates SWiFT's ability to identify reasonable window sizes in the presence of statistical variations.

An overlay of all the SWiFT backgrounds (in grey) produced from each of the 1000 pseudo-experiments is shown in Figure 6.21 (a), with their average shown by the black curve. The area mapped by the backgrounds from the pseudo-experiments (in



(a) PE vs SS Background

(b) SS PE vs SS Background



(c) PE vs 4-parameter Fit

Figure 6.19: The SWIFT background and the global 4-parameter fit to the signal injection case is shown here. (a) Signal-injected pseudo-experiment vs signal-subtracted SWIFT background. (b) Signal-subtracted pseudo-experiment vs signal-subtracted SWIFT background. (c) Global 4-parameter fit to Signal-injected pseudo-experiment.

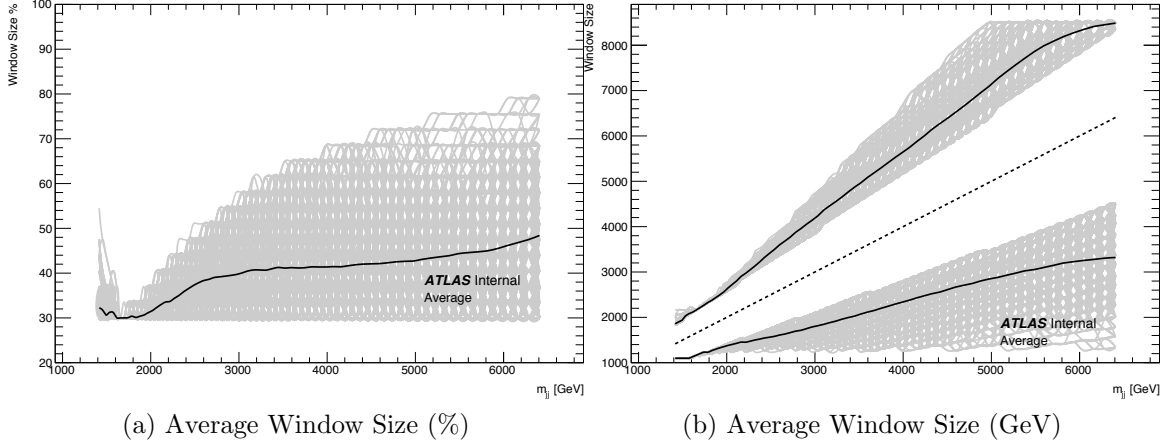


Figure 6.20: Average window size as chosen by the automatic window selection procedure. (a) The average size (%) is shown for each window center. The grey curves show sizes for each PE and the black curve is the average. (b) The average size (GeV) is shown for each window center. The diagonal dotted line shows the window center, the solid curves show the average upper and lower edges of the window and the grey curves show the window size from each PE.

grey) shows the statistical uncertainty. It is larger at higher masses due to the low statistical precision at the tail. In Figure 6.21 (b), the average is then compared to the parent distribution, i.e. the smoothed MC fit. The difference between the average SWIFT background and the smoothed MC is less than  $0.25\sigma$  everywhere.

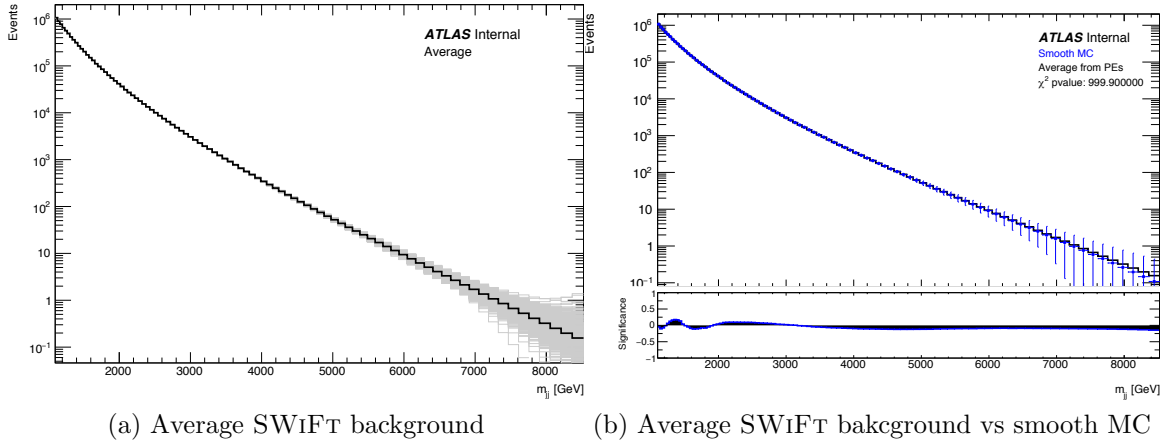


Figure 6.21: (a) Average of all SWIFT backgrounds obtained from each PE. The grey curves shown the SWIFT background for each PE. (b) The average size (%) is shown for each window center.

### 6.3.4 Spurious Signal

Spurious signal is defined as the amount of signal extracted from a distribution with no real signal present, and it quantifies the amount of bias in the extracted signal. It is measured by averaging the extracted signal from 1000 pseudo-experiments drawn from the smooth MC. Figure 6.22 shows the spurious signal (a) and its significance (b) using the full SWiFT procedure for three different signal shapes: resolution Gaussian, 7% Gaussian and  $q^*$ .

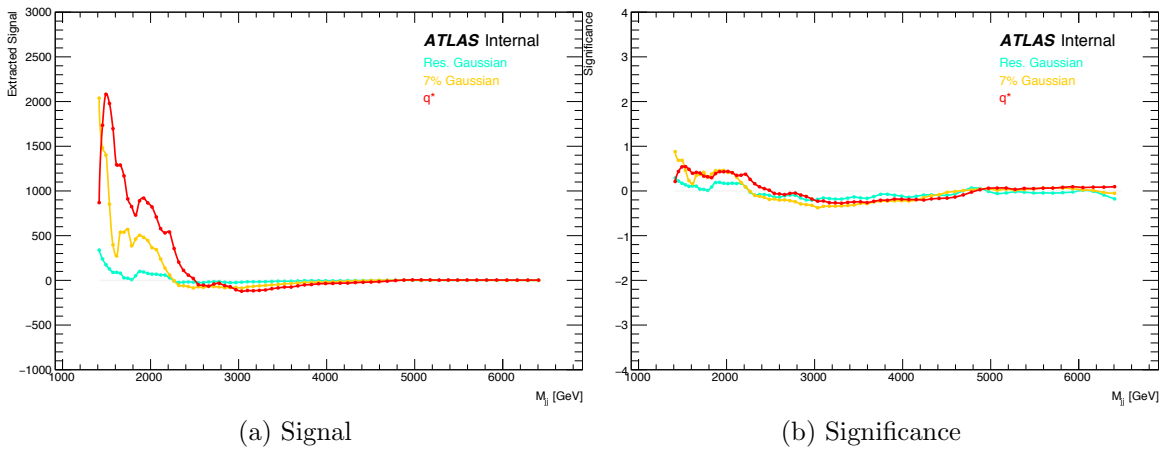


Figure 6.22: (a) Spurious signal and (b) its significance for three signals: resolution width Gaussian, 7% width Gaussian and  $q^*$ . Significance is defined as the extracted signal divided by its uncertainty. Each curve on the plots is obtained by averaging over a 1000 PEs.

The spurious signal is generally less than  $0.5\sigma$ . Such values are acceptable for a general search, although smaller values would be desirable for a precision measurement. The low mass regions have somewhat larger spurious signal, however, this may be due to residual over-fitting of the large deviations in the underlying MC (recall Figure 6.9). Another point to keep in mind is that the shape of the smooth MC differs from the data; therefore, these spurious signal results are at best an approximation (a good one) of what one might expect in the data.

### 6.3.5 Linearity

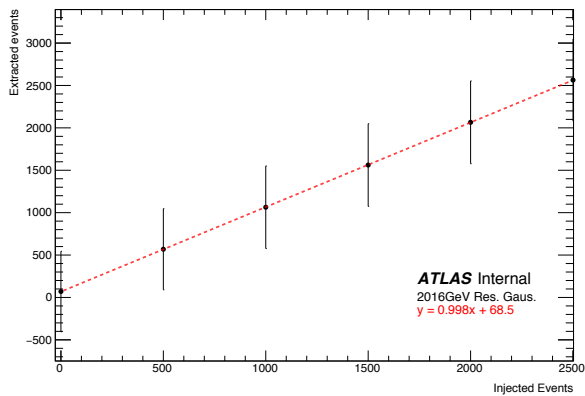
Linearity studies were performed to determine SWiFT's ability to accurately recover injected events from test distributions. These studies were done by injecting signal into the smoothed MC at three masses: 2016 GeV, 4070 GeV and 6047 GeV, and producing an ensemble of 1000 pseudo-varied distributions. The extracted signal was then calculated by averaging over the extracted signals from each pseudo-experiment.

Results are shown in Figure 6.23 and 6.24 for resolution-width Gaussian and  $q^*$  signals, respectively. The error bars are obtained from the standard deviation of the distribution of extracted signal events. They are largely the same as the spectrum is background-dominated in the region of the injected signal. The linear relationship between the injected and extracted signal is evident, and the linear fits (dotted red lines) confirm this. For all masses tested, the slope is close to unity which indicates that SWiFT is successfully recovering the injected signal. The offsets represents the spurious signal for each mass and are consistent with what is shown in the previous section.

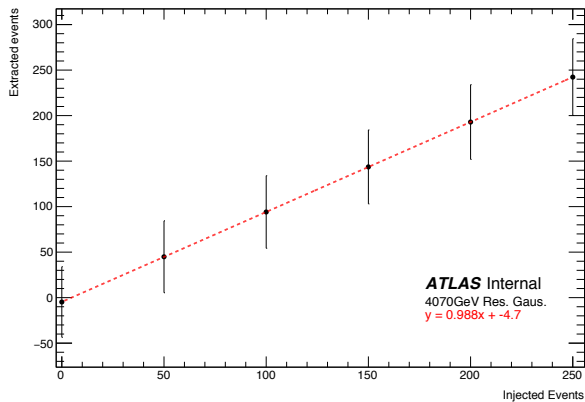
### 6.3.6 Signal Injection and Sensitivities

This section explores the expected statistical significance as a function of the signal size. It also demonstrates SWiFT's performance in the presence of increasing signal.

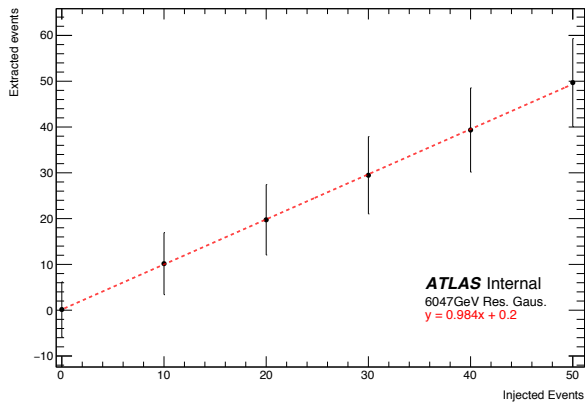
Increasing amounts of signal are injected into the smoothed MC and 1000 pseudo-experiments are drawn for each. Four outputs are then studied: the window size, the background parameter chosen (nominal or alternate), the number of signal events extracted and the local p-value. The first three outputs are averaged over the 1000-PE ensemble. For the local p-value, the median is used rather than the mean as the p-value distributions are highly asymmetric; the vast majority of the p-values will be peaked close to zero with a falling tail towards one. Consequentially, the mean does not accurately reflect the most probable result.



(a) 2016 GeV

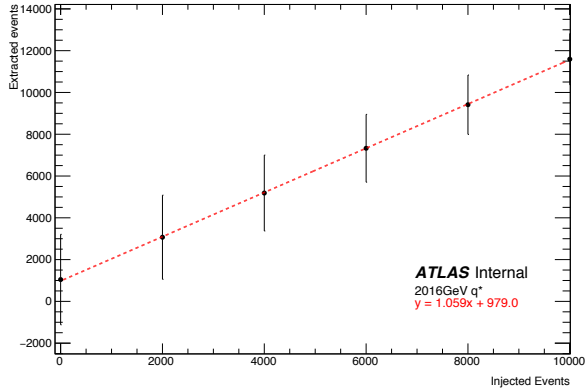


(b) 4070 GeV

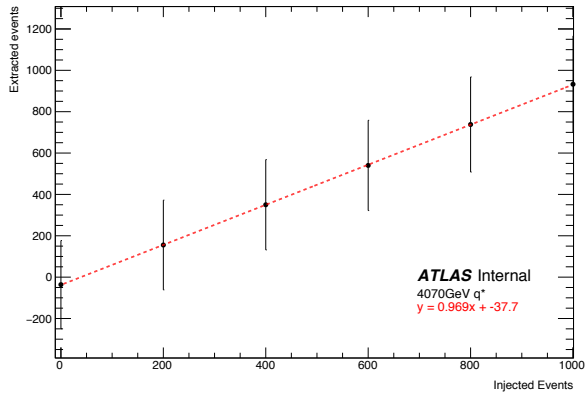


(c) 6047 GeV

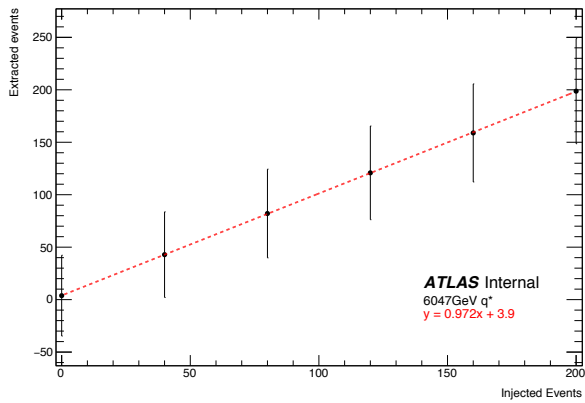
Figure 6.23: Linear relationship between injected and extracted signal shown for resolution width Gaussian signals at 2016 (a), 4070 (b) and 6047 (c) GeV. Each point for the extracted signal is calculated by taking the average of 1000 PEs. The error bars are obtained from the standard deviation of the distribution of extracted signal events from the PEs.



(a) 2016 GeV



(b) 4070 GeV



(c) 6047 GeV

Figure 6.24: Linear relationship between injected and extracted signal shown for  $q^*$  signals at 2016 (a), 4070 (b) and 6047 (c) GeV. Each point for the extracted signal is calculated by taking the average of 1000 PEs. The error bars are obtained from the standard deviation of the distribution of extracted signal events from the PEs.



The background function chosen and the average window sizes picked (for each window) for resolution-width Gaussian signals at three masses are shown in Figures (a) and (b) of Figures 6.25, 6.26 and 6.27. Averages for  $q^*$  injections are shown in Figures (a) and (b) of Figure 6.28, 6.29 and 6.30. On average, SWIFT prefers to pick the 3-parameter function more often than the 4-parameter function in each window. However, whenever the signal is at the edge of a window (left or right edge), the 4-parameter function is preferred over the 3-parameter function. This supports the approach of approximating a more complex global spectrum (in this case, drawn from a 6-parameter fit to the smooth MC) using simpler functions in limited ranges. Window sizes are successfully picked in the presence of increasing signal. The effect of the injected signal sliding across the window can be seen in the figures. The window sizes continue to grow until the right edge of the window reaches the injected signal. Then, the windows shrink to avoid pulling the signal into the window. The larger the injected signal, the smaller the windows becomes. As the window center gets closer to the injected signal, the window pulls in the injected signal and continues to grow (to improve the  $\chi^2$  p-value).

Next, the average number of signal events extracted and the median of the local p-values are studied. Figures 6.25, 6.26 and 6.27 (c) and (d) show these results for the resolution-width Gaussian and Figures 6.28, 6.29 and 6.30 (c) and (d) show them for the  $q^*$  signals. For windows centered at the mass of the injected signal, maximum signal is extracted and the most significant local p-values are achieved. The figures show the number of signal events required to produce a local p-value of  $3\sigma$ . Window centers adjacent to the injected signal pick up negative signals, the expected behavior described in Footnote 5. For larger injected signals, the negative signal extracted becomes proportionally larger. The structure (peak at the injected signal and dips around it) in the extracted signal is universally observed in any fitting procedure.

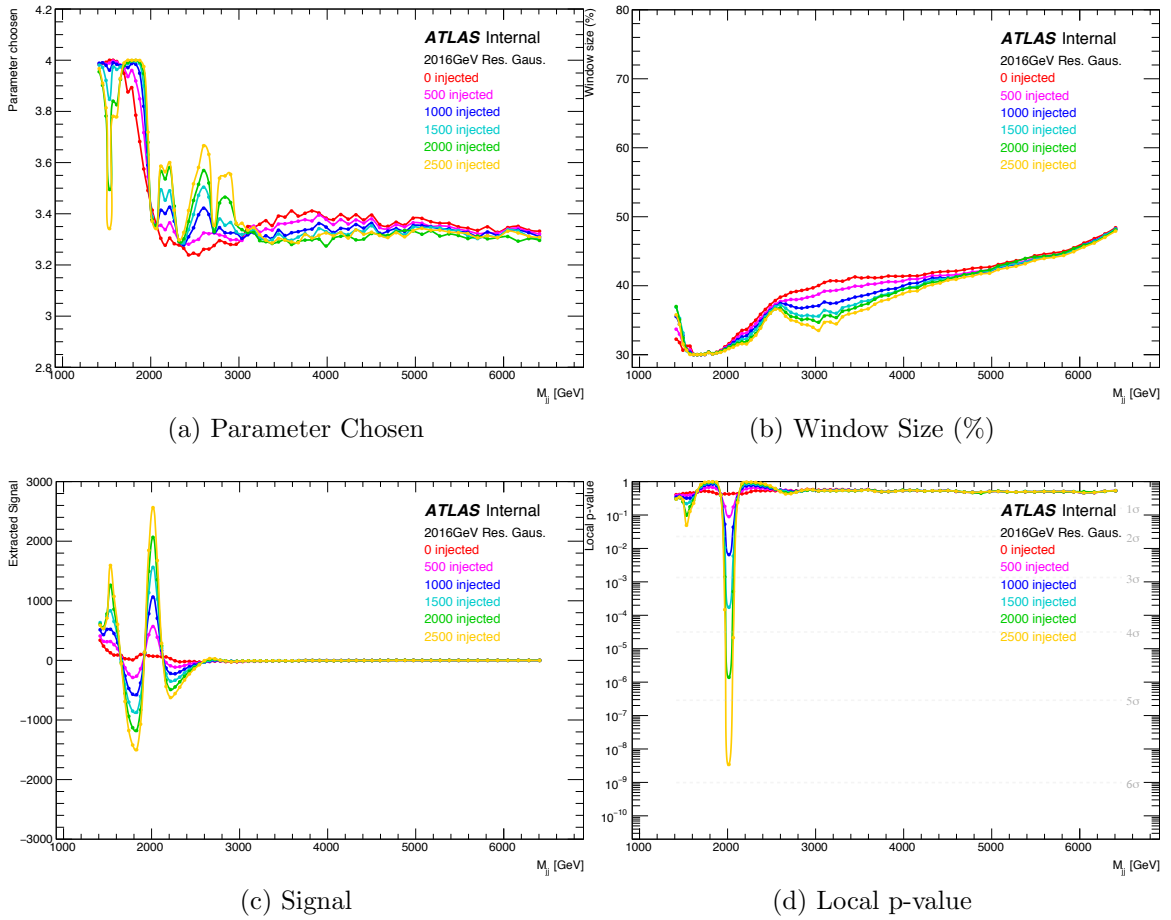


Figure 6.25: Resonance scan results for a resolution-width Gaussian signal injected at 2016 GeV: (a) background parameter chosen (3- vs 4-parameter), (b) window size, (c) number of extracted signal events and (d) local p-value. Each curve, for each amount of injected signal, is a result of averaging over 1000 PEs.

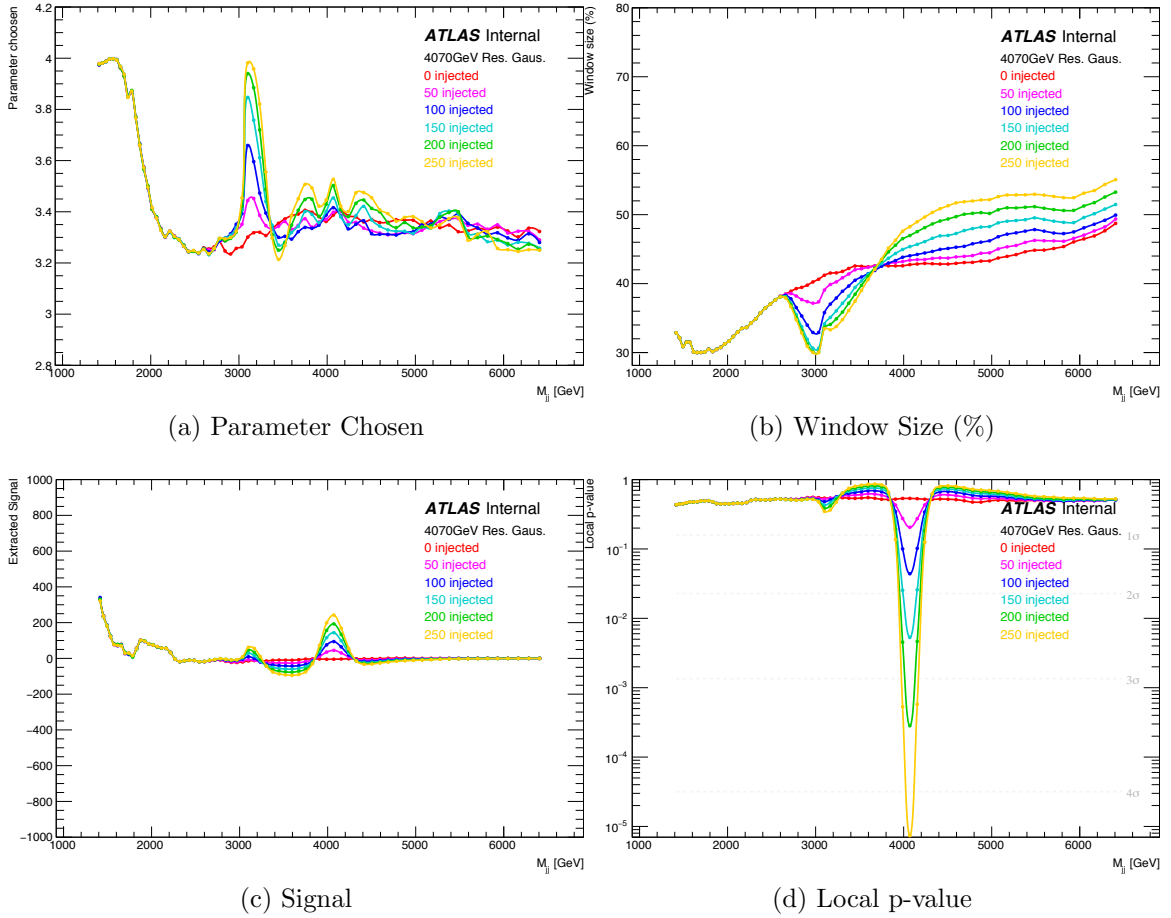


Figure 6.26: Resonance scan results for a resolution-width Gaussian signal injected at 4070 GeV: (a) background parameter chosen (3- vs 4-parameter), (b) window size, (c) number of extracted signal events and (d) local p-value. Each curve, for each amount of injected signal, is a result of averaging over 1000 PEs.

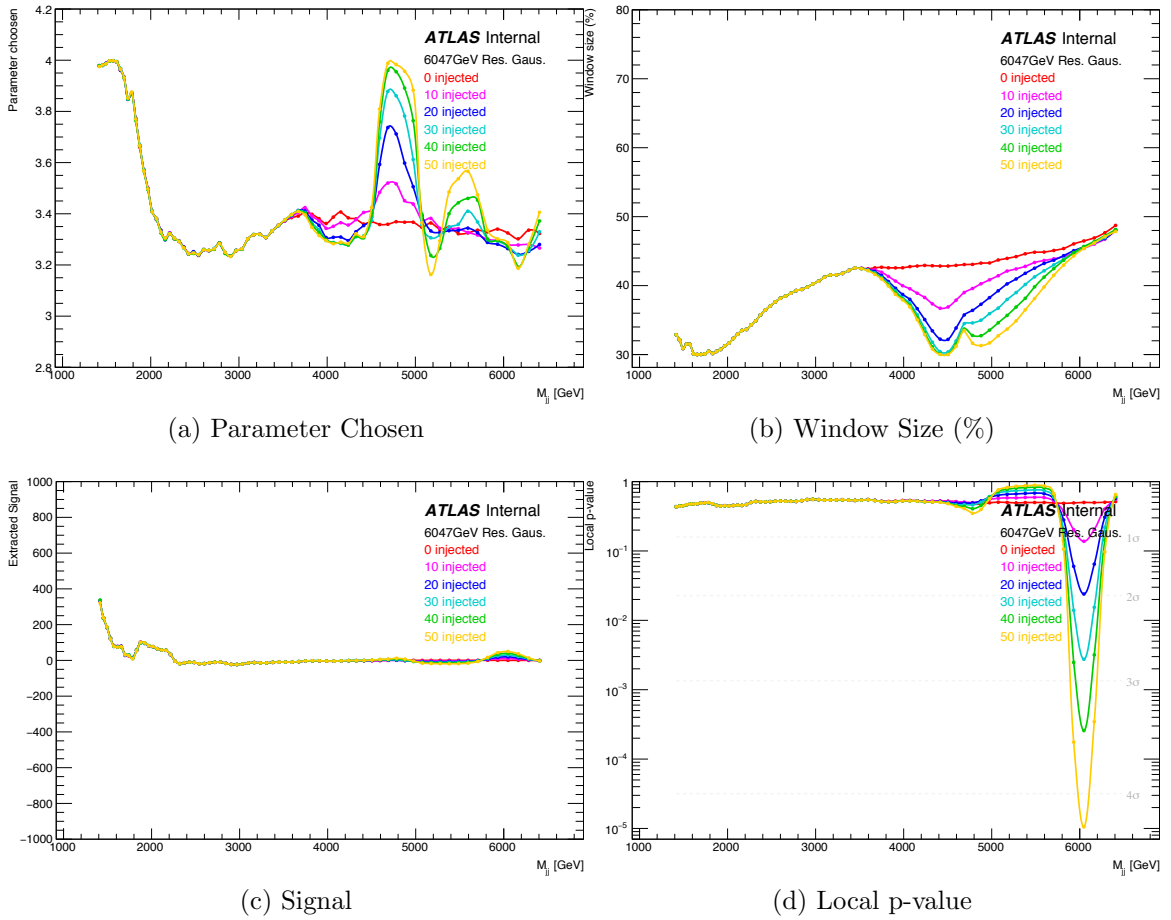


Figure 6.27: Resonance scan results for a resolution-width Gaussian signal injected at 6047 GeV: (a) background parameter chosen (3- vs 4-parameter), (b) window size, (c) number of extracted signal events and (d) local p-value. Each curve, for each amount of injected signal, is a result of averaging over 1000 PEs.

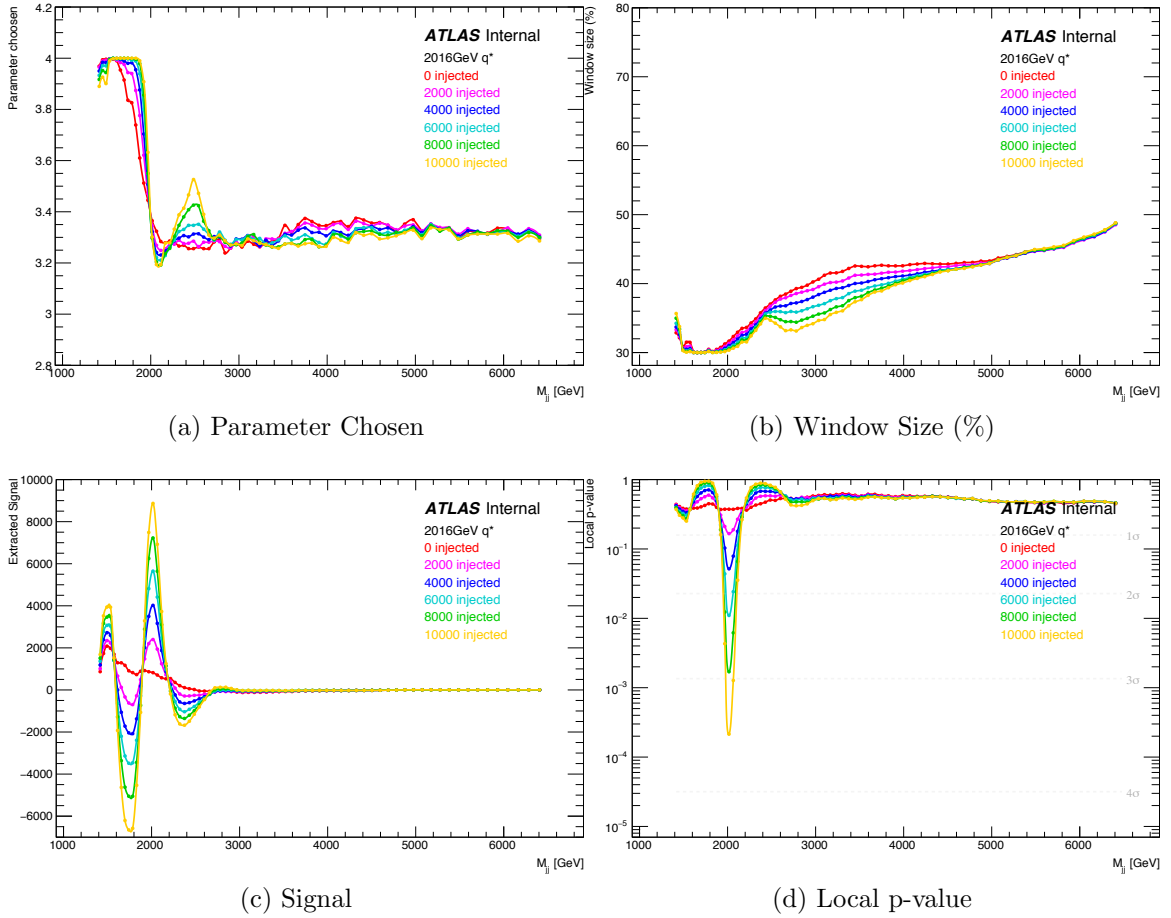


Figure 6.28: Resonance scan results for a  $q^*$  signal injected at 2016 GeV: (a) background parameter chosen (3- vs 4-parameter), (b) window size, (c) number of extracted signal events and (d) local p-value. Each curve, for each amount of injected signal, is a result of averaging over 1000 PEs.

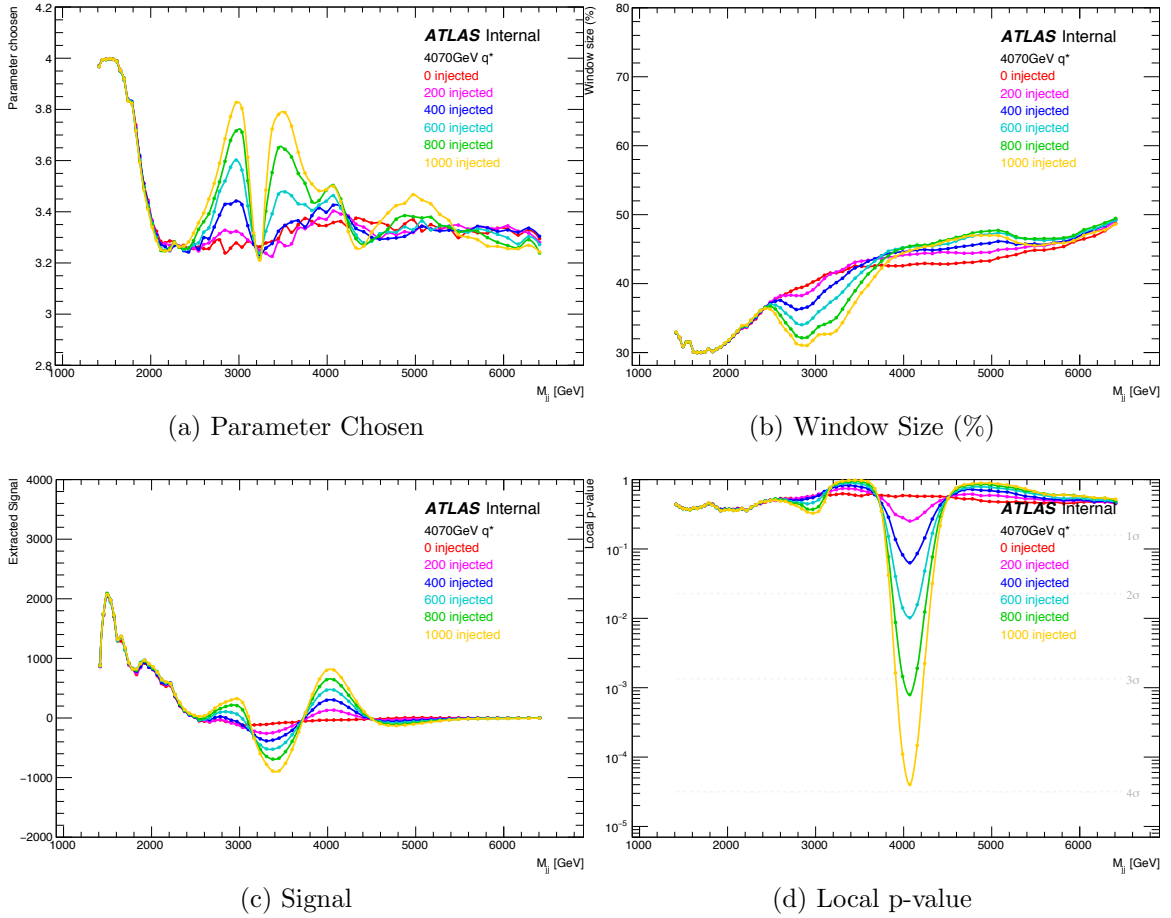


Figure 6.29: Resonance scan results for a  $q^*$  signal injected at 4070 GeV: (a) background parameter chosen (3- vs 4-parameter), (b) window size, (c) number of extracted signal events and (d) local p-value. Each curve, for each amount of injected signal, is a result of averaging over 1000 PEs.

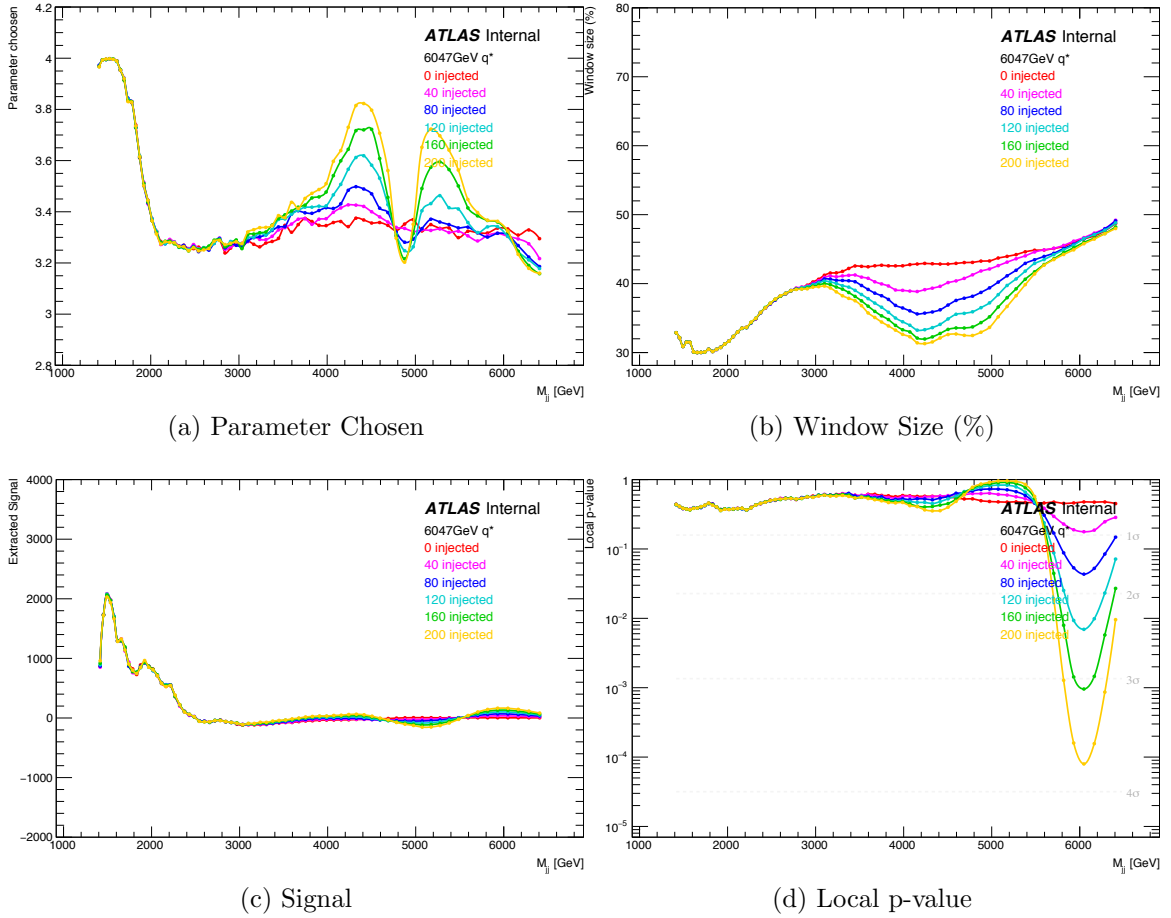


Figure 6.30: Resonance scan results for a  $q^*$  signal injected at 6047 GeV: (a) background parameter chosen (3- vs 4-parameter), (b) window size, (c) number of extracted signal events and (d) local p-value. Each curve, for each amount of injected signal, is a result of averaging over 1000 PEs.

## CHAPTER 7

# Dijet Analysis Selection & Validation

In the previous chapters, jet production, reconstruction and calibration was discussed in detail. Using the calibrated jets as inputs, this chapter will begin the discussion of the dijet analysis. The selection and validation of the dijet data will be detailed.

This chapter will show that the data is well-understood, but the available MC is not good enough to serve as a background. Thus, the analysis uses the data-driven SWIFT method to model the background.

### 7.1 Dijet Event Selection

The dijet analysis presented in this thesis was conducted on a total of  $37 \text{ fb}^{-1}$  of data collected by the ATLAS detector with a center-of-mass energy of 13 TeV. The data was collected in the year 2015 ( $3.5 \text{ fb}^{-1}$ ) and 2016 ( $33.5 \text{ fb}^{-1}$ ). Dijet events were identified by applying a number of cuts designed to select good quality events. The cuts are listed in Table 7.1, known as the *cut-flow*, which shows the number of events that pass every selection step (each selection step will be detailed in the following sections). The cuts are classified into three groups: event selection, object selection, and analysis selection.



Table 7.1: The event cut-flow table showing the number of events that pass each selection stage. The cuts are classified into three groups: event selection (event quality, good run list (GRL) and primary vertex cuts), object selection (full triggers, high level trigger (HLT) and jet cuts), and analysis selection (leading jet  $p_T$ ,  $m_{jj}$ ,  $y^*$  cuts).

Selection	$N_{\text{events}}$
All events	1,682,839,275
LAr Quality	1,680,323,020
Tile Quality	1,680,232,308
Core Quality	1,679,301,246
Primary Vertex	1,678,594,582
Full Triggers	1,520,215,165
2 jets $p_T > 60$ GeV	1,409,142,270
Lead jet $p_T > 360$ GeV	150,694,315
GRL Selection	147,028,750
HLT j380	110,618,942
Jet Cleaning	110,618,942
Lead jet $p_T > 440$ GeV	48,682,995
$m_{jj} > 1100$ GeV	25,564,160
$ y^*  < 0.6$	7,533,433

### 7.1.1 Event Selection

Event selection cuts are made to ensure good quality events. The Good Run List (GRL) selection, LAr, Tile, Core quality and primary vertex selection cuts fall under this category.

Data recorded by the detector can include events where certain subdetector systems suffer from issues such as non-functional cells, bad cell signals, noise bursts and corrupted data. To deal with this issue, a GRL is maintained that identifies the subset of the data where the detector was optimally functioning. The GRL selection then removes events that are not part of the the list. After the GRL selection is made, the events are scanned for cases that still have subdetector system errors. The LAr/Tile quality cuts perform this action by discarding events that have erroneous ECal/HCal signals. The Core quality cut removes events that are incompletely built.

In a collision event, there are multiple interactions that produce many tracks.

The points at which the interactions occur are known as vertices. The vertex that is associated to the highest scalar sum of the transverse momentum square of tracks ( $\sum p_T^2(track)$ ) emerging from it is known as the primary vertex. To maximize the probability of the primary vertex giving rise to the dijet event, the primary vertex selection requires there to be at least two tracks associated to it.

## 7.1.2 Object Selection

After good events are selected, events with at least two good jets are selected next. This is done by a combination of cuts known as the object selection cuts. These include the jet trigger cuts, the jet cleaning cut and the basic jet  $p_T$  cuts. The basic jet  $p_T$  cuts require each event to have at least two jets with  $p_T$  larger than 60 GeV. This removes events with low- $p_T$  pileup jets. The jet with the highest  $p_T$  is known as the *leading jet* and the jet with the second-highest  $p_T$  is called the *subleading jet*. The leading jet is required to have a  $p_T$  larger than 360 GeV. The jet trigger and cleaning selection are discussed next.

### 7.1.2.1 Jet Triggers

As described in the last subsection of Chapter 3, ATLAS has two kinds of triggers: the hardware-based L1 and the software-base HLT. Each HLT trigger is seeded from a L1 trigger. These triggers are object-specific, i.e. separate triggers exist for different objects like jets, photons, electrons, etc. Their names are written in the format: type-ofTrigger\_objectThreshold<sup>1</sup>. Requiring events to pass a trigger cut would guarantee the existence of the object in the event with  $p_T$  or  $E$  larger than the trigger threshold. Hence to select dijet events, each event is required to have at least two jets, with one passing the HLT\_j380 trigger (that is seeded from L1\_j100). This trigger was chosen as it was the lowest *unprescaled* trigger in 2016. Prescaling is the process of reducing

---

<sup>1</sup>An example of a L1 jet trigger that requires events to have a single jet with  $p_T$  larger than 50 GeV would be written as: L1\_j50.

the trigger rate by a factor known as the prescale factor. It is performed on lower  $p_T$  triggers due to the inability to record the extremely large number of low- $p_T$  triggered events.

As seen in Table 7.1 there is an additional trigger selection known as Full Triggers. This selection requires each event to pass any trigger from the following set: L1\_j75, L1\_j100, HLT\_j360, HLT\_j380, HLT\_j400, HLT\_3j175, HLT\_4j85, HLT\_4j100 where the last three triggers are tri-jet and quad-jet triggers. This additional trigger information is used for trigger studies and by other jet analyses.

### 7.1.2.2 Jet Cleaning

Jets produced from genuine hard-scattering events must be differentiated from jets produced from non-collision backgrounds [108]. The main sources of these backgrounds are:

- Beam induced background: Due to proton losses upstream of the interaction point, secondary cascades that lead to very high energy muons can be falsely reconstructed as high energy jets.
- Cosmic-ray showers: If a high energy cosmic ray shower overlaps with the collision event, it can appear as a fake jet.
- Calorimeter noise: Most of the calorimeter noise is taken into account and removed from events during the standard data quality checks. However, a small portion of the noise remains undetected and appears in the calorimeters as jets. It is caused by either coherent or individually pathological calorimeter cells.

To differentiate fake jets from genuine jets, cuts are made on several detector-level quantities. These quantities are categorized into three main types: LAr signal pulse shape variables, energy ratio variables and track-based variables.

- LAr signal pulse shape variables: The measured signal pulses obtained from the cells of the LAr detector are compared to the expected pulses from simulation and a quality factor ( $Q_{\text{cell}}^{\text{LAr}}$ ) is defined that quantifies the differences of the two pulses. It is stored as a 16-bit integer and can take values from 1 to 65535. Based on this quality factor, three different variables are defined:
  - $\langle Q \rangle$  is the average jet quality. It is defined as the energy-squared weighted average of  $Q_{\text{cell}}^{\text{LAr}}$  in the jet and is normalized to be between 0 and 1.
  - $f_{\text{Q}}^{\text{LAr}}$  is the fraction of poor signal quality LAr cells in a jet. Poor signal is defined as  $Q_{\text{cell}}^{\text{LAr}} > 4000$ .
  - $f_{\text{Q}}^{\text{HEC}}$  is the fraction of poor signal quality HEC cells in a jet.
  - $E_{\text{neg}}$  is the sum of the energy of all the cells with negative energy. Sporadic noise bursts can cause large negative energy values, therefore jets with large negative energy are discarded. Note that good jets can also have negative energy. It is small and mostly due to electronic and pile-up noise.
- Energy ratio variables: The energy deposited by fake jets have a different shower profile from the good jets, i.e. they tend to extend laterally in the calorimeter rather than longitudinally. This fact can help distinguish bad jets from good and three variables are defined to do so:
  - $f_{\text{EM}}$  is the ratio of the energy deposited in the electromagnetic calorimeter to the total energy of the jet.
  - $f_{\text{HEC}}$  is the ratio of the jet's energy deposited in the HEC calorimeter to the total energy.
  - $f_{\text{max}}$  is the maximum energy fraction in any layer of the calorimeter system to the total jet energy. This includes all the layers of the calorimeter system: the layers of the LAr, Tile, HEC, EMEC and FCal.

- Track-based variables: The last set of variables are based on the fact that most real jets contain charged hadrons that leave track in the ID and fake jets do not. The variable based on tracks is:

- $f_{\text{ch}}$  is the fraction of the jet  $p_{\text{T}}$  measured by the tracks of the ID.

Based on cuts made on the variables described above, two categories of bad jets can be obtained: looseBad or tightBad. The jet cleaning cut made in this analysis is looseBad and if any of the three leading jets in an event satisfies any of the following criteria, the event is removed:

1.  $f_{\text{HEC}} > 0.5$  and  $|f_{\text{Q}}^{\text{HEC}}| > 0.5$  and  $\langle Q \rangle > 0.8$ ,
2.  $|E_{\text{neg}}| > 60$  GeV,
3.  $f_{\text{EM}} > 0.95$  and  $f_{\text{Q}}^{\text{LAr}} > 0.8$  and  $\langle Q \rangle > 0.8$  and  $|\eta| < 2.8$ ,
4.  $f_{\text{max}} > 0.99$  and  $|\eta| < 2$ ,
5.  $f_{\text{EM}} < 0.05$  and  $f_{\text{ch}} < 0.05$  and  $|\eta| < 2$ ,
6.  $f_{\text{EM}} < 0.05$  and  $|\eta| \geq 2$ .

### 7.1.3 Analysis Selection

After the event and object selections are made, good quality dijet events remain. At this stage the dijet-analysis-specific selections are made. The leading jet of every event is required to be greater than 440 GeV, the dijet invariant mass is set to be larger than 1100 GeV, and a cut of  $|y^*| < 0.6$  is made. The leading jet  $p_{\text{T}}$  and invariant mass cut values are determined by the efficiency of the HLT\_j380 trigger, i.e. the  $p_{\text{T}}$  and  $m_{jj}$  values are picked such that the trigger is more than 99.5% efficient. The  $y^*$  cut value is picked to maximize the sensitivity of the analysis to new-physics particles that are produced via an s-channel process.

## 7.2 Dijet MC Simulation

A LO Monte Carlo simulation of the dijet spectrum was produced using the PYTHIA [69] generator. PYTHIA calculates the hard-scatter with a  $2 \rightarrow 2$  LO matrix element. Higher-order parton interactions are created during the parton shower stage of the simulation. The momentum distribution of the colliding partons is described using the NNPDF2.3 LO PDF set [109]. The simulation parameters of the underlying event, parton showering and hadronization are set using the A14 event tune [110]. Both of these are obtained by tuning their free parameters to match past data. After the dijet events are generated, they are propagated through a full simulation [111] of the ATLAS detector using the GEANT4 simulation toolkit [112]. GEANT4 simulates the response of all the subdetector systems to the MC generated events by taking into account the interaction of the particles with the different detector material, etc.

In the analysis, the MC simulation is used to cross-check the data distribution and perform resolution, trigger, and efficiency studies. Unfortunately, as will be seen, there are statistically significant differences between the data and MC. This prevents it from being used as a background model during the statistical analysis of the data.

## 7.3 Validation

Before performing the statistical analysis, the data distributions and their quality were thoroughly validated after applying the analysis selection cuts. This was done by performing two sets of comparisons in hundreds of histograms, comparing many low-level and high-level variables including event, cleaning, track, kinematic, and dijet system variables. Correlations between different variables were also studied. The first comparison was made between the data and the PYTHIA MC simulation. The second comparison was made by dividing the data into two subsets: the data collected in 2015 and the data collected in 2016. The data-MC comparisons provide an understanding

of how well the measured data agrees with expectation. It will be observed that the agreement is good in some variables and not as good in others. This is to be expected as the simulation, though quite good, is not perfect. Higher-order QCD effects are not included, showering and hadronization are based on phenomenological models, and the simulated detector is an imperfect (though pretty darn good) representation of the physical detector. These differences, though small, become significant given the high statistical precision of the dijet dataset. This makes it impossible to use the MC in the statistical analysis, however, it provides a useful tool for verifying that the data is well-understood. The data-data comparisons compare data accumulated with slightly different run conditions. These differences are not expected to substantially change the variables of interest, and this will be shown.

In the following subsections, the data-MC and data-data comparisons will be shown side-by-side for the following handful of important variables:

- the average number of interactions per bunch crossing ( $\langle\mu\rangle$ ), the number of primary vertices (NPV) and the number of jets in the events with  $p_T$  greater than 60 GeV (Figure 7.1),
- the LAr and HEC quality fraction (Figure 7.2),
- the fraction of the jet energy deposited in the EM and HEC calorimeters (Figure 7.3),
- the leading and subleading jet transverse momenta (Figure 7.4),
- the leading and subleading jet energies (Figure 7.5),
- the leading and subleading jet pseudorapidities (Figure 7.6),
- the leading and subleading jet azimuthal angles (Figure 7.7),
- the correlations between several kinematic variables:  $\eta$  vs  $p_T$ ,  $\eta$  vs  $E$  and  $\eta$  vs  $\phi$  (Figure 7.8),

- the dijet angular variables  $y^*$  and  $y_B$  (Figure 7.9),
- the dijet kinematic variables  $\Delta R$  and transverse momentum of the dijet system (Figure 7.10),
- the dijet invariant mass distribution (Figure 7.11).

Unless otherwise stated, the data-MC plots will be in the left column and the data-data plots will be in the right column. Each one-dimensional histogram will contain two distributions: one in dotted black and one colored blue. For the data-MC plots, the dotted black distribution will represent the full 2015+2016 dataset and the blue distribution will represent the MC. The MC will be normalized to the data. For the data-data plots, the dotted black and blue distributions will represent the 2016 and the 2015 datasets respectively. The 2015 data will be normalized to the 2016 data. The relative difference between the two distributions is shown at the bottom of each histogram. It is calculated by taking the difference of the two distributions and dividing by the blue one. At last, the dijet mass resolution (used to define the binning of the dijet invariant mass distribution) will be shown in Figure 7.12.

### 7.3.1 Event Variables

The first set of variables shown in Figure 7.1 are basic event variables. These are: the average interactions per bunch crossing ( $\langle\mu\rangle$ ), the number of primary vertices (NPV) and the number of jets with transverse momentum larger than 60 GeV ( $N_{jets} > 60$  GeV).

Differences in  $\langle\mu\rangle$ , also known as pile-up, are seen in both the data-MC and data-data comparisons. For the former, differences are expected as it is hard for the MC simulation to replicate the exact LHC run conditions. In the latter, differences arise due to the different instantaneous luminosity profiles of the two years as shown in Figure 3.3. In fact, the difference observed here in  $\langle\mu\rangle$  matches the difference seen by



the pile-up condition plot made live while the LHC was fully operational as shown in Figure 3.4. Differences seen in the NPV plots can be explained using the same reasoning. For the plots with the number of jets with  $p_T$  greater than 60 GeV, the majority of events have two jets and it is interesting to note that some events contain as many as 13 jets.

### 7.3.2 Cleaning Variables

The cleaning variables are used to quantify the quality of the jets used in the analysis. Out of the many variables, the following four are shown in Figure 7.2 and 7.3: the LAr quality fraction ( $f_Q^{\text{LAr}}$ ), the HEC quality fraction ( $f_Q^{\text{HEC}}$ ), the fraction of jet energy deposited in the EM calorimeters ( $f_{\text{EM}}$ ) and the fraction of energy deposited in the HEC calorimeters ( $f_{\text{HEC}}$ ). These plots include all the jets in the events. In general, the data-MC comparison plots do not show good agreement for these variables. This is because it is extremely challenging for the simulation to account for all the detector and LHC run conditions (like electronic noise and pile-up). These differences have no impact on the analysis presented in this thesis.

Variables associated to the quality of the calorimeter cell signals ( $f_Q^{\text{LAr}}$  and  $f_Q^{\text{HEC}}$ ) show the largest discrepancies as seen by the plots in the left column of Figure 7.2. The agreement between the data-data plots is much better. In all the plots, the majority of the jets have a LAr and HEC quality factor of 0. These corresponds mostly to the leading and subleading jets in each event, where the energy of the jets is produced from good calorimeter cell signals.

Figure 7.3 shows the  $f_{\text{EM}}$  and  $f_{\text{HEC}}$  for all jets. Most jets deposit around 75% of their energy in the EM calorimeters and there is a substantial population of jets that deposit no energy in the HEC calorimeters. Once again the data-data plots in the right column show much better agreement as compared to the data-MC plots in the left column.

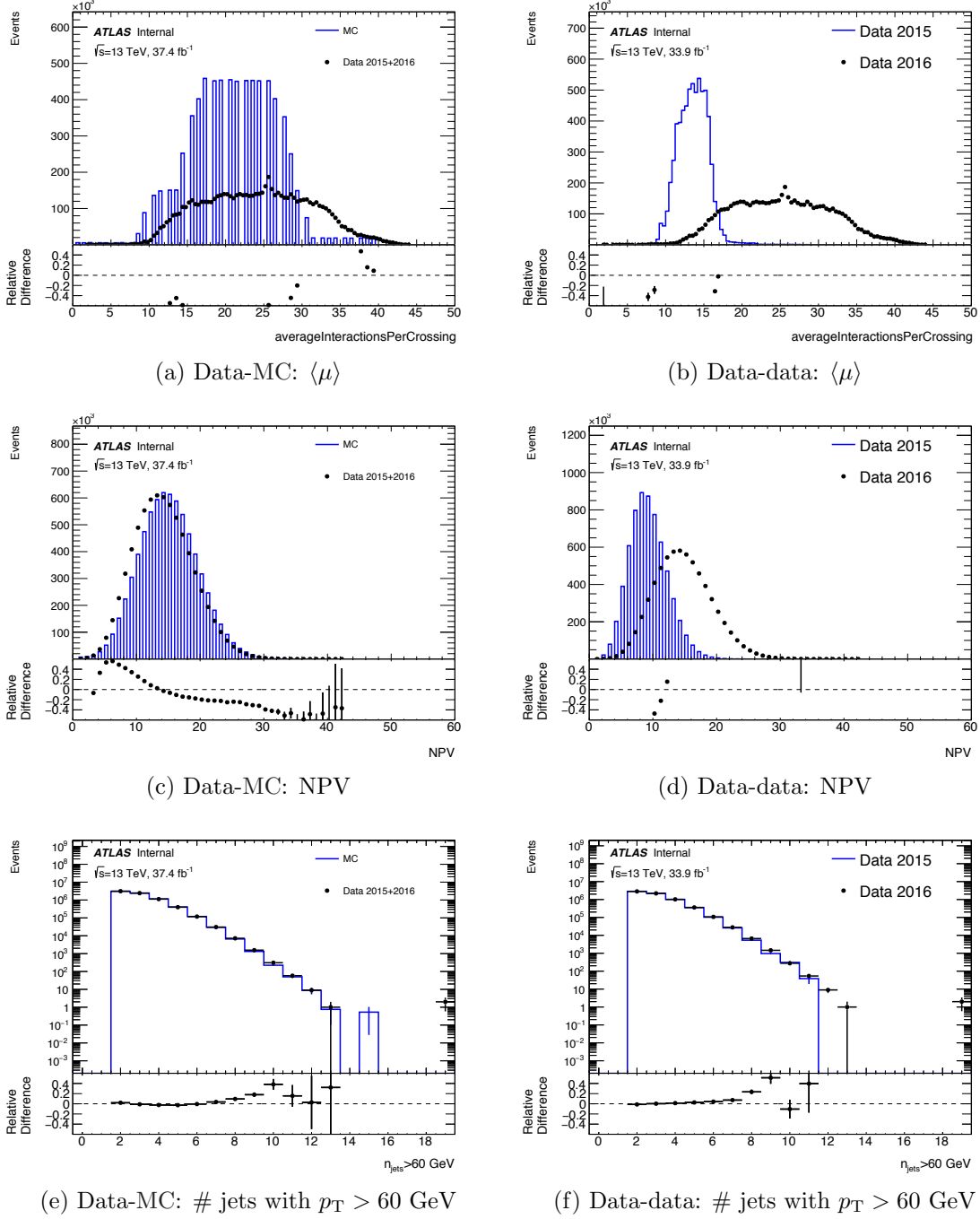


Figure 7.1: Event variables  $\langle\mu\rangle$ , NPV, and the number of jet for the data-MC and data-data comparison are shown in the left and right column respectively.  $\langle\mu\rangle$  represents the average interactions per bunch crossing and NPV shows the number of primary vertices in each event. The differences in these distributions are due to the differences in the pile-up conditions. The number of jets are shown with  $p_T$  greater than 60 GeV.

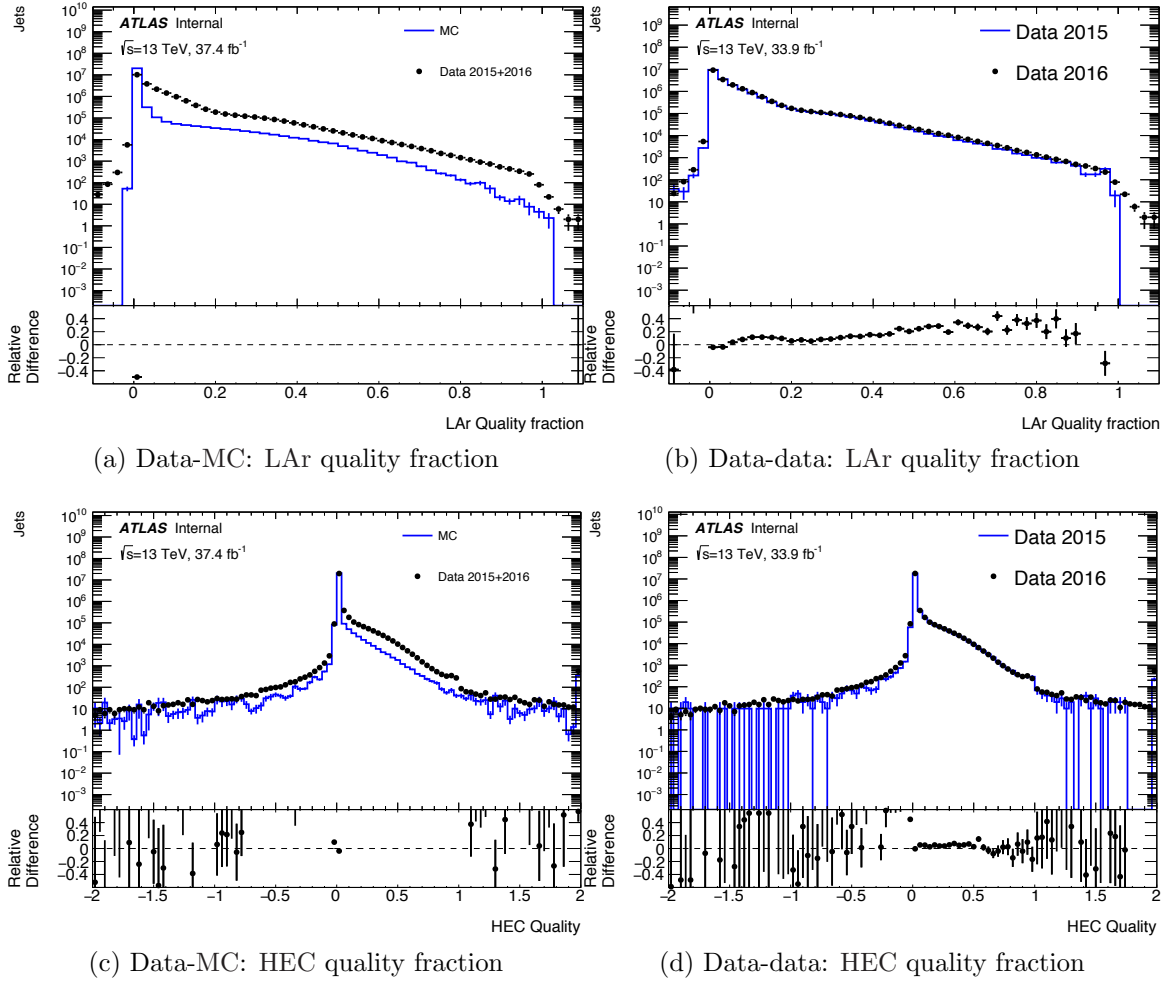


Figure 7.2: LAr and HEC quality fraction variables for the data-MC and data-data comparison are shown in the left and right column respectively. The variables show the fraction of the jet energy emerging from poor quality LAr or HEC calorimeter cells. The differences in the data-MC figures are due to the inability of the simulation to account for all the detector and LHC run conditions (like electronic noise and pile-up).

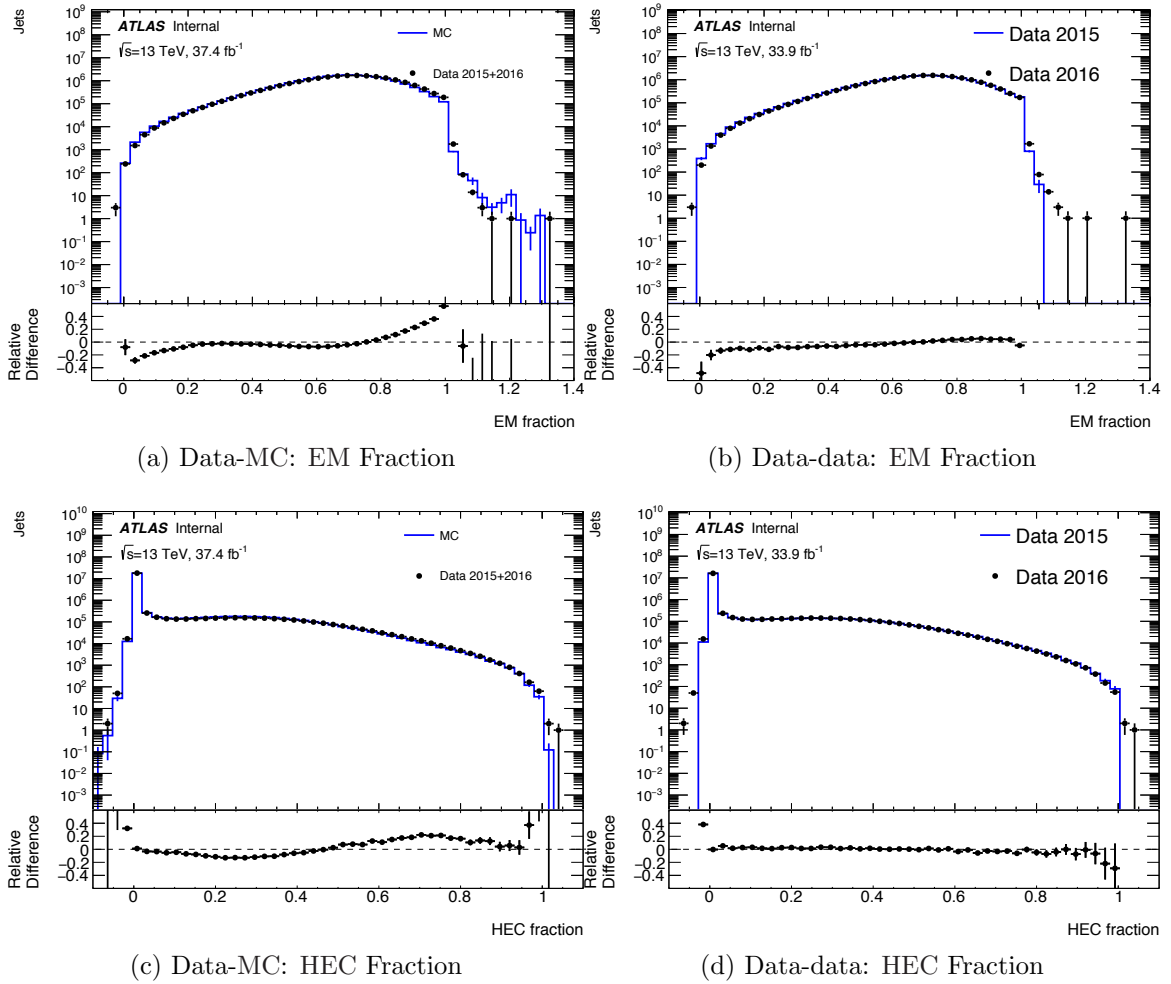


Figure 7.3: The fraction of energy deposited in the EM and HEC calorimeters are shown for the data-MC and data-data comparisons in the left and right column respectively. The differences in the data-MC figures are due to the inability of the simulation to account for all the detector and LHC run conditions (like electronic noise and pile-up).

### 7.3.3 Jet Variables

The next set of variables studied are the jet kinematic variables. As the dijet mass is produced by combining the leading and subleading jets, the third and higher jets are not shown here. Figure 7.4 shows the transverse momentum of the leading (first row of the figure) and subleading (second row of the figure) jets. Here, the data-MC and data-data plots show reasonable agreement. The leading and subleading jet  $p_T$  cuts of 440 GeV and 60 GeV are visible.

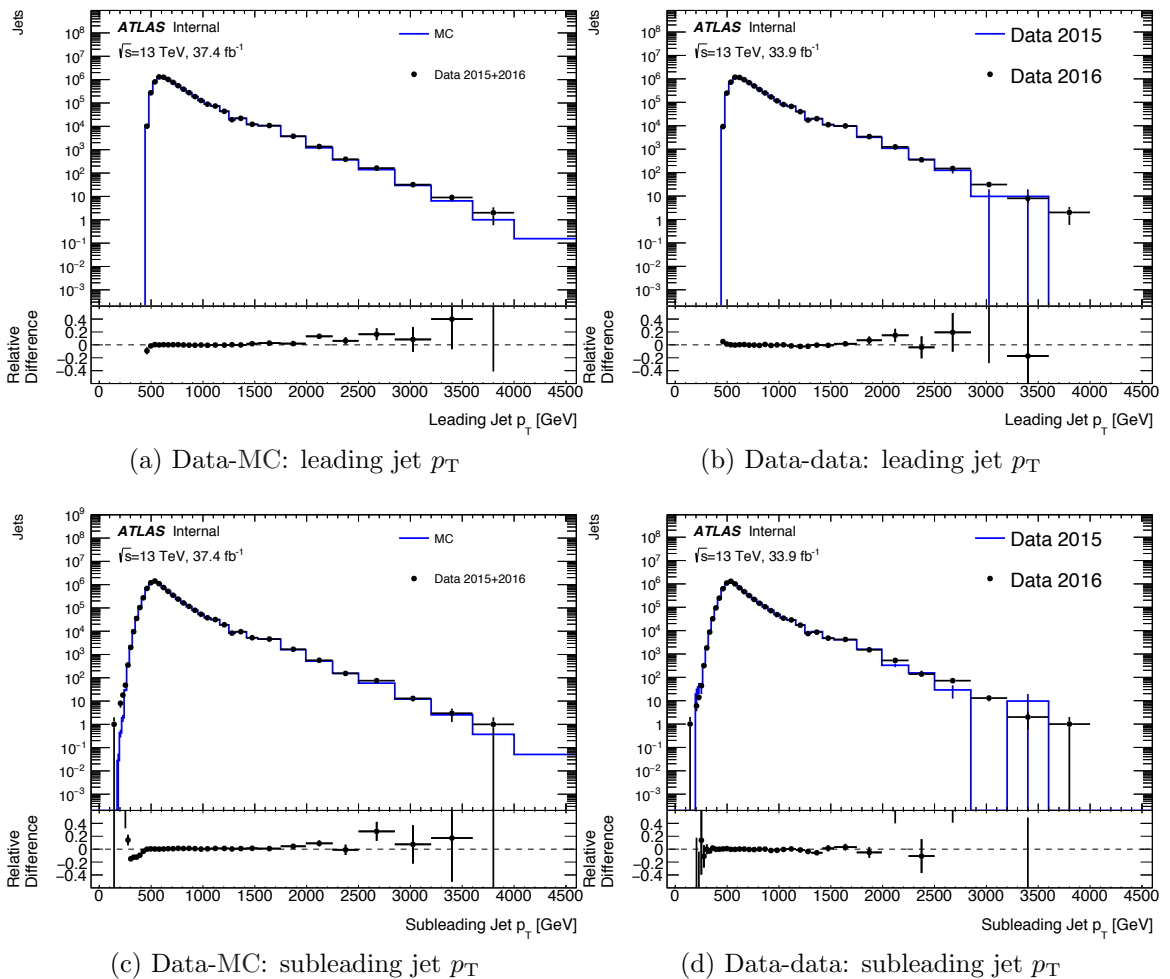


Figure 7.4: The leading and subleading jet transverse momentum are shown in (a), (b) and (c), (d) respectively. The left column shows the data-MC comparison and the right column shows the data-data comparison.

Figure 7.5 shows the energy of the leading and subleading jets. The energy of

the subleading jet for the data-MC comparison (c) shows the largest discrepancy. This is because the additional jets produced during the parton showering stage of the MC simulation can be rather energetic. This can cause them to be tagged as the subleading jet in the event instead of the true subleading jet from the hard-scattering interaction, and this tends to distort the energy spectrum. The fact that this discrepancy is visible in the total energy of the subleading jet and not the  $p_T$  means that these additional jets contain large longitudinal momenta.

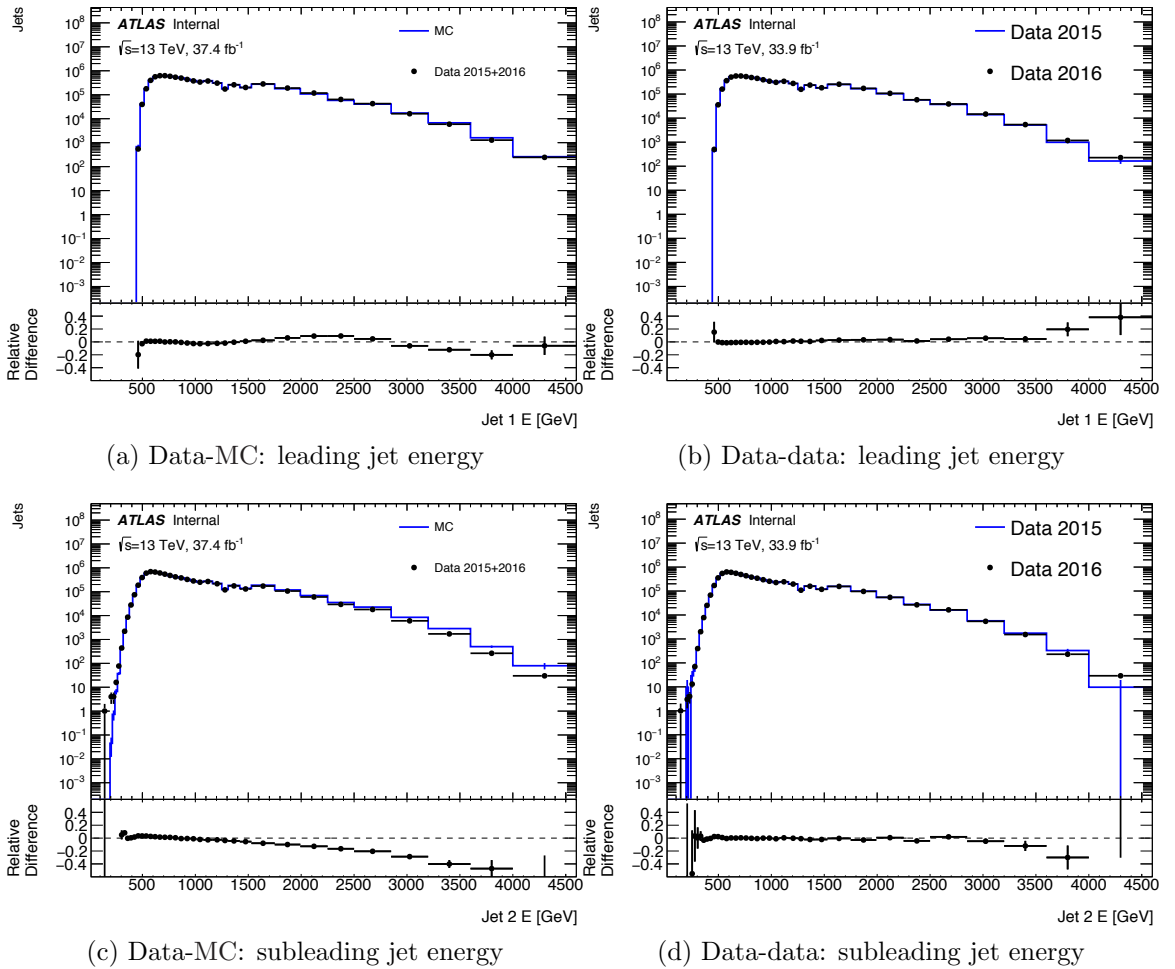


Figure 7.5: The leading and subleading jet energy are shown in (a), (b) and (c), (d) respectively. The left column shows the data-MC comparison and the right column shows the data-data comparison.

The pseudorapidity of the leading and subleading jets are shown in Figure 7.6.

There is good agreement in all plots except in the data-MC comparison of the sub-leading jet  $\eta$  (c). This occurs for the same reason as the difference in the sub-leading jet energy. The discrepancy in the  $\eta$  suggests that these additional jets are picked up from the forward regions, i.e. with high  $\eta$  closer to the beam pipe.

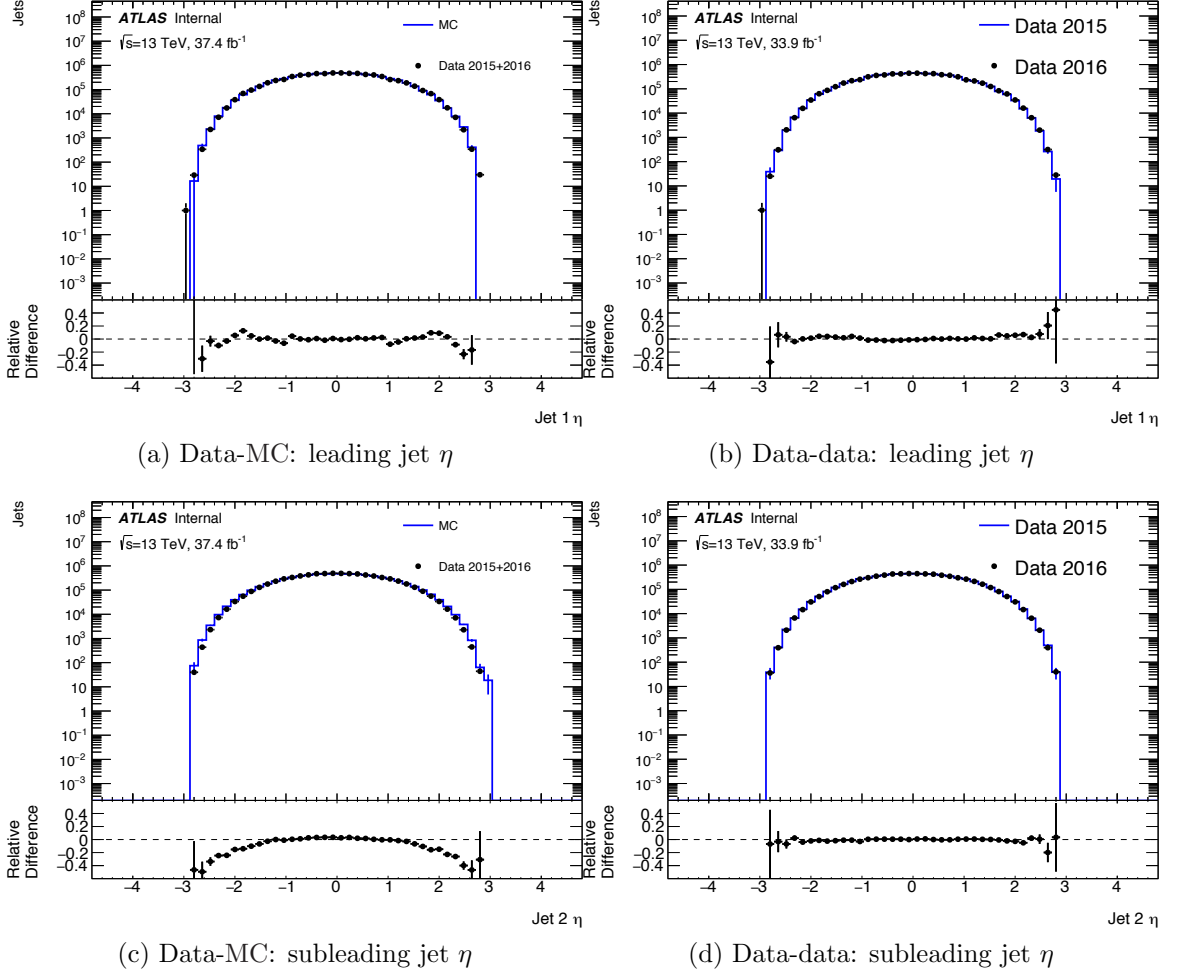


Figure 7.6: The leading and sub-leading jet pseudorapidity is shown in (a), (b) and (c), (d) respectively. The left column shows the data-MC comparison and the right column shows the data-data comparison.

Figure 7.7 shows the azimuthal angle  $\phi$  of the leading and sub-leading jets. The distributions are flat as a function of  $\phi$  and this is expected as jets have no azimuthal angle preference. The dips observed in the data distributions are caused by dead or corrupted calorimeter modules (specifically Tile modules). In the 2015 data, the

dead modules were located at a  $\phi$  of approximately 1 and 2. In the 2016 data, dead modules are found at approximately 0.5 and  $-1.2$ . These modules can also be seen in the  $\eta - \phi$  correlation plots shown in the next section.

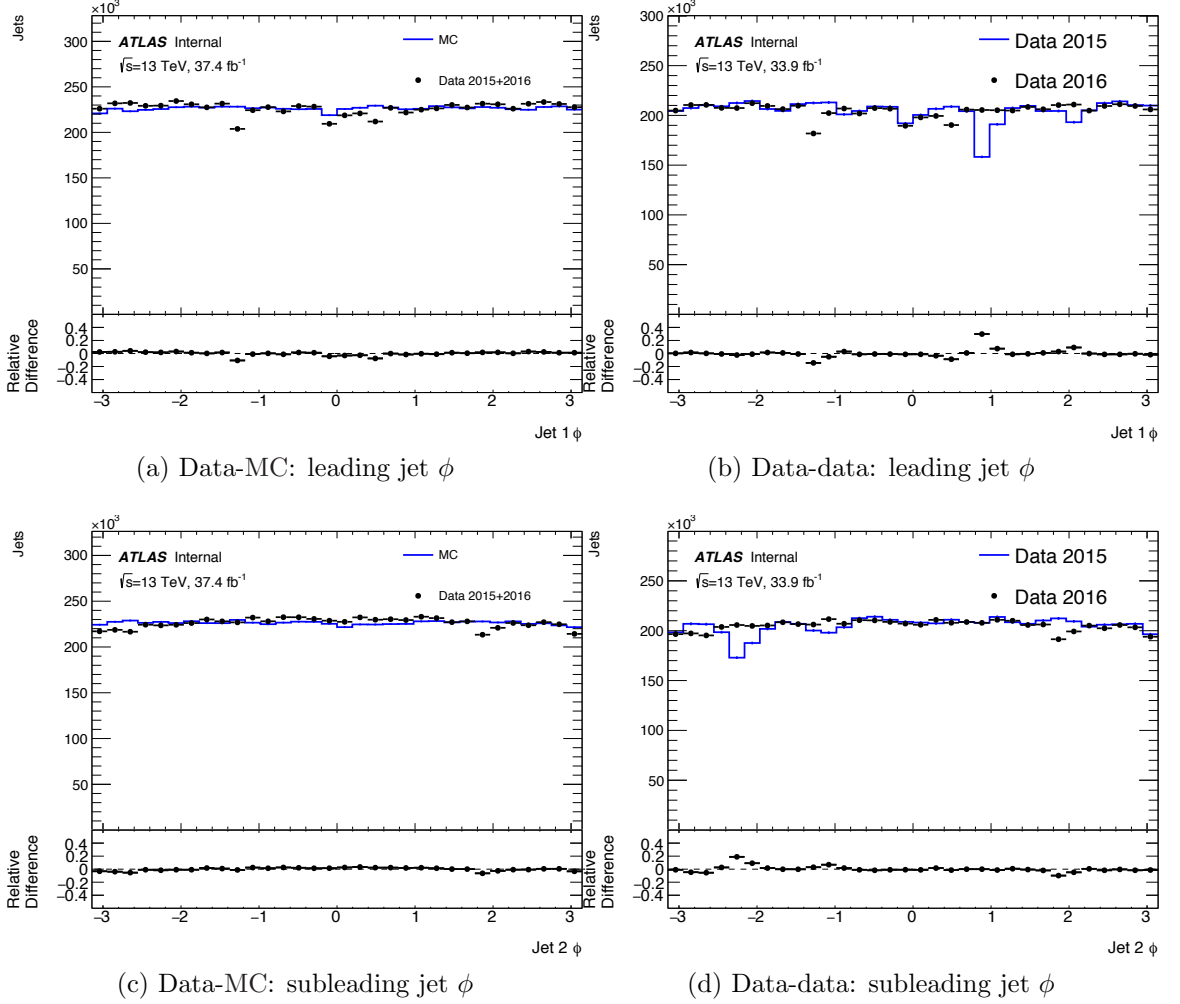


Figure 7.7: The leading and subleading jet azimuthal angles are shown in (a), (b) and (c), (d) respectively. The left column shows the data-MC comparison and the right column shows the data-data comparison. The dips in the figures are due to dead calorimeter modules.

Since the jets of the dijet system are produced back-to-back in  $\phi$ , if one of those jets falls into the dead cell region, the whole event is lost, effectively producing a dip  $\pi$  radians apart in the  $\phi$  distribution of the other jet. This explains why there are dips  $\pi$  radians apart in the leading and subleading jet  $\phi$  distributions.



### 7.3.4 Correlations

Correlations between various kinematic variables were also studied. Here, only the correlations between the transverse momentum, energy and azimuthal angle as a function of the pseudorapidity are shown. Figure 7.8 shows these as two-dimensional plots with the  $p_T$ ,  $E$  and  $\phi$  shown on the y-axis and  $\eta$  on the x-axis.

The colors on the plots show the number of jets with blue being the lowest and red being the highest number. The three plots in the left column show correlations in the full dataset and the right column shows the corresponding plots for the MC. The black, round circles on each plot show the average of all the points sharing the same x value. The shapes and trends visible in these plots are a result of the kinematic cuts of the analysis. The data  $\eta-\phi$  plot (e) shows the exact location of the dead/corrupted tile modules in the 2016 data (these were seen in the leading and subleading jet  $\phi$  plots in the previous subsection):  $\phi = 1.23$ ,  $0 < \eta < 0.85$  and  $\phi = 0.44$ ,  $-0.85 < \eta < 0$ . The faulty modules of the 2015 data are not visible here and they were disabled for 2016.

### 7.3.5 Dijet Variables

The final and the most important set of variables studied are the dijet variables. The variables presented for each event here are  $y^*$ ,  $y_B$ ,  $\Delta R$ ,  $p_T^{jj}$  and  $m_{jj}$ .

Figure 7.9 shows the two angular variables  $y^*$  (see Equation 5.7) and  $y_B$  (see Equation 5.8). The  $|y^*| < 0.6$  analysis cut is visible here. Figure 7.10 shows the distance  $\Delta R$  (see Equation 3.5) between the two jets in the  $\eta-\phi$  plane and the transverse momentum of the dijet system. In the majority of events, the two jets are centrally produced and back-to-back in  $\phi$ , i.e.  $\Delta\phi$  is  $\pi$  radians and  $\Delta\eta$  is zero. This gives the majority of jets a  $\Delta R$  value of  $\pi$  radians and this is seen in the  $\Delta R$  plots. The transverse momentum of the dijet system has a smoothly falling distribution peaked at approximately 50 GeV and extending to about 2 TeV.

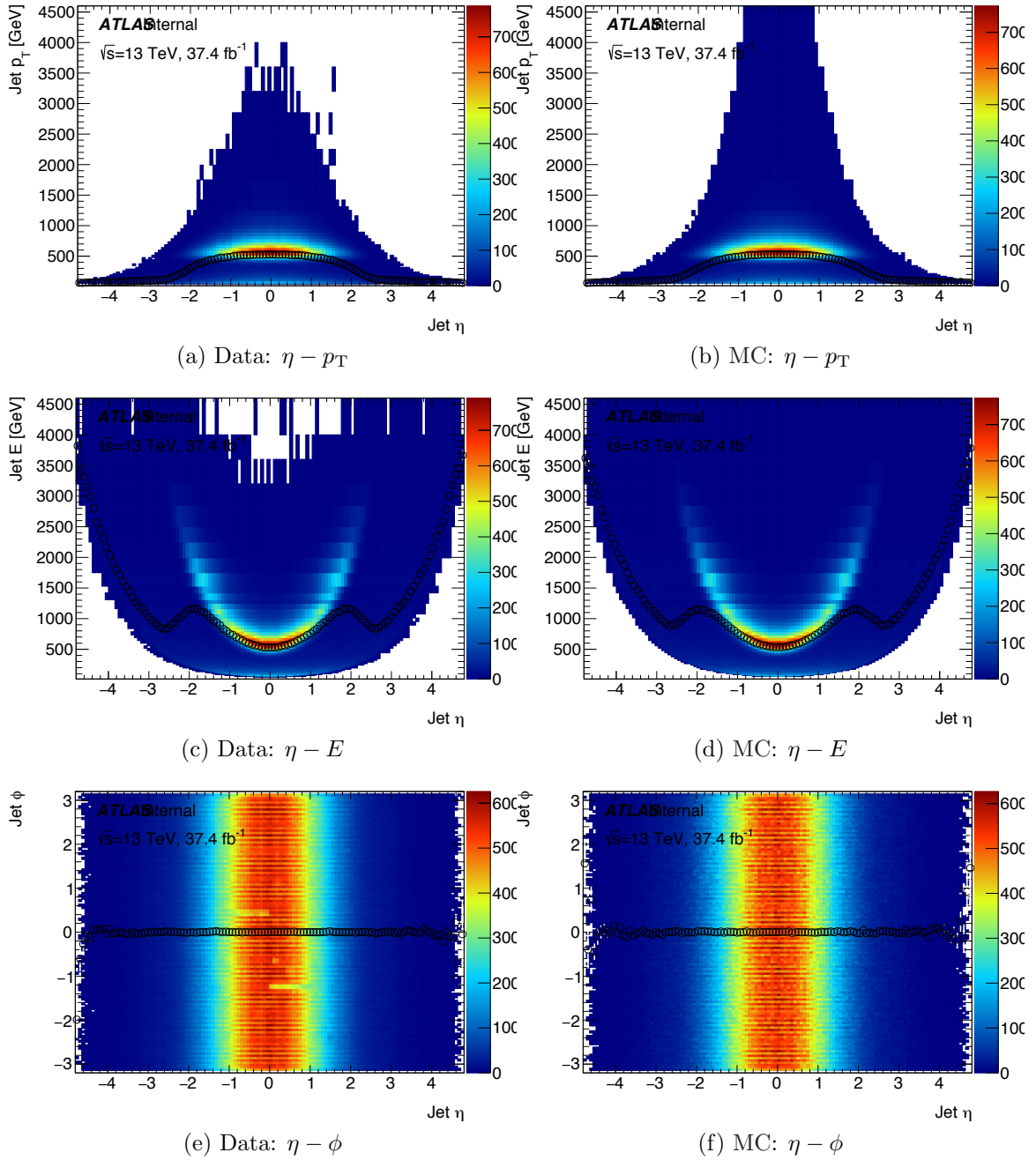


Figure 7.8: The correlations between various kinematic variables for data and MC are shown here:  $\eta$  vs.  $p_T$  (a, b),  $\eta$  vs.  $E$  (c, d) and  $\eta$  vs.  $\phi$  (e, f). The colors show the number of jets (blue being the lowest and red being the highest). The black, round circles show the average of all the points sharing the same x value. The shapes and trends visible in these plots are a result of the kinematic cuts of the analysis.

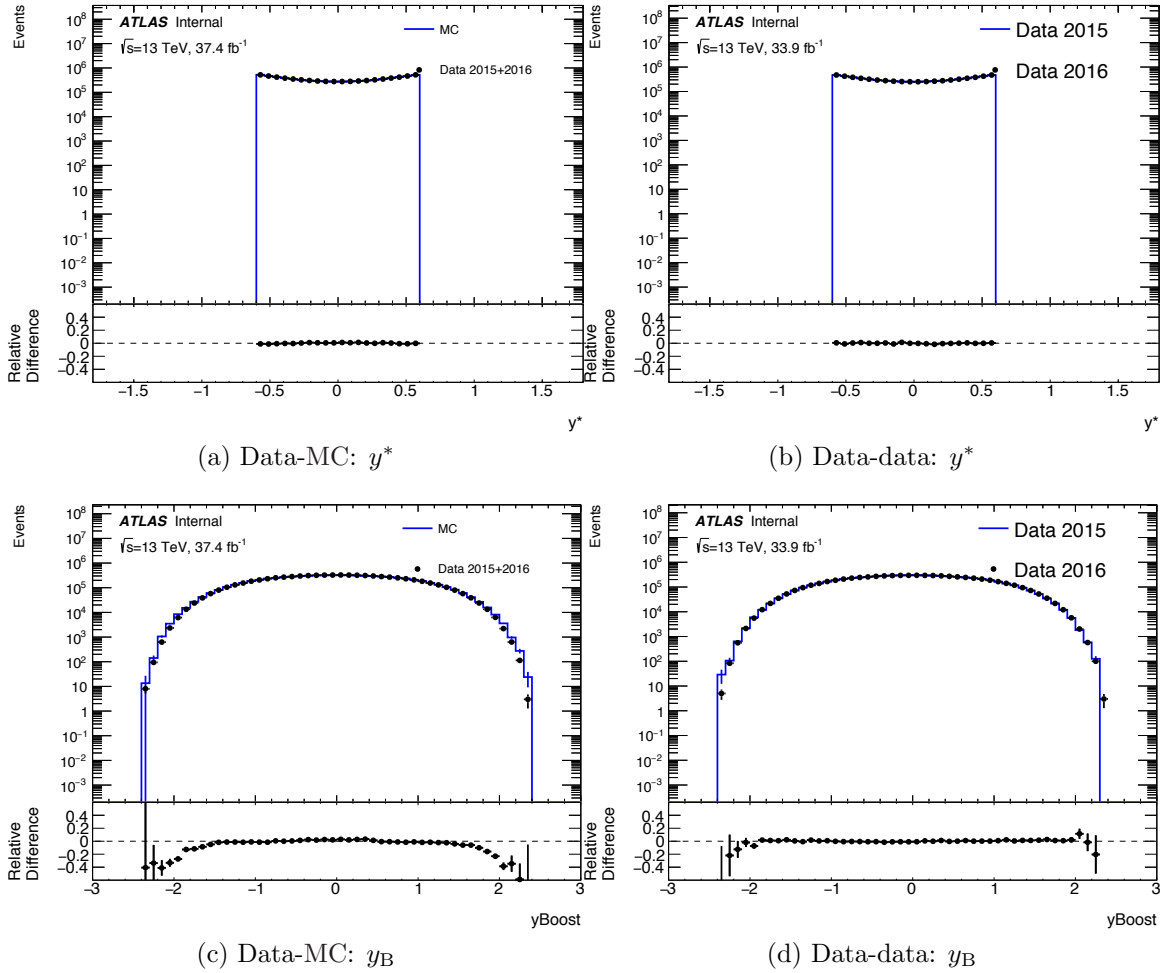


Figure 7.9: The  $y^*$  distributions for the data-MC and data-data comparison are shown in (a) and (b). The  $y_B$  distributions can be seen in (c) and (d).

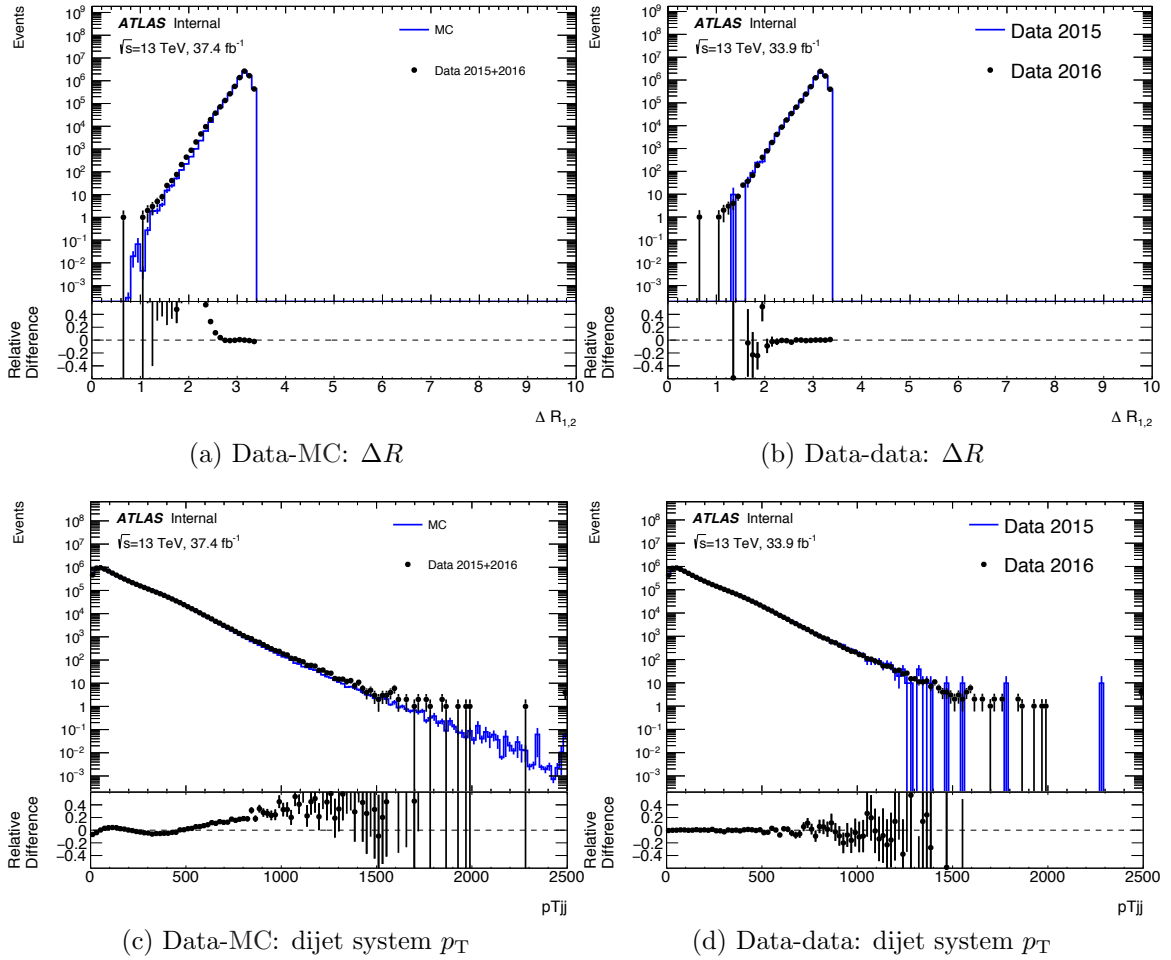
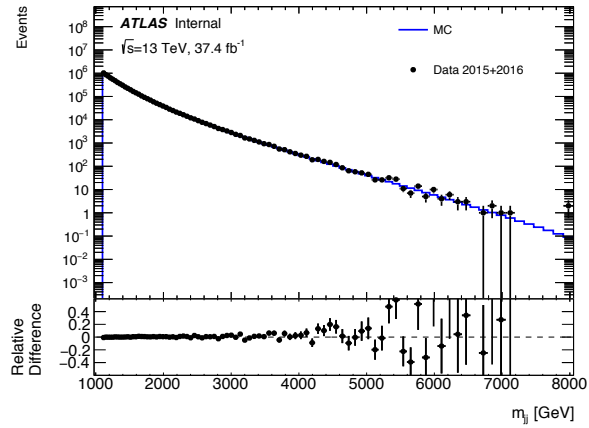
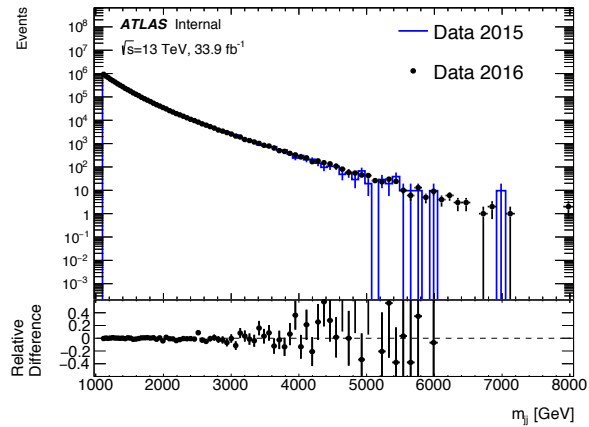


Figure 7.10: The  $\Delta R$  distributions for the data-MC and data-data comparison are shown in (a) and (b). The dijet system  $p_T$  distributions (in GeV) can be seen in (c) and (d).

The final variable shown is the dijet mass distribution in Figure 7.11. Both the data-MC and data-data distributions show good agreement. The binning of the  $m_{jj}$  distribution is chosen to be proportional to the dijet resolution ( $2 - 3\%$ ) as shown in Figure 7.12.



(a) Data-MC:  $m_{jj}$



(b) Data-data:  $m_{jj}$

Figure 7.11: The dijet mass distributions for the data-MC (a) and data-data (b) comparisons.

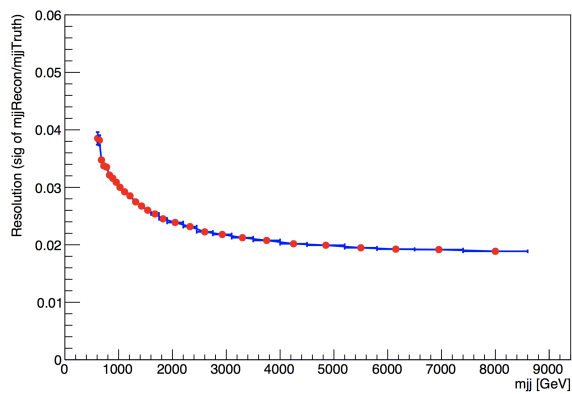


Figure 7.12: The dijet mass resolution as a function of mass. It is determined by the RMS of the difference between the truth jet matched to a reconstructed jet.

## CHAPTER 8

# Search for New Phenomena in Dijets

This chapter is the culmination of this thesis. It presents the resonance search results on the dijet data using two methods. First the model-independent `BUMPHUNTER` search results are presented using the `SWIFT` background. Then the general (using Gaussian signals) and model-dependent (excited quark and heavy gauge boson signals) `SWIFT` search results are displayed. Finally, 95% CL upper limits are calculated for the signal models.

## 8.1 BumpHunter Search

New particles are expected to appear as localized excesses in the dijet mass distribution. Regardless of the shape of the new signal, the localized excess will result in the upward fluctuation of several adjacent  $m_{jj}$  bins. Such an excess can be found by comparing the data mass distribution to a background model without assuming a particular signal shape. One method that does so is the `BUMPHUNTER` [102].

### 8.1.1 The BumpHunter

`BUMPHUNTER` is a tool to compare the data and background histograms and identify the region of the largest discrepancy. It works by sequentially combining adjacent bins of the data and background histograms - starting from two consecutive bins and

finishing with half of the histogram. For each combination of bins, it calculates the probability of the data ( $x$ ) given the background ( $\lambda$ ) using the Poisson distribution:

$$P(x|\lambda) = e^{-\lambda} \frac{\lambda^x}{x!}. \quad (8.1)$$

This is known as the BUMPHUNTER Poisson probability. For bin combinations with  $x < \lambda$ , the Poisson probability is set equal to 1. The combination of bins with the smallest Poisson probability is then identified on the data histogram.

To take into account the look-elsewhere effect, BUMPHUNTER calculates a global p-value by repeating the search procedure over a large number of PE ( $\sim 10,000$ ) drawn from the SWIFT background. From each PE, the most significant Poisson probability  $p_{\min}$  is used to create a test statistic  $t$ :

$$t = -\log(p_{\min}). \quad (8.2)$$

The global p-value is then computed by counting the fraction of PEs that have  $t$  larger than the  $t$  observed in the data.

If BUMPHUNTER finds a deviation in the data with a global p-value less than 0.01, the deviation is called “interesting”. The bins that correspond to the “interesting” excess are masked and a new background estimation is produced. This removes any bias present in the background model due to the presence of a signal. The BUMPHUNTER search procedure is repeated again comparing the data with the bias-free background model.

This procedure has been validated numerous times and has been extensively used in past dijet resonance searches [91, 93, 96, 113, 114].



### 8.1.2 Search Results

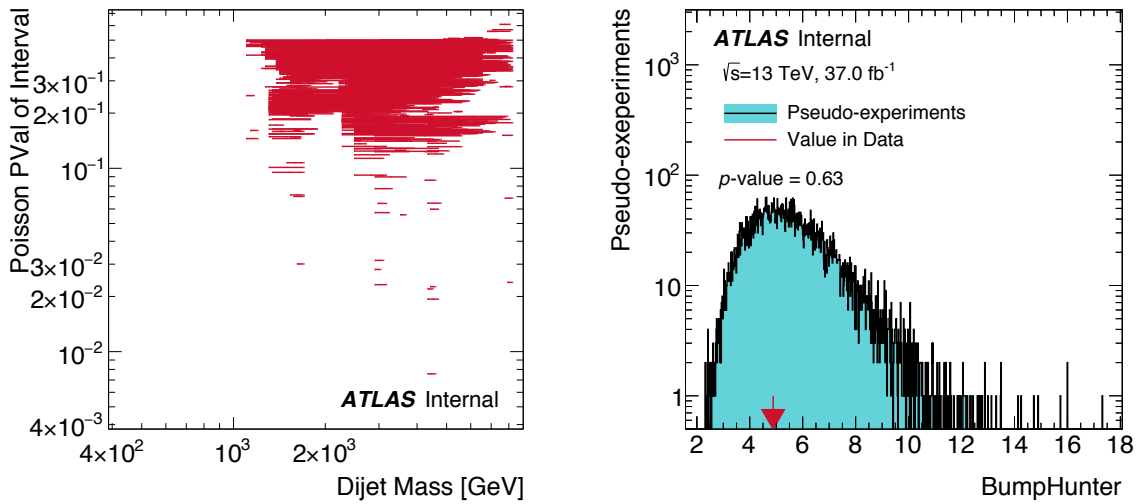
The BUMP HUNTER search results with the SWIFT background are shown in Figure 8.1.

Figure 8.1 (a) shows an overlay of the local p-values for each bin combination. The most significant deviation is seen in the combination of 3 bins centered at 4.5 TeV (with a probability of 0.008). Figure 8.1 (b) shows a histogram of the BUMP HUNTER test statistic from each PE. The red arrow signifies the value of the test statistic in the data and its global p-value of 0.63 is also shown in the figure. This value means that 63% of the times, the background fluctuations can produce an excess as significant as the one seen in the data at approximately 4.5 TeV. Hence, the fluctuation is not significant at all. Figure 8.1 (c) shows the data mass distribution (black dots), the background model (red histogram) and the most significant region (vertical blue lines). Examples of two hypothetical signals are shown in the open circle (4 TeV  $q^*$ ) and square (5 TeV  $q^*$ ) green circles. The second panel of the figure shows the significance of the deviations in the data with respect to the background. The last panel shows the relative difference between in the data and the MC dijet mass estimation. The blue bands are the JES uncertainty bands. This comparison with MC is for display purposes only.

The search result show no signs of a significant excess.

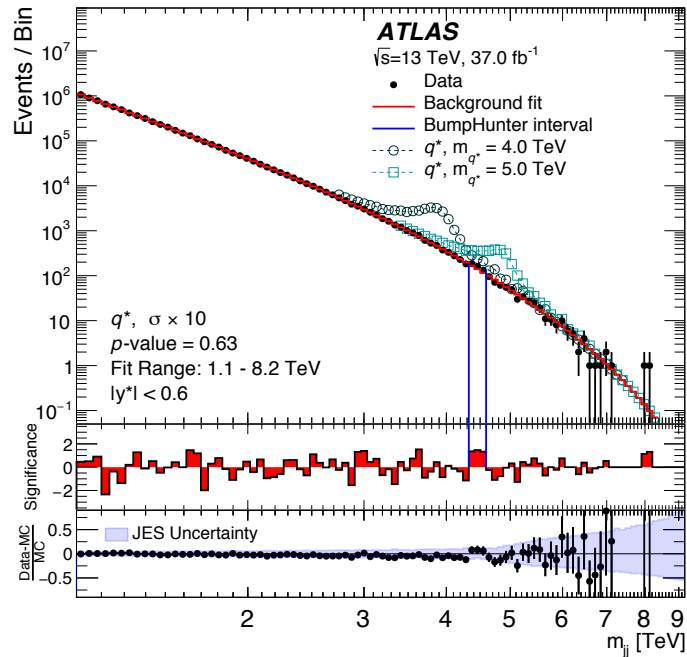
## 8.2 Signal Shapes for the Model-Dependent Searches

For the model-dependent searches discussed in the next section, signal shapes for excited quarks and heavy gauge bosons are required. These shapes are obtained from MC simulation for certain masses. Shapes for intermediate masses are obtained from the signal morphing procedure described in Appendix B. Figure 8.5 shows an overlay of the excited quark and heavy gauge boson signal shapes obtained from the



(a) Poisson probabilities

(b) Global p-value



(c) BUMPHUNTER Search Result

Figure 8.1: (a) The Poisson probabilities for each bin combination is shown. The most significant deviation is in 3 bins centered at 4.5 TeV (with a probability of 0.008). (b) The global p-value (0.63) of the most significant deviation in the data (red arrow) and the test statistic from each PE (blue distribution) are shown. (c) The BUMPHUNTER search result. The blue vertical lines show the most significant region in the data.

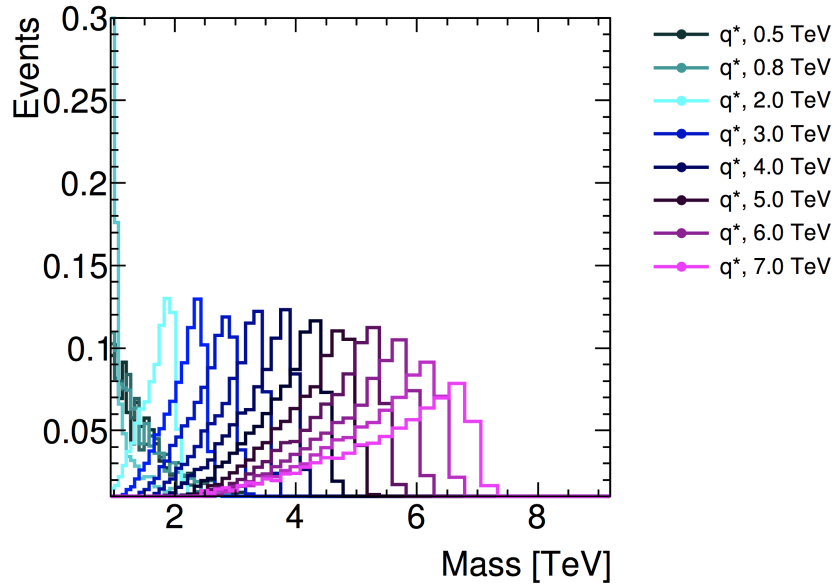
morphing procedure for four masses (along with four Gaussian signal shapes with various widths).

### 8.2.1 Excited quarks - $q^*$

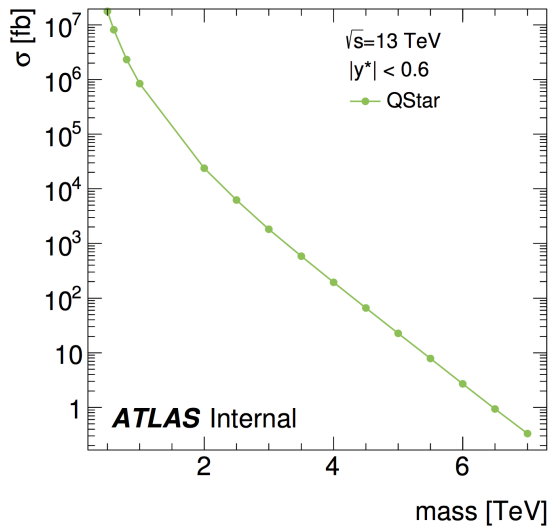
The  $q^*$  signal shapes ( $qg$  initiated) are simulated with the PYTHIA [69] event generator using the A14 event tune [110] and the NNPDF2.3 PDF set [109]. Both light flavor ( $u, d, s$ ) and heavy flavor ( $c, b$ ) quarks are considered with spin 1/2 and quark-like SM couplings. The compositeness scale is set equal to the quark mass. The signal simulation is processed with the full detector simulation, using GEANT4. Like the data, it is subject to the full jet reconstruction process (Chapter 4) and the full analysis selection procedure (Chapter 7). Figure 8.2 shows the  $q^*$  signal shape, cross-section and acceptance as a function of the simulated signal masses. The signal shapes below 2 TeV are distorted due to the  $m_{jj}$  analysis cut requiring the dijet mass to be greater than 1.1 TeV. The broad width of the signals (especially at higher masses) is due to final-state radiation, which is significant because the final-state gluon has large color charge. The acceptance represents the fraction of signal events passing the analysis selection. It is low for signals of mass less than 1 TeV due to the  $m_{jj}$  mass cut of 1.1 TeV.

### 8.2.2 Heavy gauge bosons - $W'$

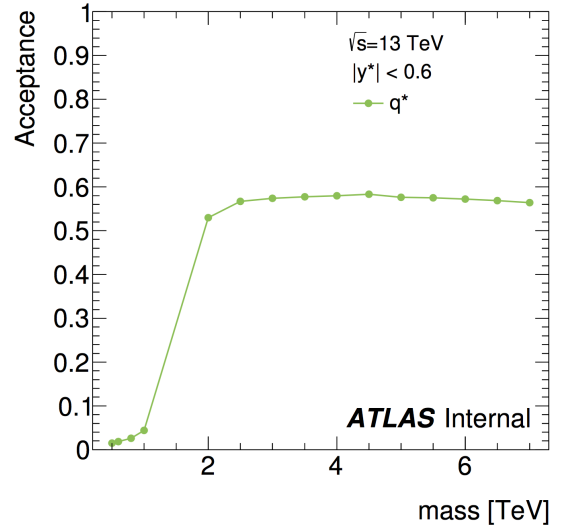
The heavy gauge bosons  $W'$  ( $q\bar{q}$  initiated) considered in this analysis is the  $W'$  and it is assumed to have SM like couplings to SM particles. The  $W'$  signals are also simulated using PYTHIA [69] with the NNPDF2.3 PDF set [109] and the A14 event tune [110]. They are produced from a quark-antiquark interaction and are restricted to decay to two quarks with all six quark flavors included. After passing through the GEANT4 detector simulation, the analysis selection is applied. Figure 8.3 shows the  $W'$  signal shape, cross-section and acceptance as a function of mass. The broad



(a) Signal shapes

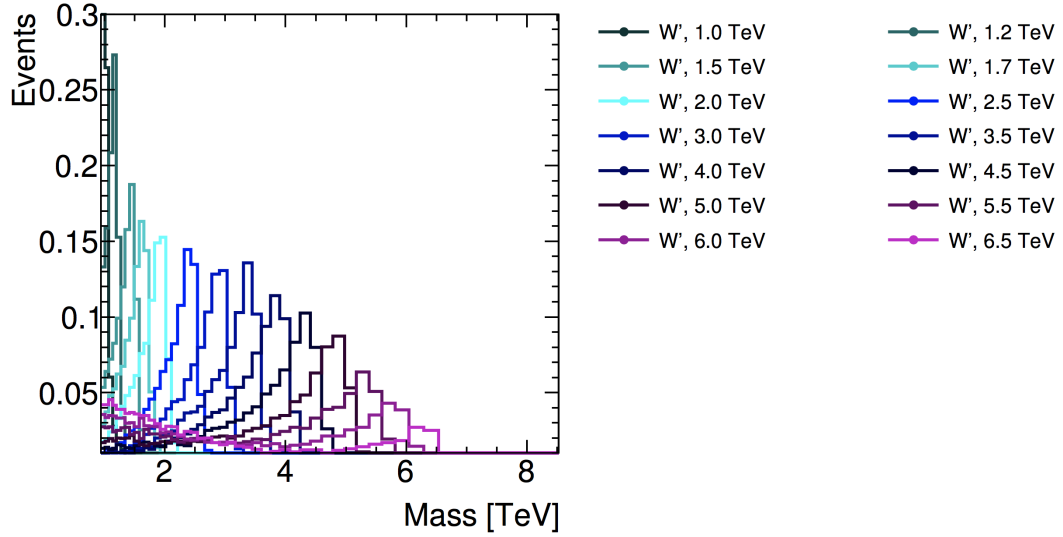


(b) Cross-section

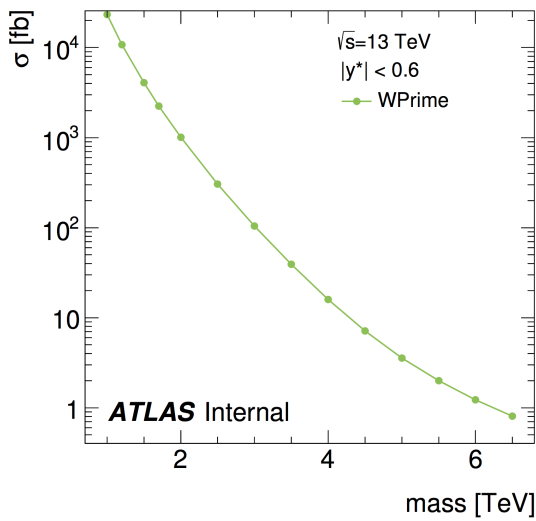


(c) Acceptance

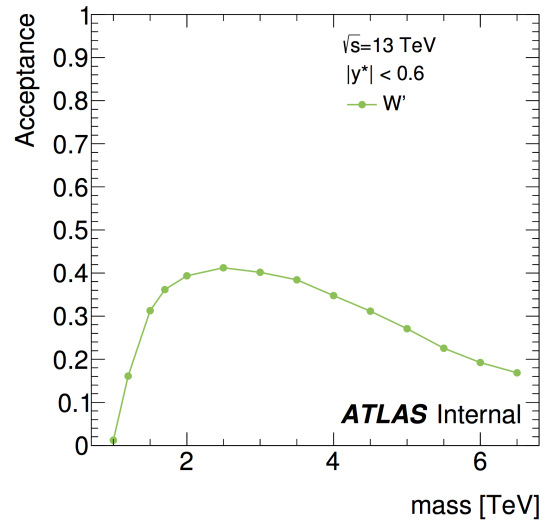
Figure 8.2: (a) Normalized signal shapes from MC simulations, (a) signal cross-section and (c) acceptance as a function of  $q^*$  mass. The signal shapes below 2 TeV are distorted due to the  $m_{jj}$  analysis cut requiring the dijet mass to be greater than 1.1 TeV. The acceptance for signal masses below 2 TeV is also low due to the  $m_{jj}$  mass cut.



(a) Signal shapes



(b) Cross-section



(c) Acceptance

Figure 8.3: (a) Normalized signal shapes from MC simulations, (a) signal cross-section and (c) acceptance as a function of  $W'$  mass. The acceptance for signal masses below 2 TeV is low due to the  $m_{jj}$  mass cut of 1.1 TeV. The drop in the acceptance towards higher masses is due to the increasing low mass tail caused by PDF effects.

width of the signals and the off-shell tail (especially at higher masses) are due to a combination of final-state radiation and PDF effects. The drop in the acceptance towards high masses is due to the increasing low mass tail as can be seen for the highest mass points in the figure. This is caused by the sharply falling PDFs in conjunction with the large width of the signals.

### 8.3 SWiFt Search and Limits

The LLHR-based local p-value SWiFt search results are shown in Figure 8.4. The search for general Gaussian (with detector resolution, 5%, 7%, 10% width),  $q^*$  and  $W'$  signals are shown in green, red and orange colored curves with each point representing the local p-value at each mass. For reference, the signal shapes used at a select few masses are shown in Figure 8.5, where the  $q^*$  and  $W'$  shapes are obtained from signal morphing (see Appendix B). The  $q^*$  shapes ( $qg$  initiated) are slightly wider than the  $W'$  shapes ( $q\bar{q}$  initiated) due to greater final-state radiation.

For each signal shape considered, Table 8.1 shows the lowest local p-value found, along with its global p-value. The fits performed in the search include all of the uncertainties described in Section 6.2.5. The effects of the JES uncertainties on the Gaussian signal shapes are taken from the  $q^*$  signal shapes. The window size chosen around each bin is shown in Figure 8.6 where (a) shows the window size as a percentage of the window center and (b) shows the lower and upper limit of each window (in GeV) about the center. Figure 8.7 shows the background function parameter chosen for each window for each signal hypothesis.

No evidence of new physics was found in the searches and 95% CL upper limits are calculated. Figure 8.8 shows the limits for Gaussian (resolution, 5%, 7% and 10% width),  $q^*$  and  $W'$  signals. The observed limits are shown by the solid black lines and the expected limits are the dotted black lines. The green and yellow bands show

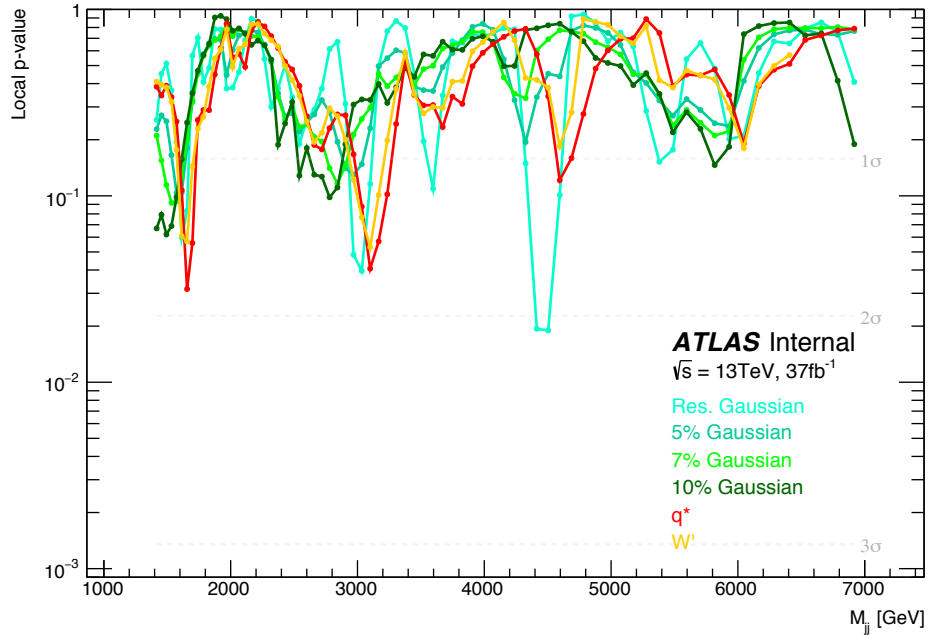


Figure 8.4: Local p-value scan as a function of mass (window center) for four gaussian,  $q^*$  and  $W'$  signal shapes. Depending on the signal shape, each scan identifies a different window for containing the most significant fluctuation in the data.

Signal	Mass [GeV]	Local p-value	Global p-value
Res. Gaussian	4504	0.019	0.659
5% Gaussian	1573	0.104	0.965
7% Gaussian	1533	0.092	0.922
10% Gaussian	1493	0.062	0.839
$q^*$	1653	0.032	0.732
$W'$	3100	0.053	0.856

Table 8.1: Window with the lowest local p-value found from the resonance scans. Global p-values, produced from PEs from the SWiFT background, are also shown. The lowest local p-value (0.019) is seen at a mass of 4504 GeV using the resolution-width Gaussian signal shape.

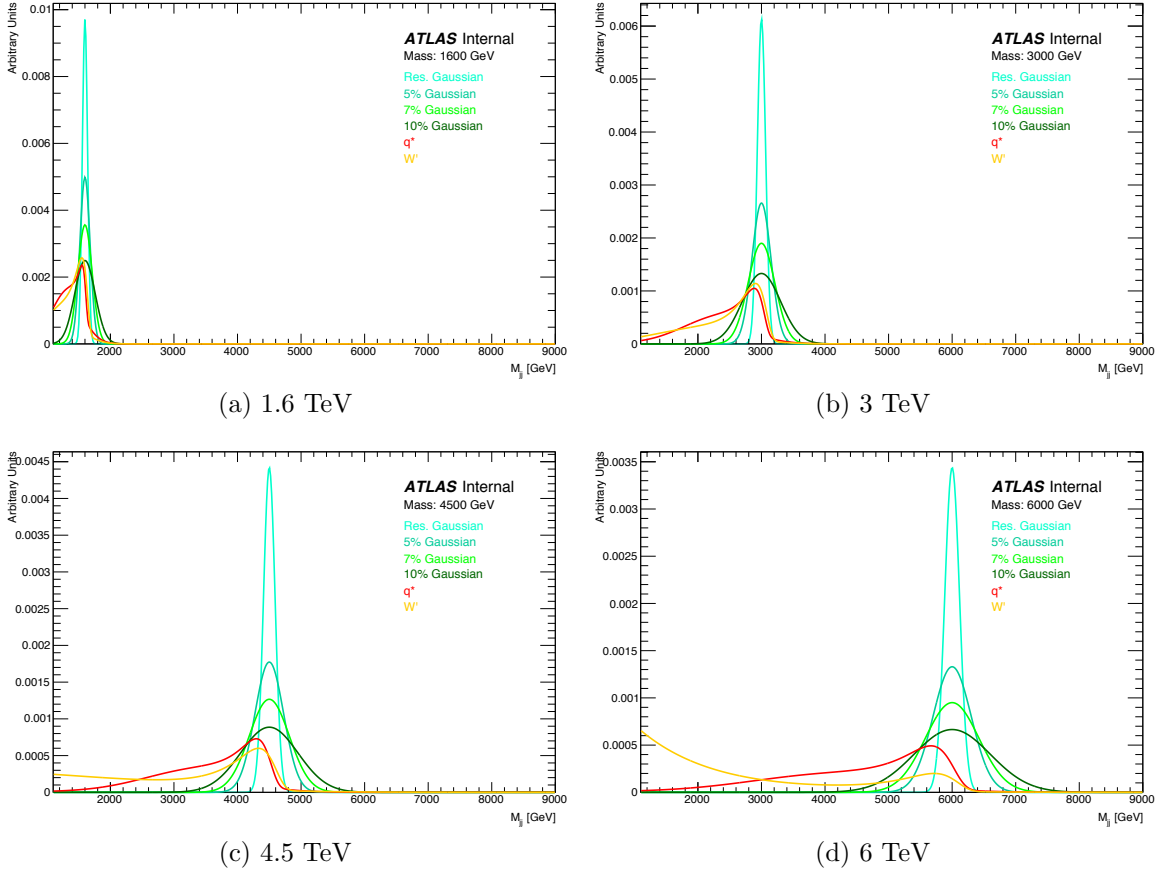


Figure 8.5: Signals shapes used for the six resonance searches. The  $q^*$  and  $W'$  shapes are obtained from signal morphing (see Appendix B) and the Gaussian shapes are simple Gaussian functions with various widths: resolution-width, 5%, 7% and 10%. The  $q^*$  shapes ( $q\bar{q}$  initiated) are slightly wider than the  $W'$  shapes ( $q\bar{q}$  initiated) due to greater final-state radiation.



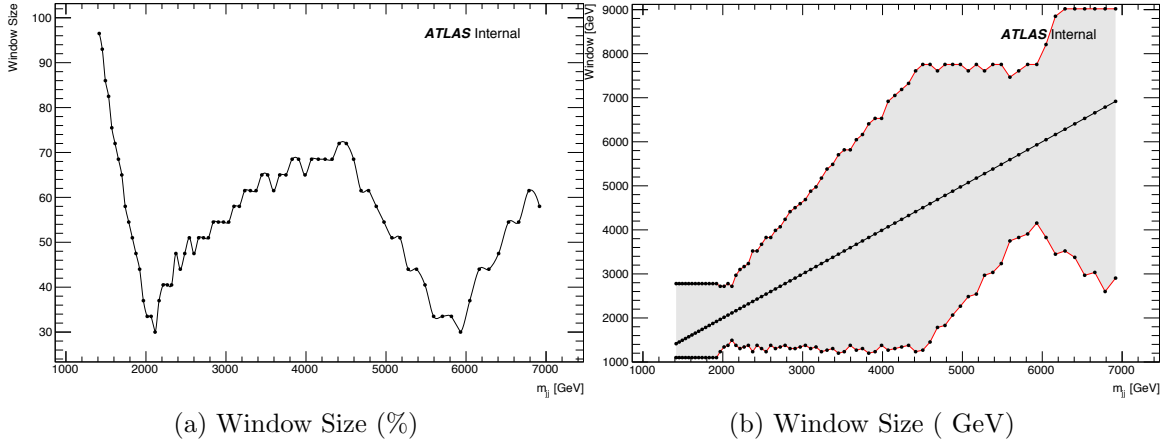


Figure 8.6: The window sizes for each window center (from 1416 to 6918 GeV). The data distribution starts at 1100 GeV. The sizes are picked based on the  $\chi^2$  p-value of the nominal (3-parameter) background-only fit.

the  $1\sigma$  and  $2\sigma$  uncertainties on the expected limit. Except for the  $W'$  signals, limits for all the other signals are calculated for 73 signal mass points, where the masses are equal to the  $m_{jj}$  histogram bin edges. The  $W'$  limits are not calculated past 4.5 TeV because of a loss of signal sensitivity. This occurs due to the rising loss mass tail (caused by PDF effects) which causes the majority of the signal to resemble the shape of the dijet background.

More plots for each resonance search and limits are shown in Appendix A.

## 8.4 Discussion

The sections above showed resonance search results from two different search methods: BUMP HUNTER and SWIFT. Both methods provide complementary results and show no sign of new physics.

BUMP HUNTER identifies the fluctuation at 4.5 TeV as being the most discrepant with respect to the background estimation, with a global p-value of 0.63. BUMP HUNTER works by identifying the collection of adjacent bins with the most significant excess. This approach is straightforward to use, however, it implicitly assumes

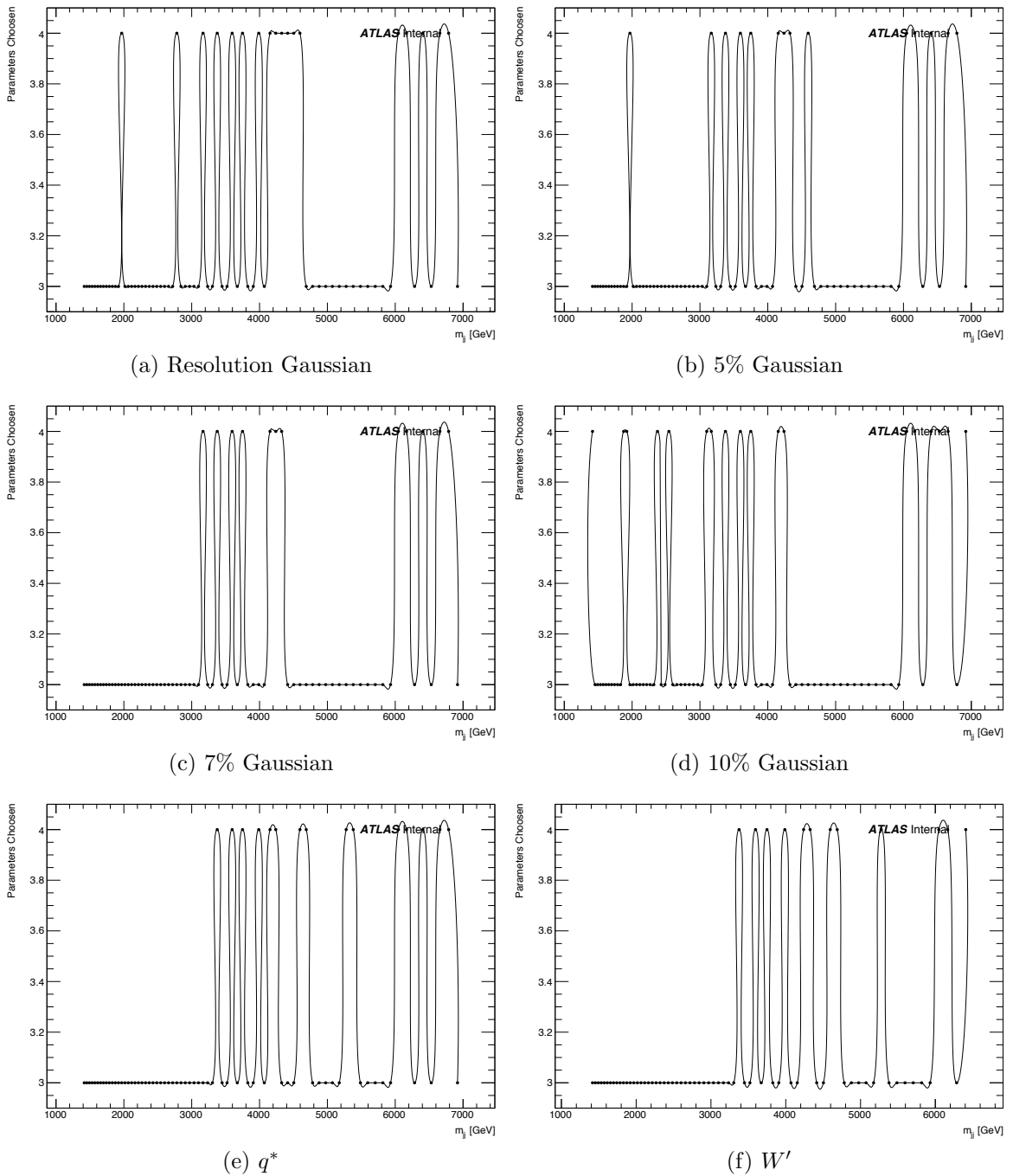
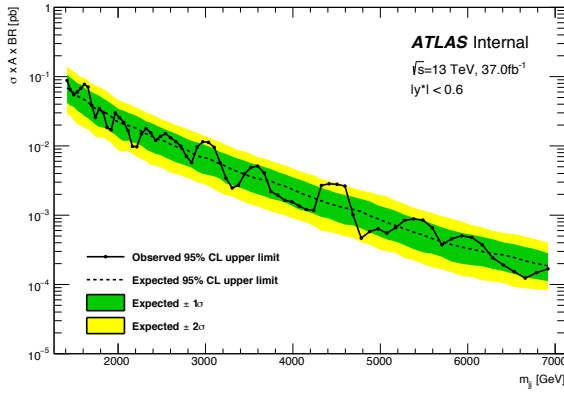
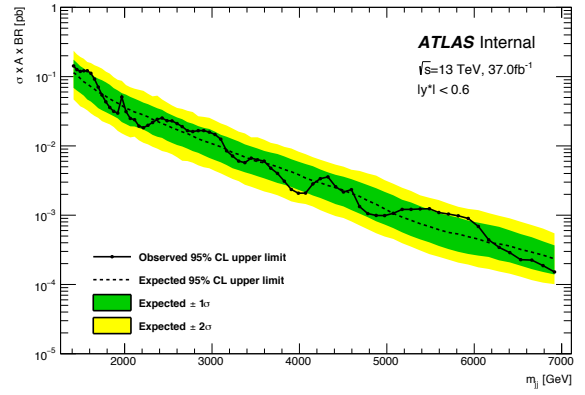


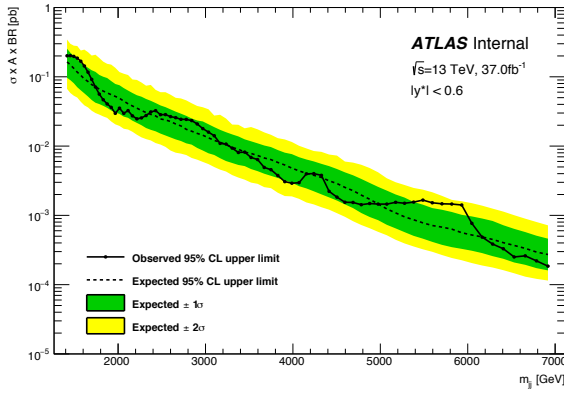
Figure 8.7: The choice of nominal (3-parameter) or alternate (4-parameter) is shown here for each signal shape. It is made based on the  $\chi^2$  p-value of the nominal and alternate signal+background fits.



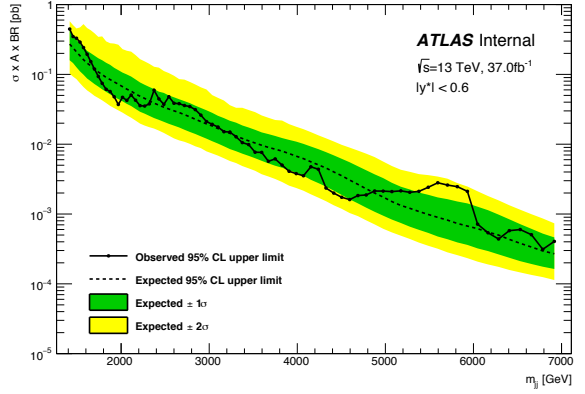
(a) Resolution Gaussian



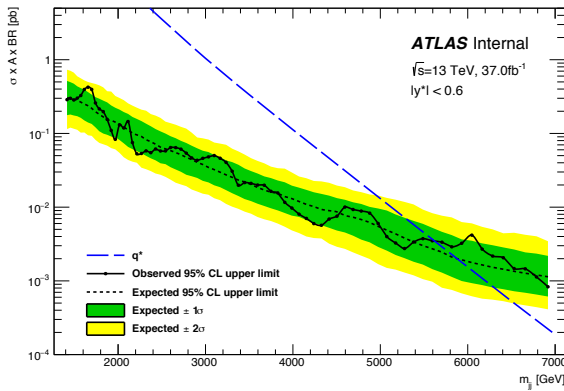
(b) 5% Gaussian



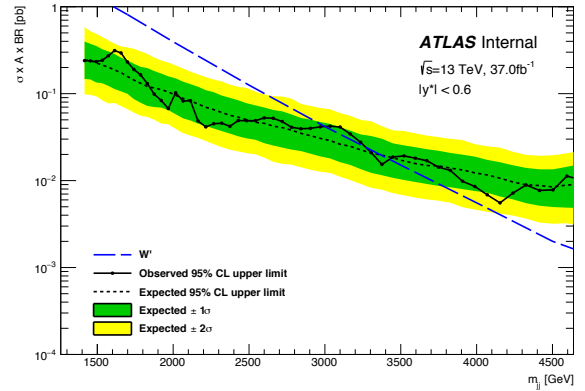
(c) 7% Gaussian



(d) 10% Gaussian



(e)  $q^*$



(f)  $W'$

Figure 8.8: 95% CL limits for gaussian shapes,  $q^*$  and  $W'$  signals using the SWiFT method.

that the signal is uniformly distributed across the bins in question. This is not the case for real signals. It also does not take into account the uncertainties associated to the signal shape and the background model.

Depending on the signal shape used, the SWIFT scans identify different regions in the data as being the most significant. This results from incorporating the full information about the signal and background shapes along with their uncertainties. For example, for narrow-width resonances (using the resolution-width Gaussian shapes), it identifies the region at 4.5 TeV with a global p-value of 0.66. This result is consistent with BUMPHUNTER's result. For realistic signal shapes, like  $q^*$ , it identifies the region at 1.6 TeV as the most significant.

The 95% CL upper limits exclude  $q^*$  below 5.6 TeV and  $W'$  below 3 TeV and between 3.3–3.4 TeV. The limits include systematic uncertainties on the background parameters, the background function, the signal JES, the PDF and luminosity. The dominant uncertainty is the uncertainty on the background parameters, hence the sensitivity is statistically limited.

## CHAPTER 9

# Conclusion

This thesis presented a search for new phenomena decaying to two jets using a new statistical tool, SWIFT. This tool was created to address the challenges faced by analyses in the new regime of extremely large LHC datasets. Its robustness was demonstrated by a collection of positive results in spurious signal, linearity and signal injections tests.

The search presented in this thesis was conducted using  $37 \text{ fb}^{-1}$  of proton-proton collision data produced by the LHC at  $\sqrt{s} = 13 \text{ TeV}$  and collected by the ATLAS detector. Both general and model-dependent searches were performed; the former using Gaussian models, and the latter using excited quarks and heavy gauge bosons. Additionally, the SWIFT background was used in conjunction with the BUMPHUNTER to perform a completely model-independent search. This combination of the SWIFT background with BUMPHUNTER has been used by several ATLAS analyses, both published [50, 115] and in progress.

As no evidence of any excess above the Standard Model expectation was observed, 95% confidence-level upper limits were calculated on the cross-sections of all the signals. Excited quarks were excluded below 5.6 TeV; new heavy charged gauge bosons were excluded below 3 TeV and between 3.3 – 3.4 TeV.

## APPENDIX A

### SWiFt Search and Limit Auxiliary Plots

The auxiliary plots from SWiFt's resonance searches using the Gaussian (resolution, 5%, 7%, 10% ),  $q^*$  and  $W'$  signals are shown here. For each signal, the following plots are shown:

- the window with the most significant excess,
- the local and global p-values of the most significant excess,
- the signal and  $\chi^2$  p-values as a function of signal mass,
- the pull plots for the systematic uncertainty nuisance parameters for the best fits as a function of signal mass,
- the pull plots for the systematic uncertainty nuisance parameters for the 95% CL upper limit fits as a function of signal mass.

The global p-value is calculated from the distribution of the LLHR of the pseudo-experiments from the SWiFt background. The pull plots show the values of the best nuisance parameters for each of the uncertainties. The flat pull plot represents the combination of the PDF and luminosity uncertainties and the three JES pull plots represent the signal shape uncertainties.

# A.1 Resolution-Width Gaussian

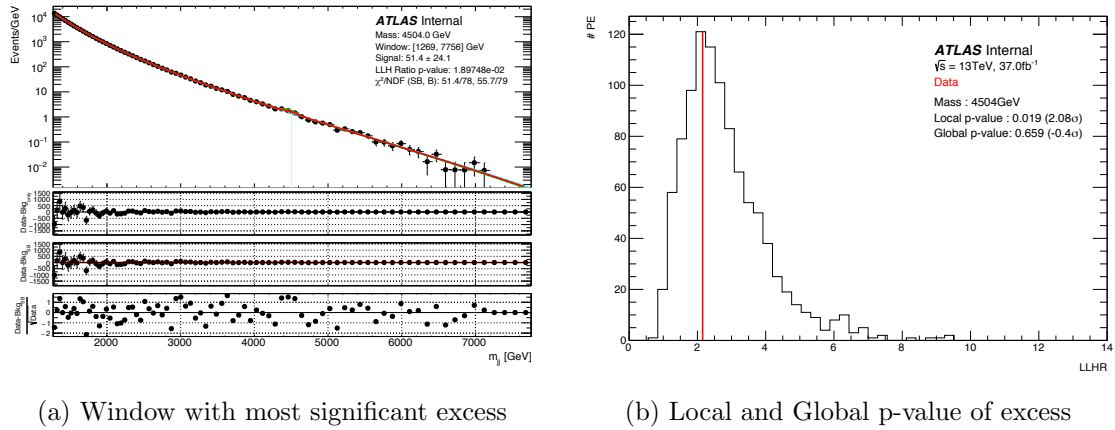


Figure A.1: (a) The window with the largest excess using the resolution-width Gaussian signal shape. This window is centered at 4504 GeV. (b) The local and global p-values of the excess.

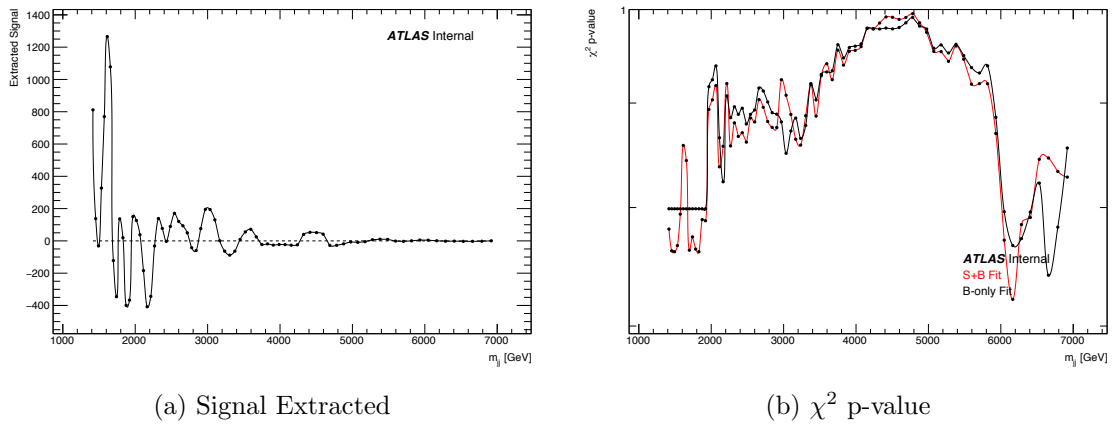
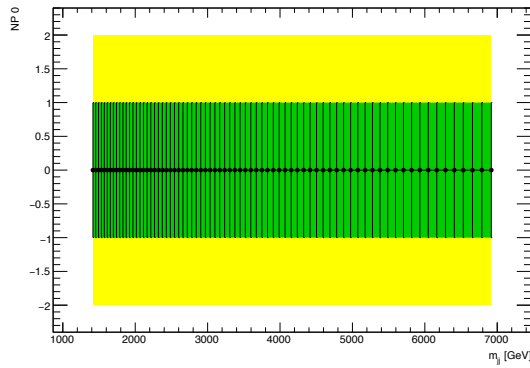
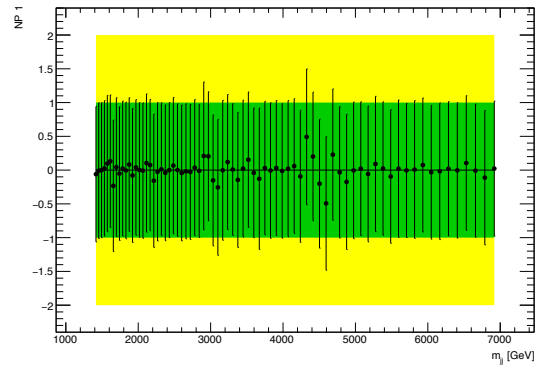


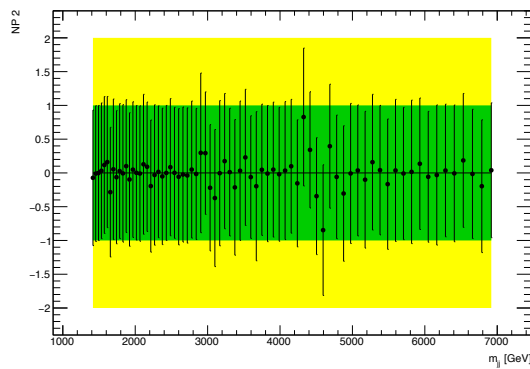
Figure A.2: Signal extracted (a) and  $\chi^2$  p-value (b) as a function of resolution-width Gaussian mass.



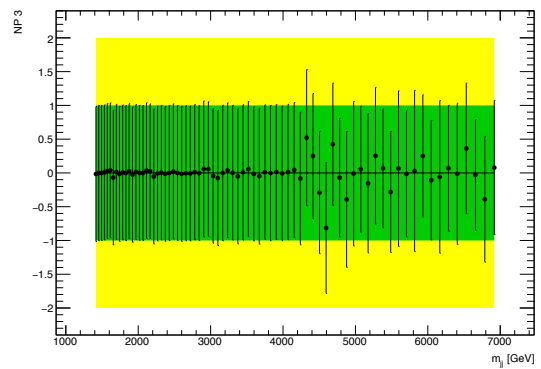
(a) Flat



(b) JES1



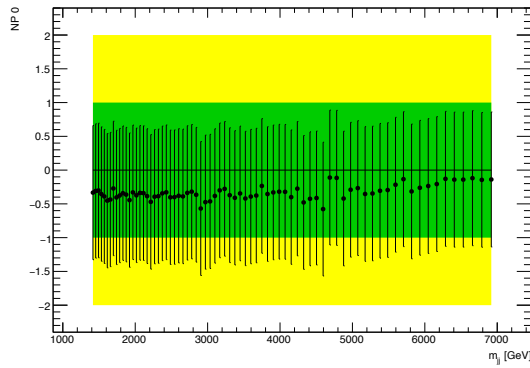
(c) JES2



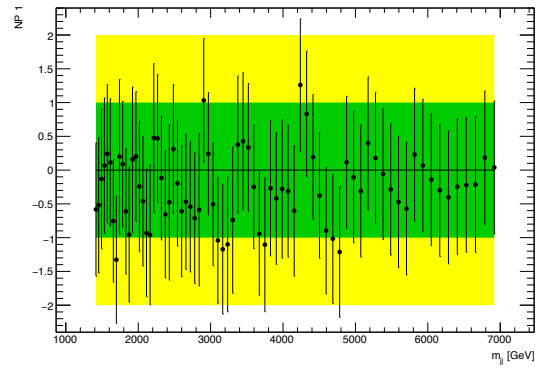
(d) JES3

Figure A.3: Pulls of the systematic uncertainty nuisance parameters for the best fits as a function of the resolution-width Gaussian mass.

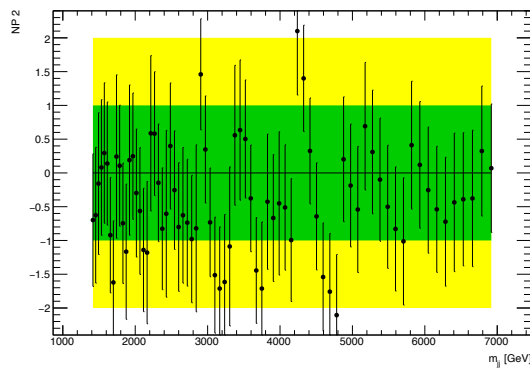




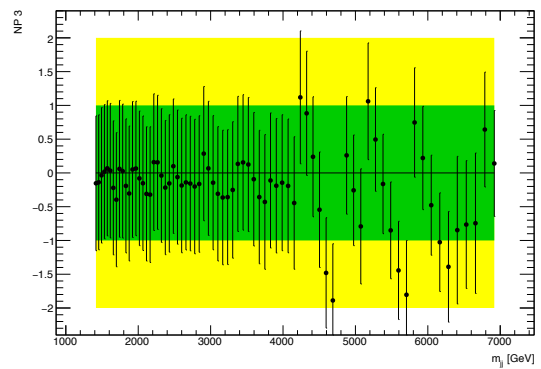
(a) Flat



(b) JES1



(c) JES2



(d) JES3

Figure A.4: Pulls of the nuisance parameters for the 95% CL upper limit fits as a function of resolution-width Gaussian mass.

## A.2 5% Width Gaussian

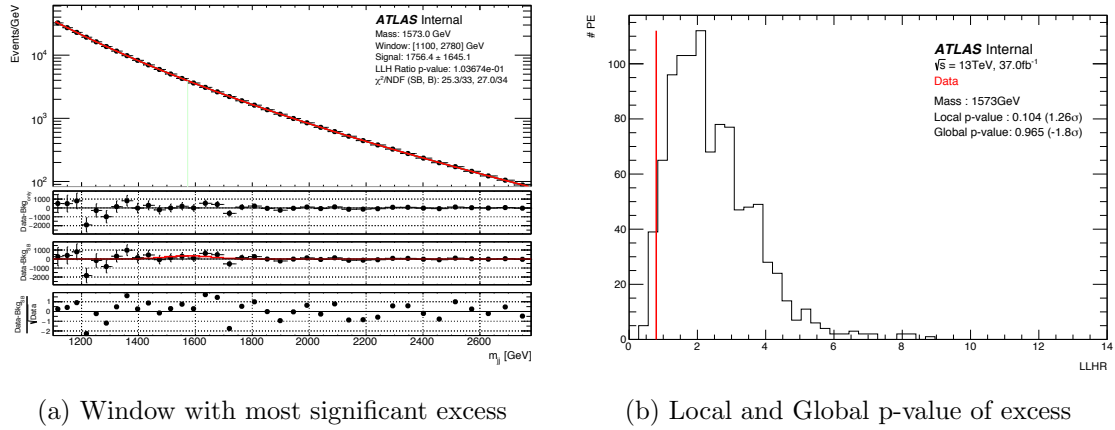


Figure A.5: (a) The window with the largest excess using the 5% width Gaussian signal shape. This window is centered at 1573 GeV. (b) The local and global p-values of the excess.

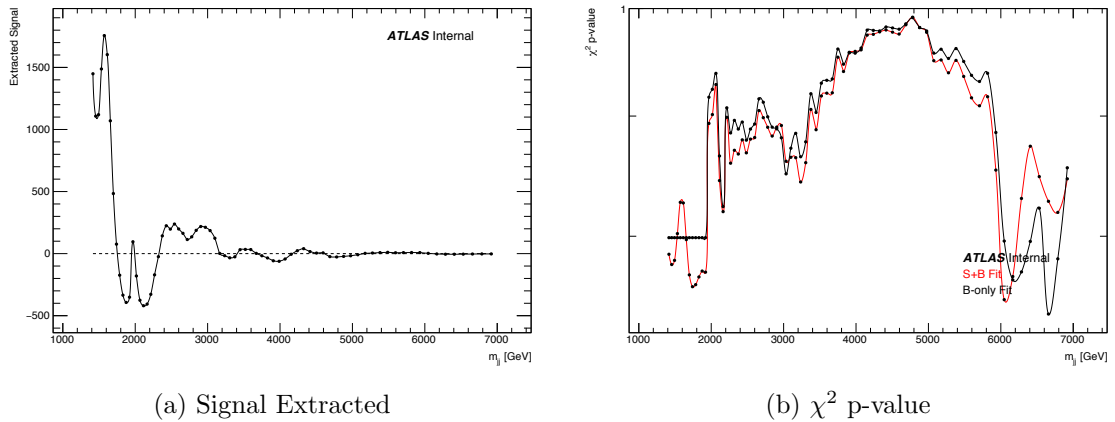
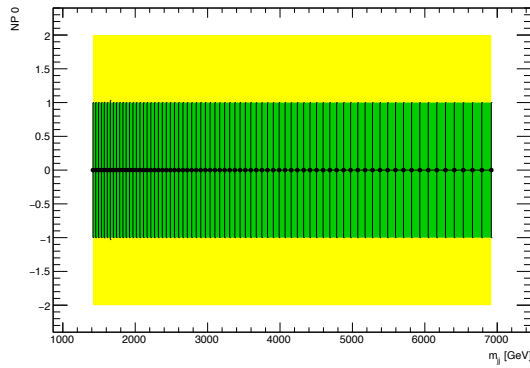
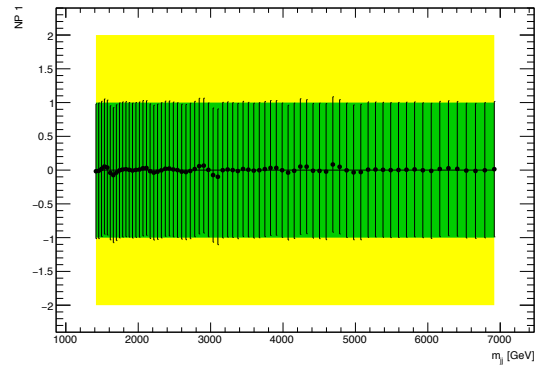


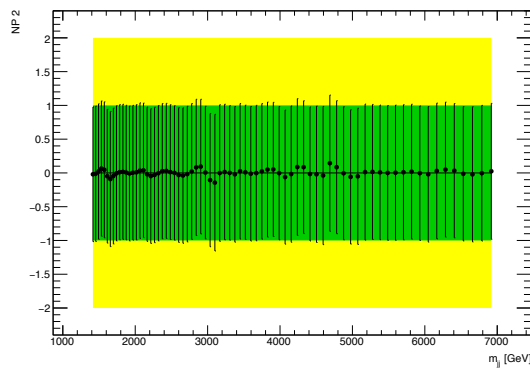
Figure A.6: Signal extracted (a) and  $\chi^2$  p-value (b) as a function of 5% width Gaussian mass.



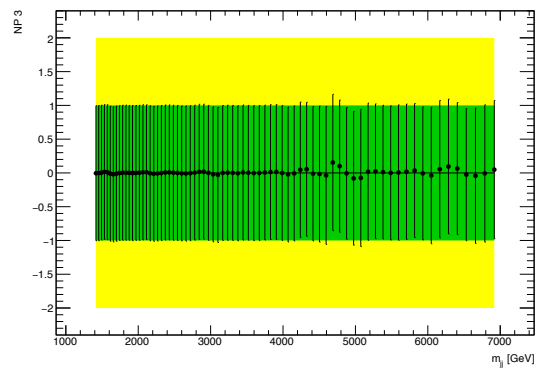
(a) Flat



(b) JES1

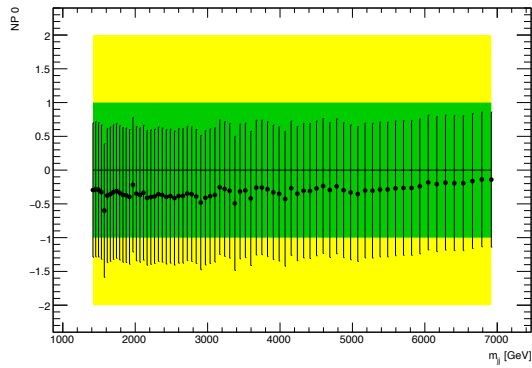


(c) JES2

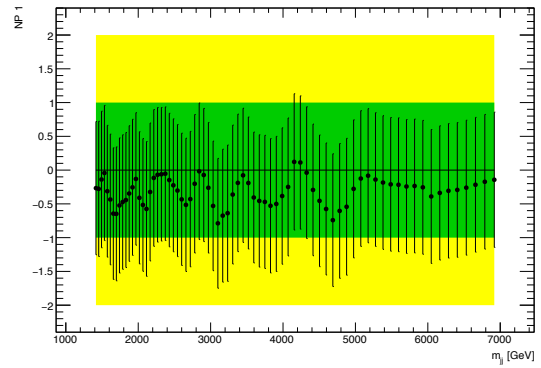


(d) JES3

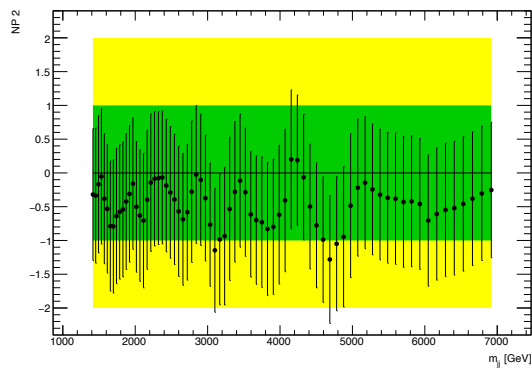
Figure A.7: Pulls of the systematic uncertainty nuisance parameters for the best fits as a function of the 5% width Gaussian mass.



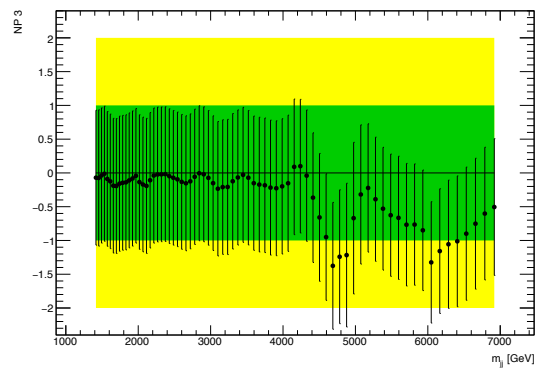
(a) Flat



(b) JES1



(c) JES2



(d) JES3

Figure A.8: Pulls of the nuisance parameters for the 95% CL upper limit fits as a function of 5% width Gaussian mass.

### A.3 7% Width Gaussian

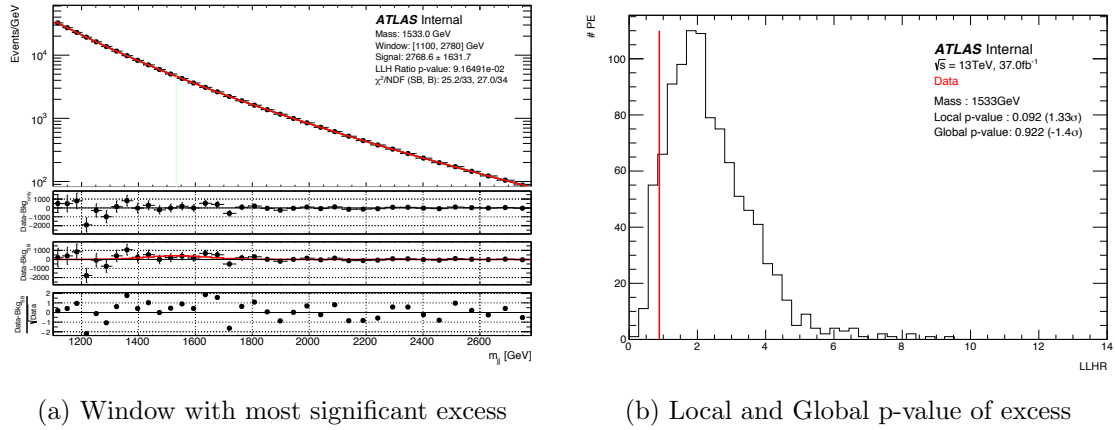


Figure A.9: (a) The window with the largest excess using the 7% width Gaussian signal shape. This window is centered at 1533 GeV. (b) The local and global p-values of the excess.

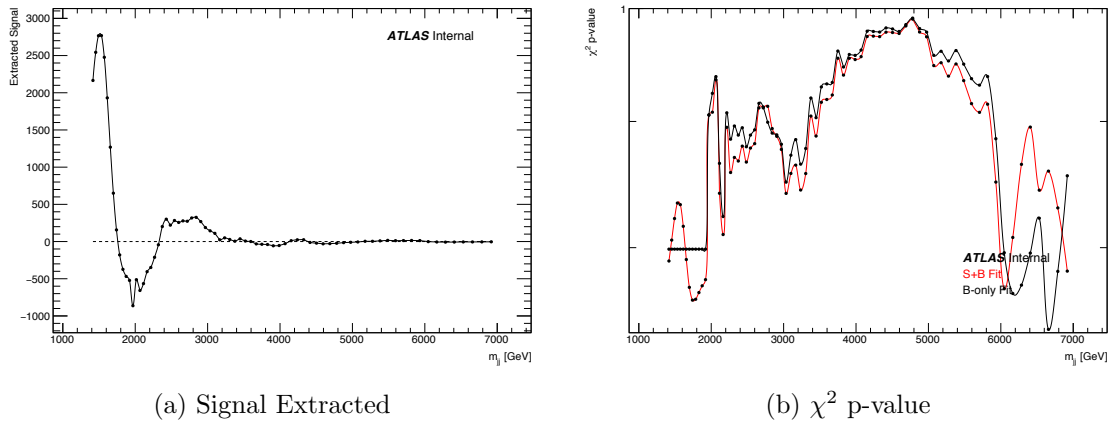
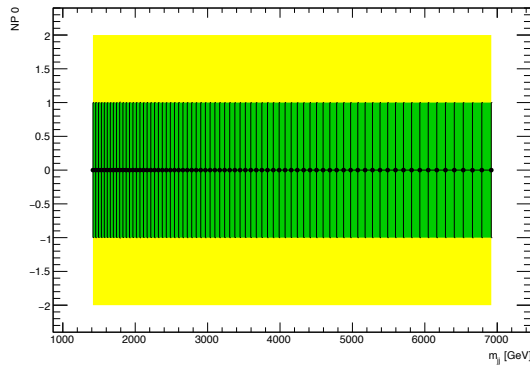
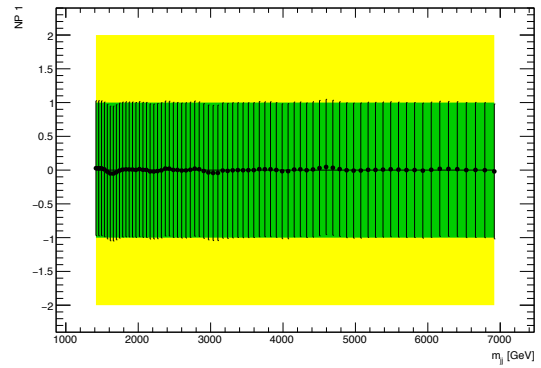


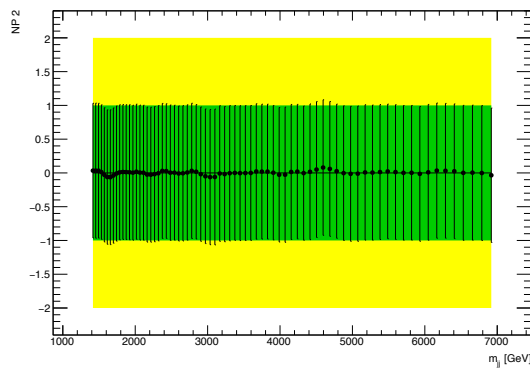
Figure A.10: Signal extracted (a) and  $\chi^2$  p-value (b) as a function of 7% width Gaussian mass.



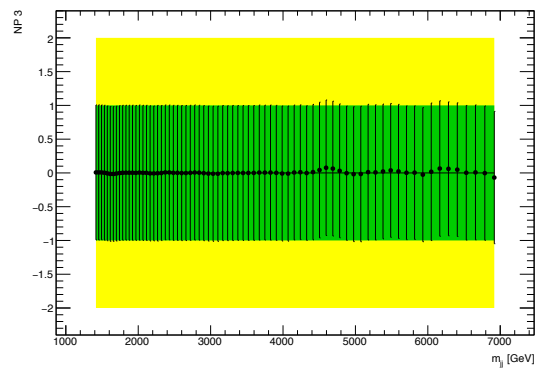
(a) Flat



(b) JES1

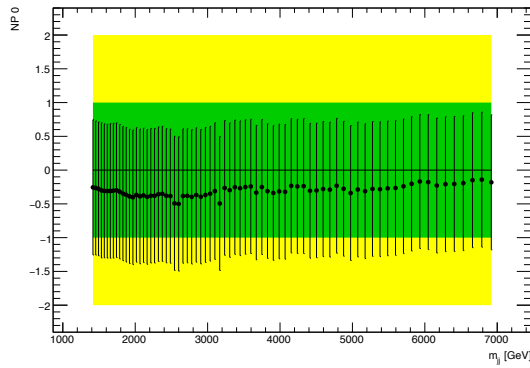


(c) JES2

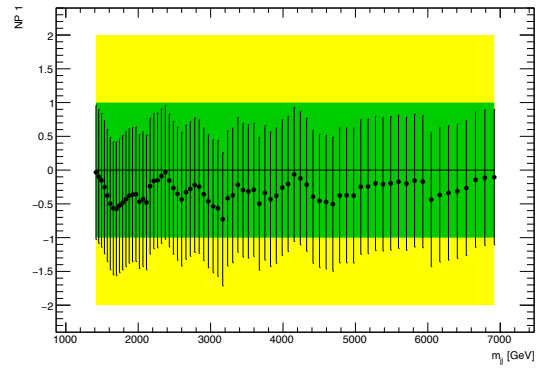


(d) JES3

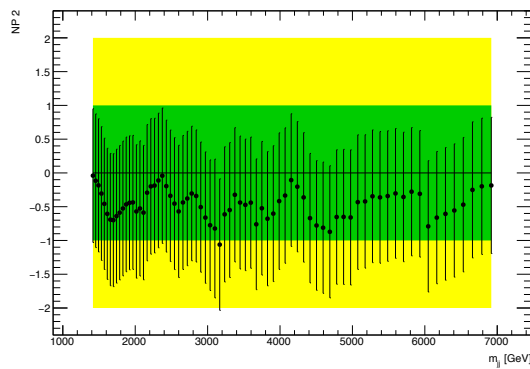
Figure A.11: Pulls of the systematic uncertainty nuisance parameters for the best fits as a function of the 7% width Gaussian mass.



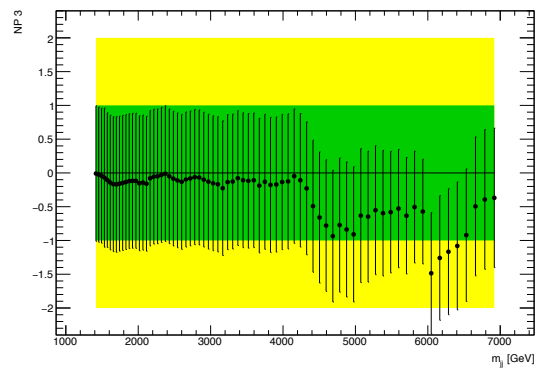
(a) Flat



(b) JES1



(c) JES2



(d) JES3

Figure A.12: Pulls of the nuisance parameters for the 95% CL upper limit fits as a function of 7% width Gaussian mass.

## A.4 10% Width Gaussian

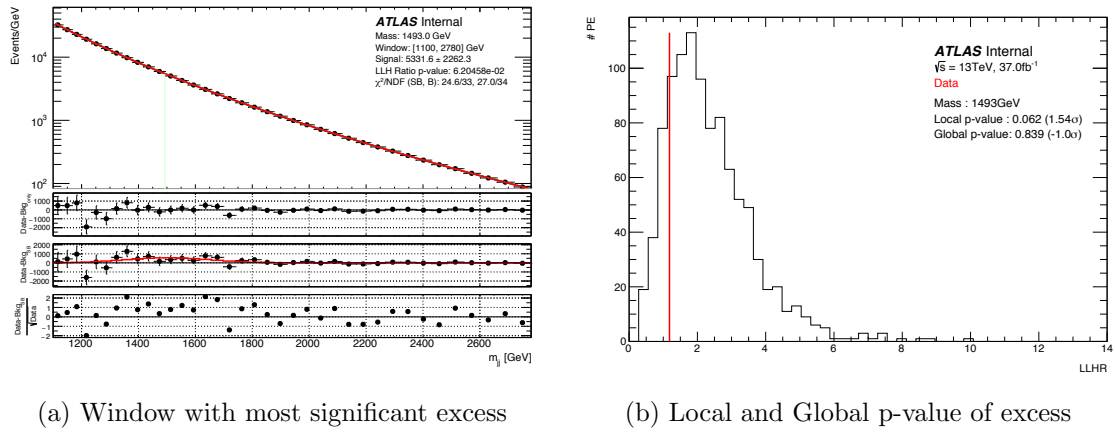


Figure A.13: (a) The window with the largest excess using the 10% width Gaussian signal shape. This window is centered at 1493 GeV. (b) The local and global p-values of the excess.

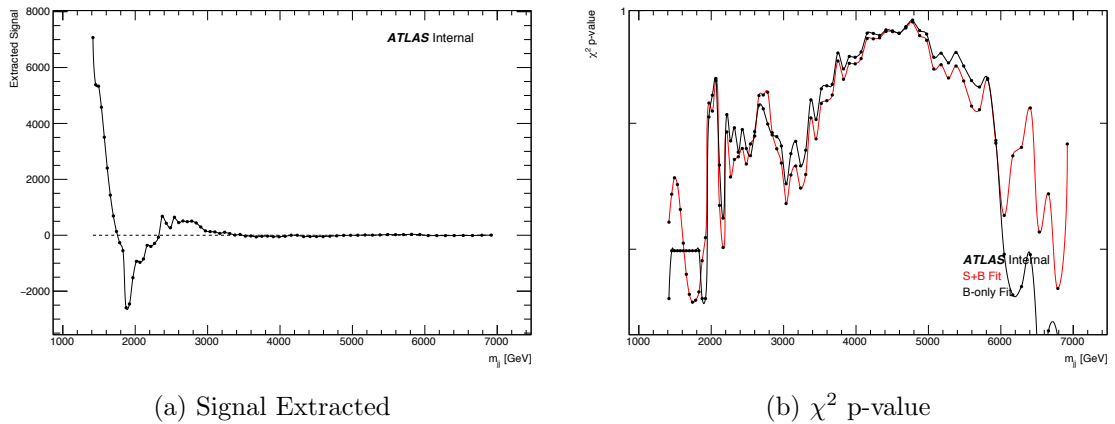
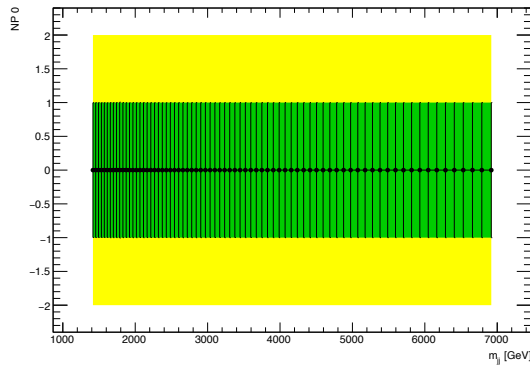
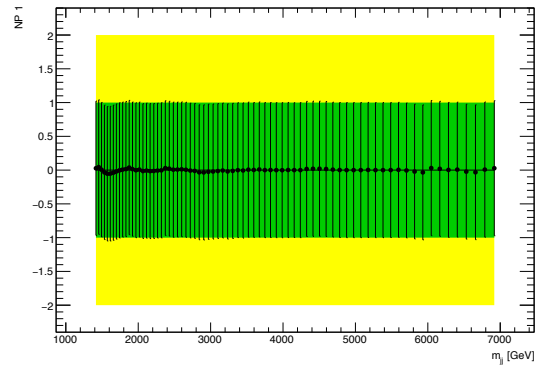


Figure A.14: Signal extracted (a) and  $\chi^2$  p-value (b) as a function of 10% width Gaussian mass.

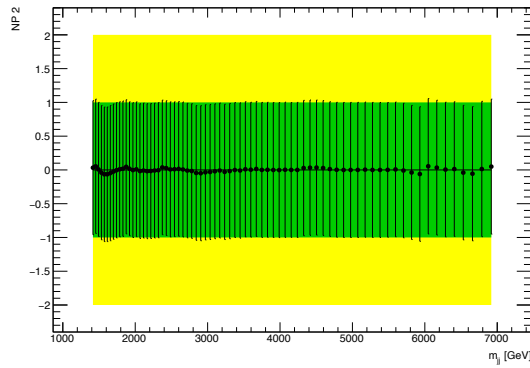




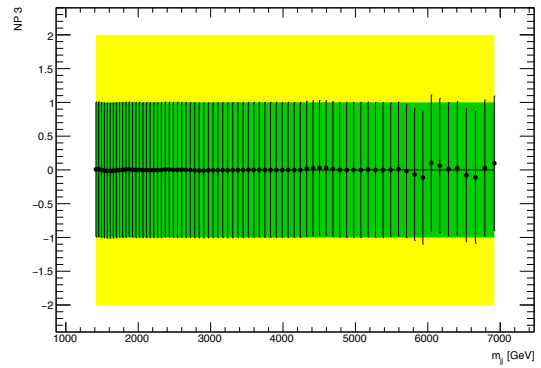
(a) Flat



(b) JES1

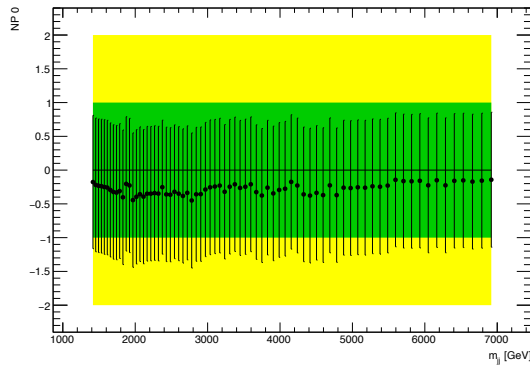


(c) JES2

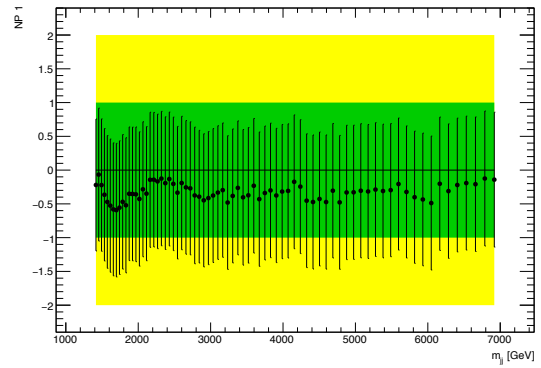


(d) JES3

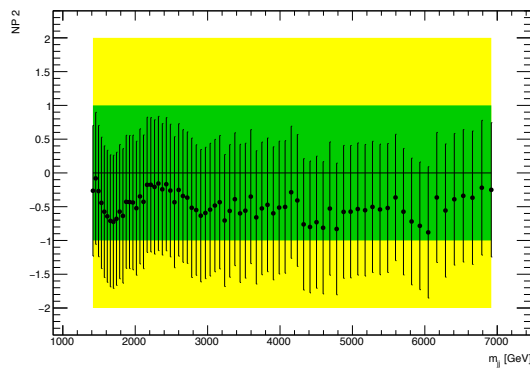
Figure A.15: Pulls of the systematic uncertainty nuisance parameters for the best fits as a function of the 10% width Gaussian mass.



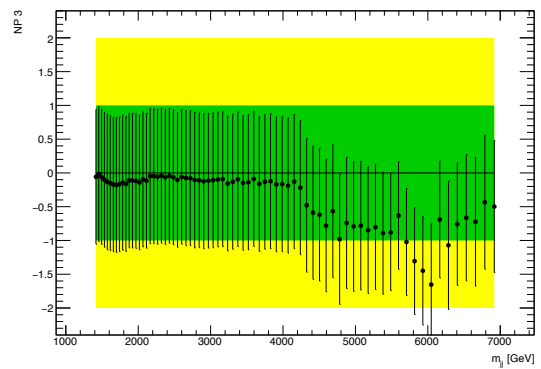
(a) Flat



(b) JES1



(c) JES2



(d) JES3

Figure A.16: Pulls of the nuisance parameters for the 95% CL upper limit fits as a function of 10% width Gaussian mass.

## A.5 $q^*$ Results

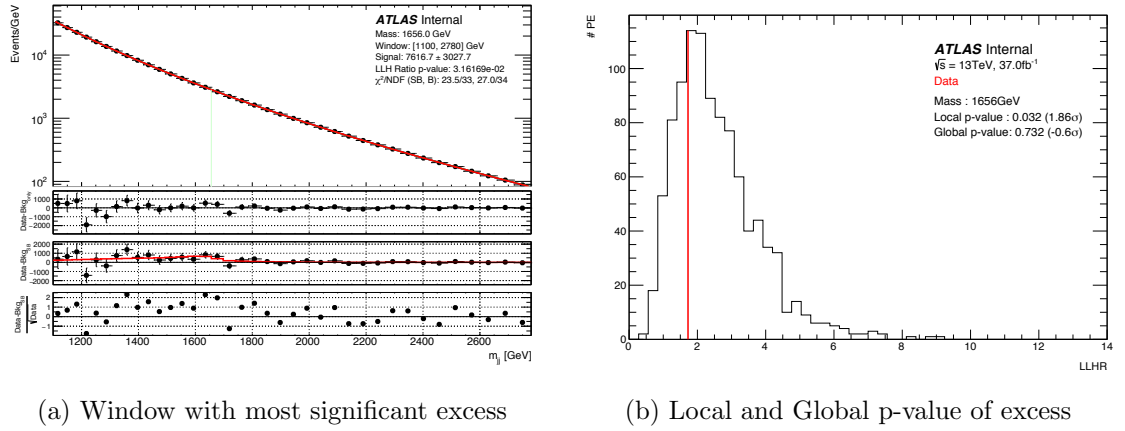


Figure A.17: (a) The window with the largest excess using the  $q^*$  signal shape. This window is centered at 1653 GeV. (b) The local and global p-values of the excess.

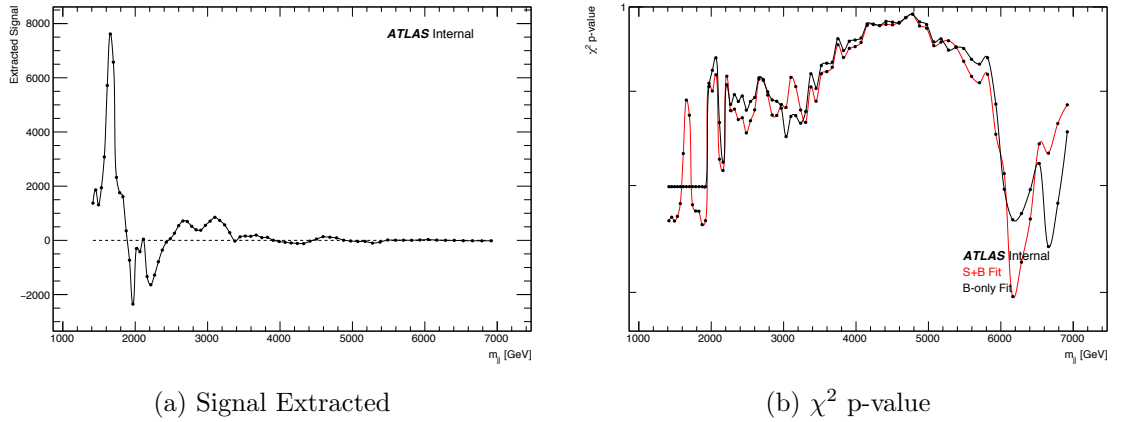
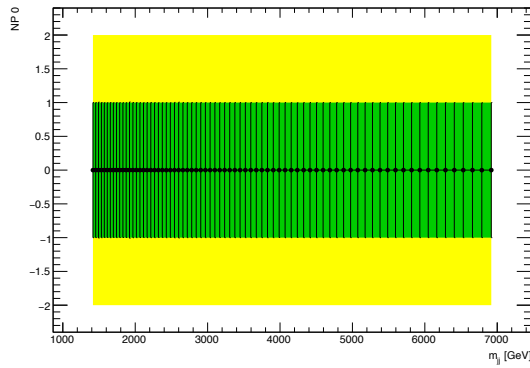
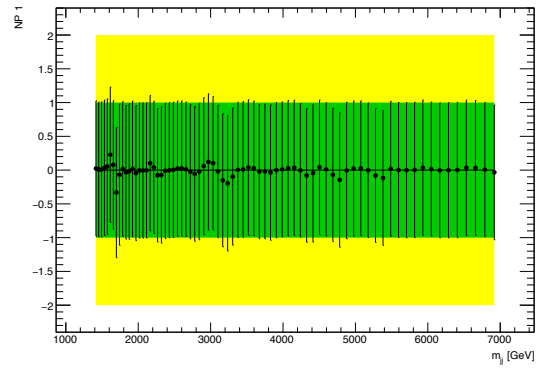


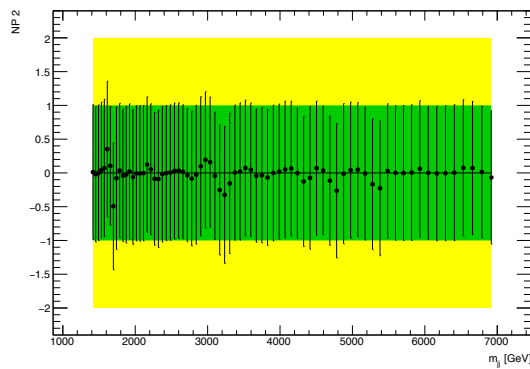
Figure A.18: Signal extracted (a) and  $\chi^2$  p-value (b) as a function of  $q^*$  mass.



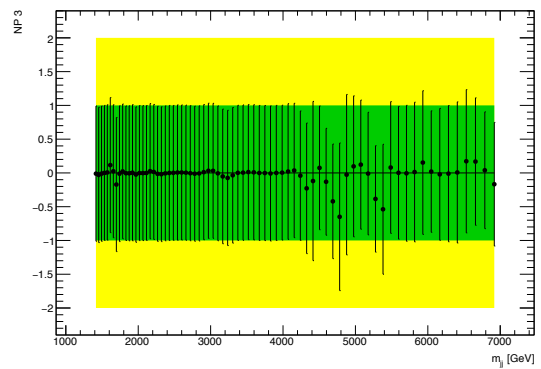
(a) Flat



(b) JES1

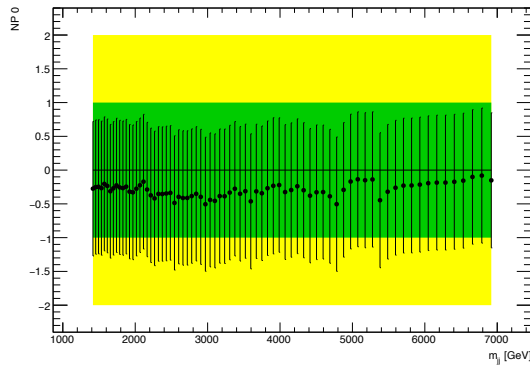


(c) JES2

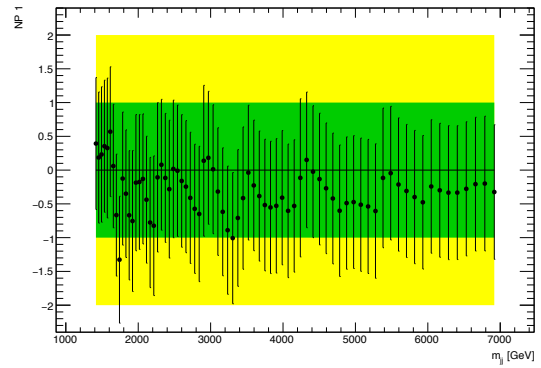


(d) JES3

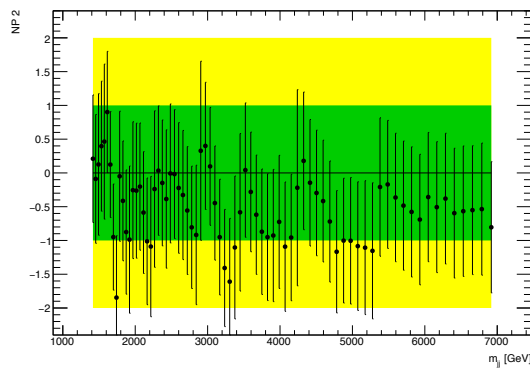
Figure A.19: Pulls of the systematic uncertainty nuisance parameters for the best fits as a function of  $q^*$  mass.



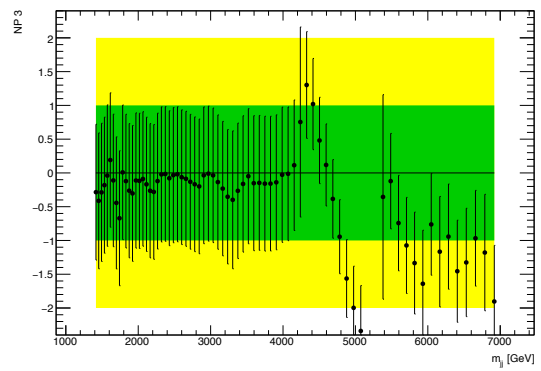
(a) Flat



(b) JES1



(c) JES2



(d) JES3

Figure A.20: Pulls of the nuisance parameters for the 95% CL upper limit fits as a function of  $q^*$  mass.

## APPENDIX B

### Signal Morphing

MC signal shapes can be generated for a limited number of masses only, due to the computer time it takes to simulate them. This is why the ability to interpolate between the generated signal shapes, to obtain intermediate signal shapes, is valuable. SWIFT achieves this by first parameterizing the generated MC signal shapes and then interpolating between the fit parameters using cubic splines.

The parameterization used for all the signal shapes is the six parameter, *gaussian* + *reverse landau* function, defined as

$$\text{GrL}(x) = p_0 [ p_3 \text{Gaus}(x, p_1, p_2) + (1 - p_3) \text{Landau}(-x, p_4, p_5) ], \quad (\text{B.1})$$

where  $p_i$  are the function parameters:

- $p_0$  - signal normalization
- $p_1$  - Gaussian mean
- $p_2$  - Gaussian width
- $p_3$  - fraction of gaussian/landau components
- $p_4$  - Landau mean
- $p_5$  - Landau width

Once successful fits have been achieved the fit parameters (as a function of mass) are interpolated using cubic splines. Intermediate signal shapes are then created by evaluating the splines at the desired masses. This process is shown for the  $q^*$  and  $W'$  signals. Figures B.1 and B.2 show the *gaussian + reverse landau* fits to the MC signal samples. Figures B.3 and B.4 show the spline fits of the fit parameters as a function to mass. Finally, figures B.5 and B.6 show the interpolated signal shapes in pink.

Even though the analysis presented in this thesis does not search for  $Z'$ 's, signal morphing results using the *gaussian + reverse landau* function are shown in Figure B.7. This demonstrates the effectiveness of the morphing procedure.

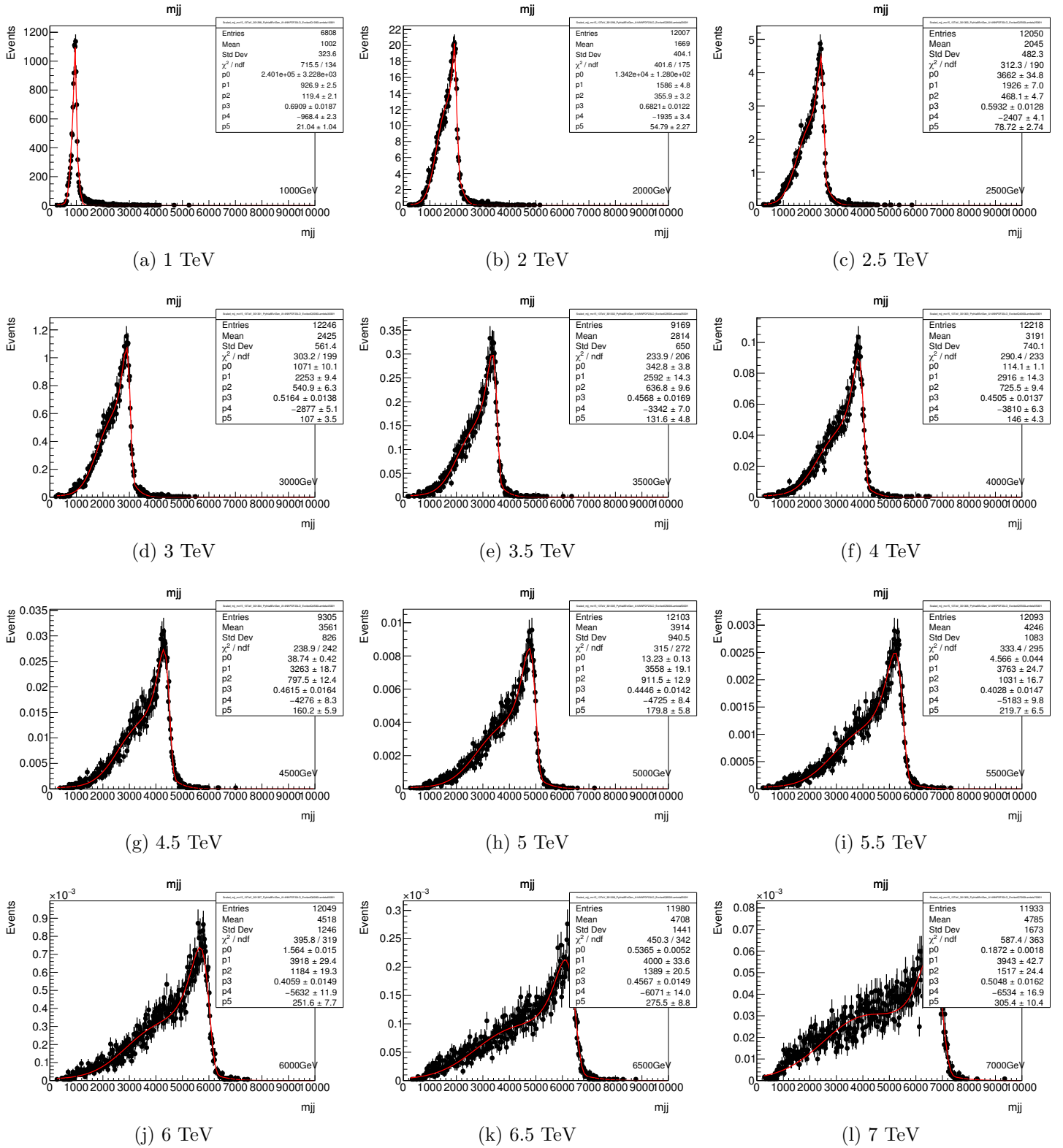


Figure B.1: Gaussian + reverse Landau fits to  $q^*$  MC signal samples after resonance selection.



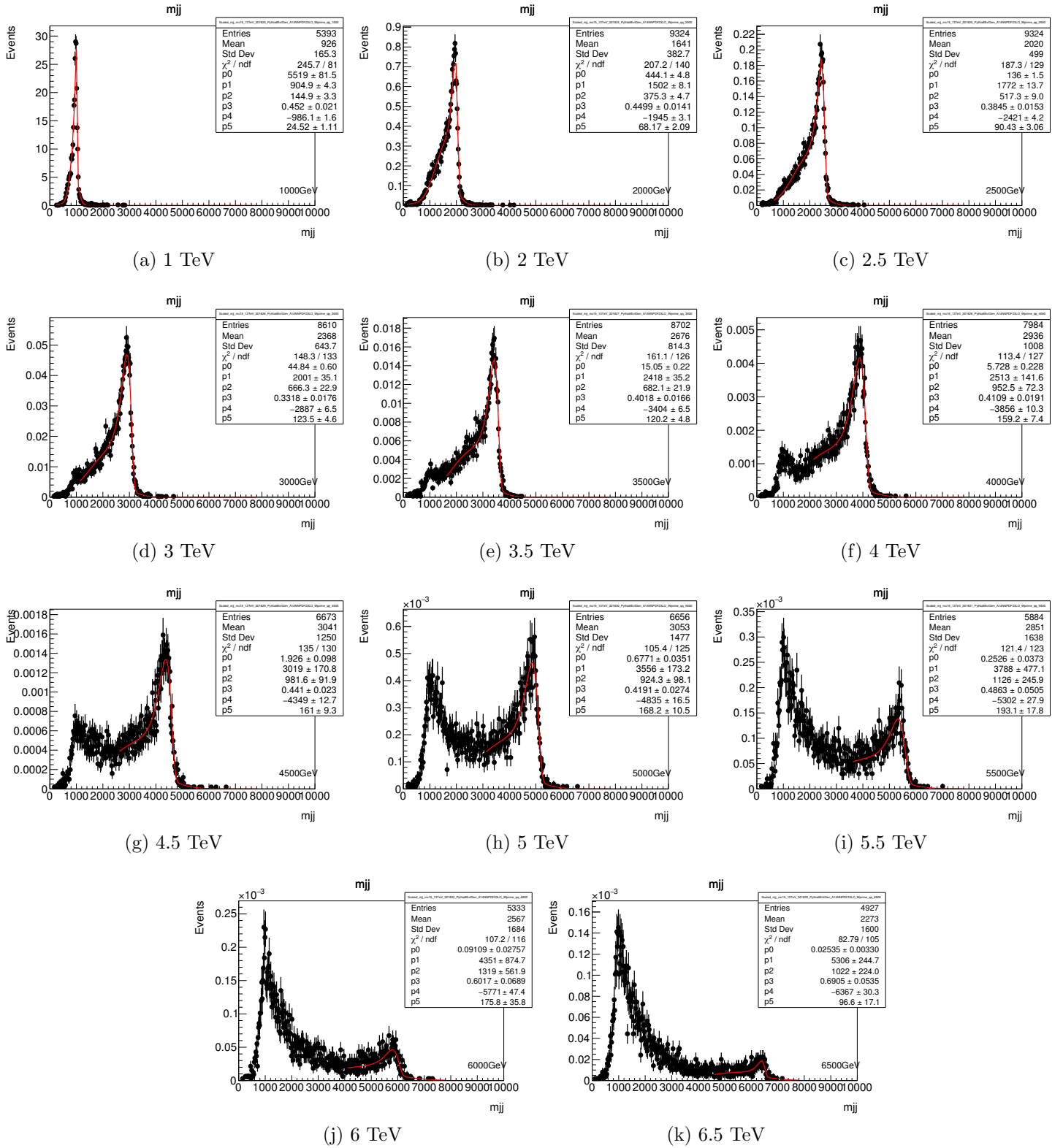
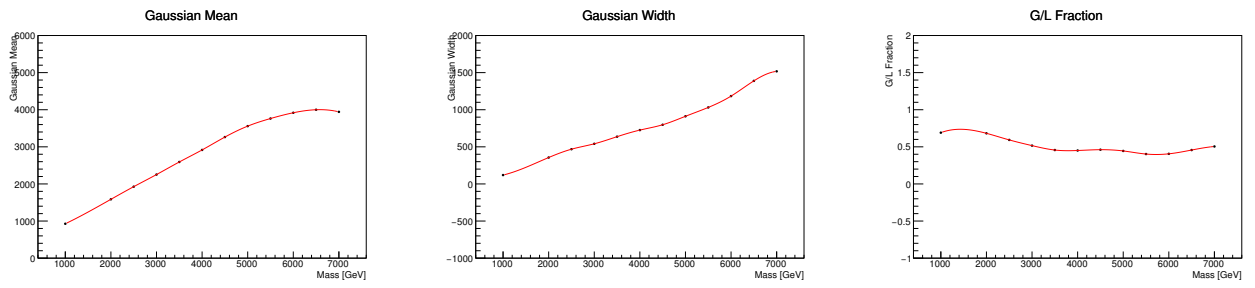


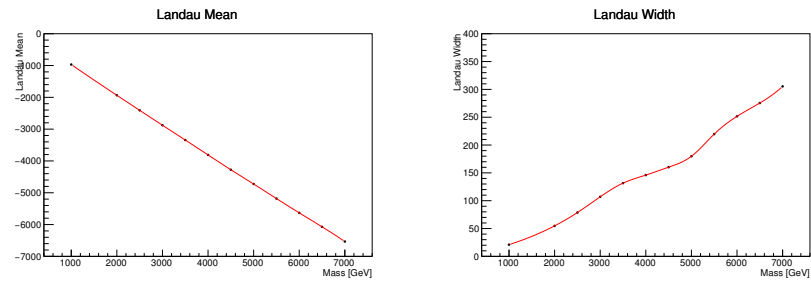
Figure B.2: Gaussian + reverse Landau fits to  $W'$  MC signal samples after resonance selection.



(a) Gaussian Mean

(b) Gaussian Width

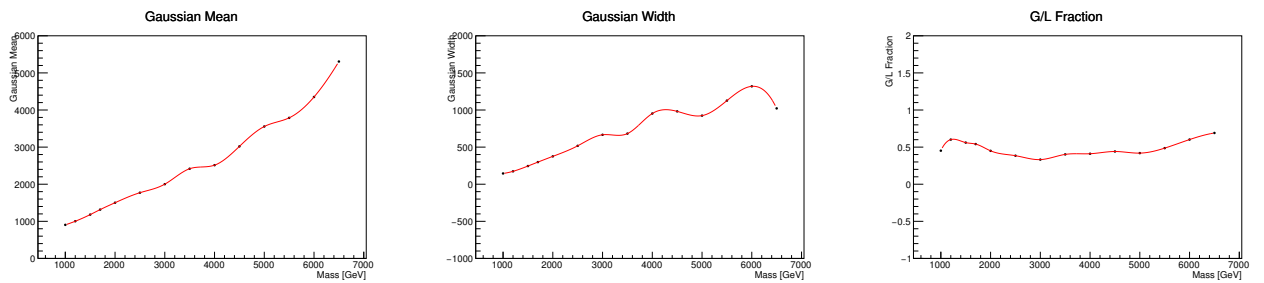
(c) G/L Fraction



(d) Landau Mean

(e) Landau Width

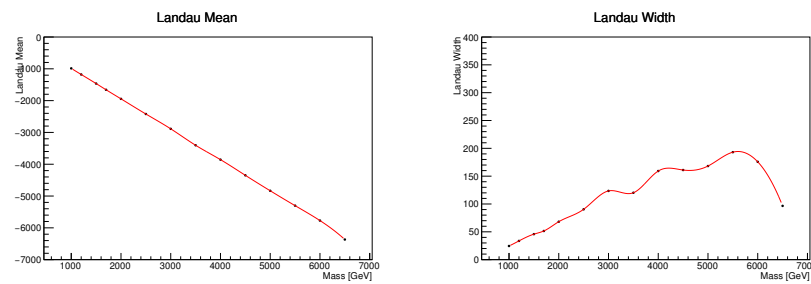
Figure B.3: Cubic spline fits to fit parameters from Figure B.1.



(a) Gaussian Mean

(b) Gaussian Width

(c) G/L Fraction



(d) Landau Mean

(e) Landau Width

Figure B.4: Cubic spline fits to fit parameters from Figure B.2.

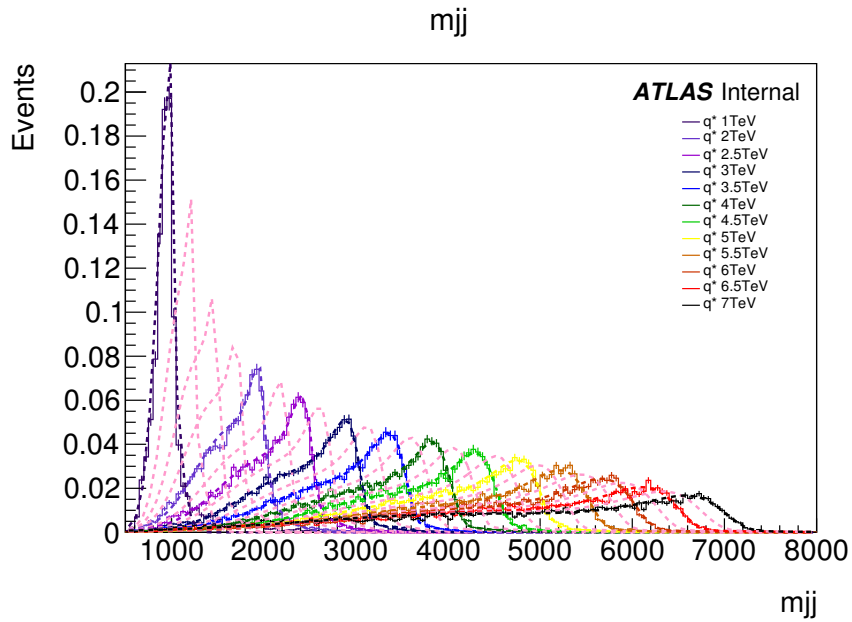


Figure B.5: Signal morphing results of  $q^*$  signals. The colored histograms in the legend show the MC signal shapes, while the matching colored dotted curves show the fits to the MC. The dotted pink curves are the morphed signal shapes.

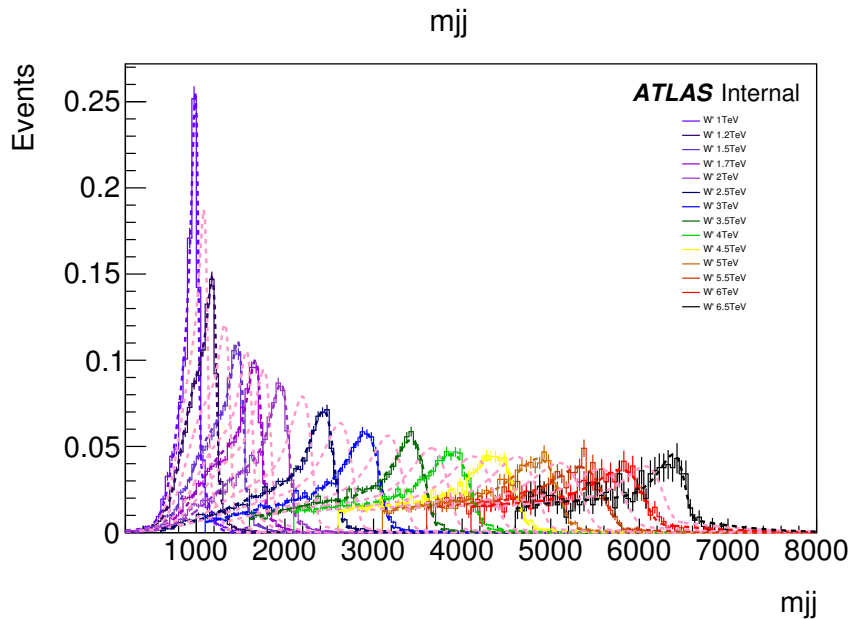


Figure B.6: Signal morphing results of  $W'$  signals. The colored histograms in the legend show the MC signal shapes, while the matching colored dotted curves show the fits to the MC. The dotted pink curves are the morphed signal shapes.

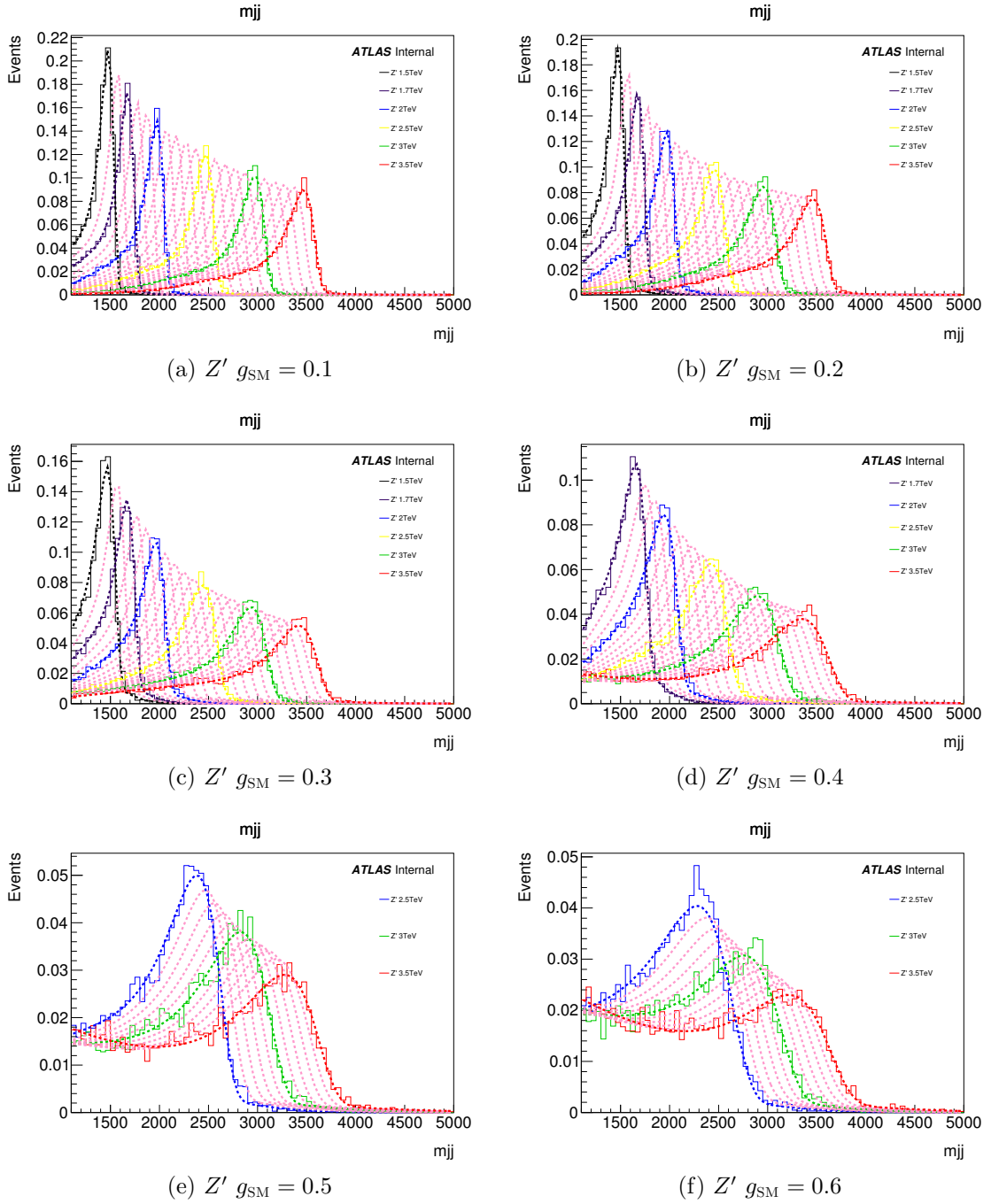


Figure B.7: Signal morphing results of  $Z'$  signals with different couplings to quarks. The colored histograms in the legend show the MC signal shapes, while the matching colored dotted curves show the fits to the MC. The dotted pink curves are the morphed signal shapes.

## REFERENCES

- [1] MissMJ, Nasfarley88 and others, Wikimedia Commons, 2014, <https://commons.wikimedia.org/w/index.php?curid=36335876>.
- [2] Gonis from es, Wikimedia Commons, 2007, <https://commons.wikimedia.org/w/index.php?curid=1556732>.
- [3] Patrignani, C. et al., “Review of Particle Physics,” *Chin. Phys.*, Vol. C40, No. 10, 2016, pp. 100001.
- [4] Rojo, J. e. a., “The PDF4LHC report on PDFs and LHC data: results from Run I and preparation for Run II,” *Journal of Physics G: Nuclear and Particle Physics*, Vol. 42, No. 10, 2015, pp. 103103, <http://stacks.iop.org/0954-3899/42/i=10/a=103103>.
- [5] Mobs, E., “The CERN accelerator complex. Complexe des accélérateurs du CERN,” Jul 2016, <https://cds.cern.ch/record/2197559>.
- [6] Team, A., “Computer-generated diagram of an LHC dipole. Schéma d’un dipôle du LHC,” <https://cds.cern.ch/record/39731>.
- [7] Brice, M., “First LHC magnets installed. Installation du premier aimant du LHC,” <https://cds.cern.ch/record/834351>.
- [8] ATLAS collaboration, “LuminosityPublicResultsRun2,” [https://twiki.cern.ch/twiki/bin/view/AtlasPublic/LuminosityPublicResultsRun2#Luminosity\\_summary\\_plots\\_for\\_201](https://twiki.cern.ch/twiki/bin/view/AtlasPublic/LuminosityPublicResultsRun2#Luminosity_summary_plots_for_201).
- [9] ATLAS Collaboration, “The ATLAS Experiment at the CERN Large Hadron Collider,” *JINST*, Vol. 3, No. 08, 2008, pp. S08003, <http://stacks.iop.org/1748-0221/3/i=08/a=S08003>.
- [10] Pequeno, J. and Schaffner, P., “An computer generated image representing how ATLAS detects particles,” <https://cds.cern.ch/record/1505342>.
- [11] ATLAS collaboration, “Pixel detector B layer,” <https://atlas.cern/updates/atlas-news/pixels-system-last-not-late>.

- [12] Dobos, D., “Rendered ATLAS Pixel Module closeups,” <https://cds.cern.ch/record/854105>.
- [13] Brice, M., “Vue divers du sub-detector Silicon Tracker de l’expérience Atlas,” <https://cds.cern.ch/record/883305>.
- [14] Kondo, T., “SCT Module,” <http://atlas.kek.jp/sub/photos/SCTJ/SCTJModule/SCTJModule.html>.
- [15] Brice, M., “Prparation des dtecteurs internes TRT de l’expérience ATLAS dans la salle propre SR du point 1.” <https://cds.cern.ch/record/865952>.
- [16] Romaniouk, A., “TRT Tube,” <http://particle.mephi.ru/en/research/atlas/trt/>.
- [17] Pequenaio, J., “Computer Generated image of the ATLAS calorimeter,” <https://cds.cern.ch/record/1095927>.
- [18] Brice, M., “ATLAS barrel detector,” <https://cds.cern.ch/record/619028>.
- [19] Brice, M., “ATLAS electromagnetic calorimeter after cabling, after insertion.. Calorimtre lectromagntique ATLAS aprs cblage, aprs insertion,” <https://cds.cern.ch/record/615897>.
- [20] Guiraud, L., “Various phases of the instrumentation of the ATLAS barrel tile calorimeter at CERN: Phase III,” <https://cds.cern.ch/record/40849>.
- [21] Brice, M., “Btiment de stockage des tuiles du calorimetre ATLAS,” <https://cds.cern.ch/record/682387>.
- [22] Aloisio, A. and M. Alvigi, e. a., “The trigger chambers of the ATLAS muon spectrometer: production and tests,” *Nuclear Instruments and Methods in Physics Research Section A: Accelerators, Spectrometers, Detectors and Associated Equipment*, Vol. 535, No. 1, 2004, pp. 265 – 271, Proceedings of the 10th International Vienna Conference on Instrumentation.
- [23] Brice, M., “Essai d’insertion du solenoide dans LAr (liquide Argon) EM-Barrel Calorimtre,” <https://cds.cern.ch/record/712128>.
- [24] Brice, M., “Installing the ATLAS calorimeter. Vue centrale du dtecteur ATLAS avec ses huit toroides entourant le calorimtre avant son dplacement au centre du dtecteur,” <https://cds.cern.ch/record/910381>.
- [25] “Barrel-toroid: BT-1: transport,” <https://cds.cern.ch/record/892282>.

- [26] Marcelloni, C., “Beginning of transport of ATLAS End Cap Toroid from between building 191 to building 180,” <https://cds.cern.ch/record/1015713>.
- [27] WLCG, “Grid activity on Google Earth,” <http://wlcg.web.cern.ch/wlcg-google-earth-dashboard>.
- [28] Collaboration, C., “Jet Production,” <https://www.quantumdiaries.org/2010/10/22/qcd-and-confinement/>.
- [29] Cacciari, M., Salam, G. P., and Soyez, G., “The anti- $k_t$  jet clustering algorithm,” *Journal of High Energy Physics*, Vol. 2008, No. 04, 2008, pp. 063, <http://stacks.iop.org/1126-6708/2008/i=04/a=063>.
- [30] ATLAS Collaboration, “Jet energy scale measurements and their systematic uncertainties in proton-proton collisions at  $\sqrt{s} = 13$  TeV with the ATLAS detector,” *Phys. Rev.*, Vol. D96, No. 7, 2017, pp. 072002.
- [31] ATLAS Collaboration, “Public plots: Jet energy scale uncertainties updated for ICHEP 2016 using full 13 TeV 2015 dataset,” <https://atlas.web.cern.ch/Atlas/GROUPS/PHYSICS/PLOTS/JETM-2016-010/>.
- [32] ATLAS Collaboration, “JES Public Plots for Moriond 2017,” <https://atlas.web.cern.ch/Atlas/GROUPS/PHYSICS/PLOTS/JETM-2017-003/>.
- [33] JabberWok at English Wikipedia, “A Feynman diagram of an s-channel process,” 2006, <https://commons.wikimedia.org/wiki/File:S-channel.svg>.
- [34] JabberWok at English Wikipedia, “A Feynman diagram of a t-channel process,” 2006, <https://commons.wikimedia.org/wiki/File:T-channel.svg>.
- [35] JabberWok at English Wikipedia, “A Feynman diagram of a u-channel process,” 2006, <https://commons.wikimedia.org/wiki/File:U-channel.svg>.
- [36] Ellis, R. K., Stirling, W. J., and Webber, B. R., “QCD and collider physics,” *Camb. Monogr. Part. Phys. Nucl. Phys. Cosmol.*, Vol. 8, 1996, pp. 1–435.
- [37] ATLAS Collaboration, “Measurement of inclusive jet and dijet cross-sections in proton-proton collisions at  $\sqrt{s} = 13$  TeV with the ATLAS detector,” 2017.
- [38] ATLAS Collaboration, 2018, [https://atlas.web.cern.ch/Atlas/GROUPS/PHYSICS/CombinedSummaryPlots/SM/ATLAS\\_b\\_SMSummary\\_FiducialXsect/ATLAS\\_b\\_SMSummary\\_FiducialXsect.png](https://atlas.web.cern.ch/Atlas/GROUPS/PHYSICS/CombinedSummaryPlots/SM/ATLAS_b_SMSummary_FiducialXsect/ATLAS_b_SMSummary_FiducialXsect.png).

- [39] Baur, U., Spira, M., and Zerwas, P. M., “Excited-quark and -lepton production at hadron colliders,” *Phys. Rev. D*, Vol. 42, Aug 1990, pp. 815–824, <https://link.aps.org/doi/10.1103/PhysRevD.42.815>.
- [40] ATLAS Collaboration, “Search for light dijet resonances with the ATLAS detector using a Trigger-Level Analysis in LHC pp collisions at  $\sqrt{s} = 13$  TeV,” Tech. Rep. ATLAS-CONF-2016-030, CERN, Geneva, Jun 2016, <https://cds.cern.ch/record/2161135>.
- [41] Scott, P., “Chi-square: Testing for Goodness of Fit,” 2006, <http://maxwell.ucsc.edu/~drip/133/ch4.pdf>.
- [42] Higgs, P. W., “Broken Symmetries and the Masses of Gauge Bosons,” *Phys. Rev. Lett.*, Vol. 13, Oct 1964, pp. 508–509, <https://link.aps.org/doi/10.1103/PhysRevLett.13.508>.
- [43] Englert, F. and Brout, R., “Broken Symmetry and the Mass of Gauge Vector Mesons,” *Phys. Rev. Lett.*, Vol. 13, Aug 1964, pp. 321–323, <https://link.aps.org/doi/10.1103/PhysRevLett.13.321>.
- [44] Guralnik, G. S., Hagen, C. R., and Kibble, T. W. B., “Global Conservation Laws and Massless Particles,” *Phys. Rev. Lett.*, Vol. 13, Nov 1964, pp. 585–587, <https://link.aps.org/doi/10.1103/PhysRevLett.13.585>.
- [45] ATLAS Collaboration, “Observation of a new particle in the search for the Standard Model Higgs boson with the ATLAS detector at the LHC,” *Physics Letters B*, Vol. 716, No. 1, 2012, pp. 1 – 29, <http://www.sciencedirect.com/science/article/pii/S037026931200857X>.
- [46] CMS Collaboration, “Observation of a new boson at a mass of 125 GeV with the CMS experiment at the LHC,” *Physics Letters B*, Vol. 716, No. 1, 2012, pp. 30 – 61, <http://www.sciencedirect.com/science/article/pii/S0370269312008581>.
- [47] Andersson, B., Gustafson, G., Ingelman, G., and Sjostrand, T., “Parton Fragmentation and String Dynamics,” *Phys. Rept.*, Vol. 97, 1983, pp. 31–145.
- [48] Bahcall, N. A., “Dark matter universe,” *Proceedings of the National Academy of Sciences*, Vol. 112, No. 40, 2015, pp. 12243–12245, <http://www.pnas.org/content/112/40/12243>.
- [49] Peebles, P. J. E. and Ratra, B., “The Cosmological constant and dark energy,” *Rev. Mod. Phys.*, Vol. 75, 2003, pp. 559–606, [592(2002)].
- [50] ATLAS Collaboration, “Search for new phenomena in dijet events using 37 fb<sup>-1</sup> of pp collision data collected at  $\sqrt{s} = 13$  TeV with the ATLAS detector,” *Phys. Rev.*, Vol. D96, No. 5, 2017, pp. 052004.



- [51] Evans, L. R. and Bryant, P., “LHC Machine,” *JINST*, Vol. 3, 2008, pp. S08001. 164 p, <https://cds.cern.ch/record/1129806>.
- [52] Bajko, M. and Bertinelli, F, e. a., “Report of the Task Force on the Incident of 19th September 2008 at the LHC,” Tech. Rep. LHC-PROJECT-Report-1168. CERN-LHC-PROJECT-Report-1168, CERN, Geneva, Mar 2009, <https://cds.cern.ch/record/1168025>.
- [53] UA1 Collaboration, “Experimental Observation of Isolated Large Transverse Energy Electrons with Associated Missing Energy at  $\sqrt{s} = 540\text{-GeV}$ ,” *Phys. Lett.*, Vol. 122B, 1983, pp. 103–116, [611(1983)].
- [54] UA1 Collaboration, “Experimental Observation of Lepton Pairs of Invariant Mass Around  $95\text{-GeV}/c^2$  at the CERN SPS Collider,” *Phys. Lett.*, Vol. 126B, 1983, pp. 398–410.
- [55] UA2 Collaboration, “Evidence for  $Z^0 \rightarrow e^+ e^-$  at the CERN anti-p p Collider,” *Phys. Lett.*, Vol. 129B, 1983, pp. 130–140.
- [56] UA2 Collaboration, “Observation of Single Isolated Electrons of High Transverse Momentum in Events with Missing Transverse Energy at the CERN anti-p p Collider,” *Phys. Lett.*, Vol. 122B, 1983, pp. 476–485.
- [57] ALICE Collaboration, “The ALICE experiment at the CERN LHC,” *JINST*, Vol. 3, No. 08, 2008, pp. S08002, <http://stacks.iop.org/1748-0221/3/i=08/a=S08002>.
- [58] CMS Collaboration, “The CMS Experiment at the CERN LHC,” *JINST*, Vol. 3, 2008, pp. S08004.
- [59] LHCb Collaboration, “The LHCb Detector at the LHC,” *JINST*, Vol. 3, No. LHCb-DP-2008-001. CERN-LHCb-DP-2008-001, 2008, pp. S08005, <https://cds.cern.ch/record/1129809>.
- [60] ATLAS Collaboration, *ATLAS inner detector: Technical Design Report, 1*, Technical Design Report ATLAS, CERN, Geneva, 1997, <https://cds.cern.ch/record/331063>.
- [61] Capeans, M., Darbo, G., Einsweiler, K., Elsing, M., Flick, T., Garcia-Sciveres, M., Gemme, C., Pernegger, H., Rohne, O., and Vuillemet, R., “ATLAS Insertable B-Layer Technical Design Report,” Tech. Rep. CERN-LHCC-2010-013. ATLAS-TDR-19, Sep 2010, <https://cds.cern.ch/record/1291633>.
- [62] ATLAS Collaboration, *ATLAS liquid-argon calorimeter: Technical Design Report*, Technical Design Report ATLAS, CERN, Geneva, 1996, <https://cds.cern.ch/record/331061>.

- [63] ATLAS Collaboration, *ATLAS tile calorimeter: Technical Design Report*, Technical Design Report ATLAS, CERN, Geneva, 1996, <https://cds.cern.ch/record/331062>.
- [64] ATLAS Collaboration, *ATLAS muon spectrometer: Technical Design Report*, Technical Design Report ATLAS, CERN, Geneva, 1997, <https://cds.cern.ch/record/331068>.
- [65] ATLAS Collaboration, *ATLAS magnet system: Technical Design Report, 1*, Technical Design Report ATLAS, CERN, Geneva, 1997, <https://cds.cern.ch/record/338080>.
- [66] Martnez, A. R. and Collaboration, A., “The Run-2 ATLAS Trigger System,” *Journal of Physics: Conference Series*, Vol. 762, No. 1, 2016, pp. 012003, <http://stacks.iop.org/1742-6596/762/i=1/a=012003>.
- [67] Shiers, J., “The Worldwide LHC Computing Grid (worldwide LCG),” *Computer Physics Communications*, Vol. 177, No. 1, 2007, pp. 219 – 223, <http://www.sciencedirect.com/science/article/pii/S001046550700077X>.
- [68] ATLAS Collaboration, “Topological cell clustering in the ATLAS calorimeters and its performance in LHC Run 1,” *Eur. Phys. J.*, Vol. C77, 2017, pp. 490.
- [69] Sjstrand, T., Mrenna, S., and Skands, P., “A brief introduction to PYTHIA 8.1,” *Computer Physics Communications*, Vol. 178, No. 11, 2008, pp. 852 – 867, <http://www.sciencedirect.com/science/article/pii/S0010465508000441>.
- [70] ATLAS Collaboration, “Jet energy measurement with the ATLAS detector in proton-proton collisions at  $\sqrt{s} = 7$  TeV,” *The European Physical Journal C*, Vol. 73, No. 3, Mar 2013, pp. 2304, <https://doi.org/10.1140/epjc/s10052-013-2304-2>.
- [71] Alioli, S., Nason, P., Oleari, C., and Re, E., “A general framework for implementing NLO calculations in shower Monte Carlo programs: the POWHEG BOX,” *Journal of High Energy Physics*, Vol. 2010, No. 6, Jun 2010, pp. 43, [https://doi.org/10.1007/JHEP06\(2010\)043](https://doi.org/10.1007/JHEP06(2010)043).
- [72] Gleisberg, T., Hche, S., Krauss, F., Schnherr, M., Schumann, S., Siegert, F., and Winter, J., “Event generation with SHERPA 1.1,” *Journal of High Energy Physics*, Vol. 2009, No. 02, 2009, pp. 007, <http://stacks.iop.org/1126-6708/2009/i=02/a=007>.
- [73] ATLAS Collaboration, “The ATLAS Simulation Infrastructure,” *The European Physical Journal C*, Vol. 70, No. 3, Dec 2010, pp. 823–874, <https://doi.org/10.1140/epjc/s10052-010-1429-9>.

- [74] ATLAS Collaboration, “A measurement of the calorimeter response to single hadrons and determination of the jet energy scale uncertainty using LHC Run-1 pp-collision data with the ATLAS detector,” *The European Physical Journal C*, Vol. 77, No. 1, Jan 2017, pp. 26, <https://doi.org/10.1140/epjc/s10052-016-4580-0>.
- [75] Baur, U., Hinchliffe, I., and Zeppenfeld, D., “Excited Quark Production at Hadron Colliders,” *Int. J. Mod. Phys.*, Vol. A2, 1987, pp. 1285.
- [76] Mohapatra, R. N., “Supersymmetric grand unification,” *Supersymmetry, supergravity and supercolliders. Proceedings, Theoretical Advanced Study Institute in elementary particle physics, TASI’97, Boulder, USA, June 2-27, 1997*, 1997, pp. 601–657.
- [77] Durkin, L. S. and Langacker, P., “Neutral Current Constraints on Heavy Z Bosons,” *Phys. Lett.*, Vol. 166B, 1986, pp. 436–442.
- [78] Del Aguila, F., “The Physics of z-prime bosons,” *Acta Phys. Polon.*, Vol. B25, 1994, pp. 1317–1336.
- [79] Aguila, F. D., Quirs, M., and Zwirner, F., “Detecting E6 neutral gauge bosons through lepton pairs at hadron colliders,” *Nuclear Physics B*, Vol. 287, 1987, pp. 419 – 456, <http://www.sciencedirect.com/science/article/pii/0550321387901131>.
- [80] Altarelli, G., Mele, B., and Ruiz-Altaba, M., “Searching for New Heavy Vector Bosons in  $p\bar{p}$  Colliders,” *Z. Phys.*, Vol. C45, 1989, pp. 109, [Erratum: *Z. Phys.*C47,676(1990)].
- [81] UA1 Collaboration, “Measurement of the inclusive jet cross section at the CERN pp collider,” *Physics Letters B*, Vol. 172, No. 3, 1986, pp. 461 – 466, <http://www.sciencedirect.com/science/article/pii/037026938690290X>.
- [82] UA1 Collaboration, “Two-jet mass distributions at the CERN proton-antiproton collider,” *Physics Letters B*, Vol. 209, No. 1, 1988, pp. 127 – 134, <http://www.sciencedirect.com/science/article/pii/0370269388918436>.
- [83] CDF Collaboration, “Two-jet invariant mass distribution at  $\sqrt{s} = 1.8$  TeV,” *Phys. Rev. D*, Vol. 41, Mar 1990, pp. 1722–1725, <https://link.aps.org/doi/10.1103/PhysRevD.41.1722>.
- [84] Alitti, J. et al., “A Measurement of two jet decays of the  $W$  and  $Z$  bosons at the CERN  $p\bar{p}$  collider,” *Z. Phys.*, Vol. C49, 1991, pp. 17–28.
- [85] CDF Collaboration, “Search for quark compositeness, axigluons, and heavy particles using the dijet invariant mass spectrum observed in  $pp^-$  collisions,”

- Phys. Rev. Lett.*, Vol. 71, Oct 1993, pp. 2542–2546, <https://link.aps.org/doi/10.1103/PhysRevLett.71.2542>.
- [86] UA2 Collaboration, “A search for new intermediate vector bosons and excited quarks decaying to two-jets at the CERN pp collider,” *Nuclear Physics B*, Vol. 400, No. 1, 1993, pp. 3 – 22, <http://www.sciencedirect.com/science/article/pii/0550321393903956>.
- [87] CDF Collaboration, “Search for New Particles Decaying to Dijets in  $p\bar{p}$  Collisions at  $\sqrt{s} = 1.8$  TeV,” *Phys. Rev. Lett.*, Vol. 74, May 1995, pp. 3538–3543, <https://link.aps.org/doi/10.1103/PhysRevLett.74.3538>.
- [88] CDF Collaboration, “Search for new particles decaying to dijets at CDF,” *Phys. Rev. D*, Vol. 55, May 1997, pp. R5263–R5268, <https://link.aps.org/doi/10.1103/PhysRevD.55.R5263>.
- [89] DØ Collaboration, “Search for new particles in the two-jet decay channel with the DØ detector,” *Phys. Rev. D*, Vol. 69, Jun 2004, pp. 111101, <https://link.aps.org/doi/10.1103/PhysRevD.69.111101>.
- [90] CDF Collaboration, T. Aaltonen et al., “Search for new particles decaying into dijets in proton-antiproton collisions at  $\sqrt{s} = 1.96$  TeV,” *Phys. Rev. D*, Vol. 79, Aug 2009, pp. 112002.
- [91] ATLAS Collaboration, “Search for New Particles in Two-Jet Final States in 7 TeV Proton–Proton Collisions with the ATLAS Detector at the LHC,” *Phys. Rev. Lett.*, Vol. 105, 2010, pp. 161801.
- [92] Khachatryan, V. et al., “Search for Dijet Resonances in 7 TeV pp Collisions at CMS,” *Phys. Rev. Lett.*, Vol. 105, 2010, pp. 211801.
- [93] ATLAS Collaboration, “A search for new physics in dijet mass and angular distributions in  $pp$  collisions at  $\sqrt{s} = 7$  TeV measured with the ATLAS detector,” *New J. Phys.*, Vol. 13, 2011, pp. 053044.
- [94] CMS Collaboration, “Search for Resonances in the Dijet Mass Spectrum from 7 TeV  $pp$  Collisions at CMS,” *Phys. Lett. B*, Vol. 704, 2011, pp. 123.
- [95] ATLAS Collaboration, “Search for New Physics in the Dijet Mass Distribution using  $1 \text{ fb}^{-1}$  of  $pp$  Collision Data at  $\sqrt{s} = 7$  TeV collected by the ATLAS Detector,” *Phys. Lett.*, Vol. B708, 2012, pp. 37–54.
- [96] ATLAS Collaboration, “Search for new phenomena in the dijet mass distribution using  $pp$  collision data at  $\sqrt{s} = 8$  TeV with the ATLAS detector,” *Phys. Rev. D*, Vol. 91, 2015, pp. 052007.
- [97] CMS Collaboration, “Search for resonances and quantum black holes using dijet mass spectra in proton-proton collisions at  $\sqrt{s} = 8$  TeV,” *Phys. Rev.*, Vol. D91, No. 5, 2015, pp. 052009.

- [98] ATLAS Collaboration, “Search for New Phenomena in Dijet Mass and Angular Distributions from  $pp$  Collisions at  $\sqrt{s} = 13$  TeV with the ATLAS Detector,” *Phys. Lett. B*, Vol. 754, 2016, pp. 302.
- [99] Khachatryan, V. et al., “Search for narrow resonances decaying to dijets in proton-proton collisions at  $\sqrt{s} = 13$  TeV,” *Phys. Rev. Lett.*, Vol. 116, No. 7, 2016, pp. 071801.
- [100] CMS Collaboration, “Search for dijet resonances in proton-proton collisions at  $\sqrt{s} = 13$  TeV and constraints on dark matter and other models,” *Phys. Lett. B*, 2017.
- [101] “Searches for dijet resonances in pp collisions at  $\sqrt{s} = 13$  TeV using data collected in 2016.” Tech. Rep. CMS-PAS-EXO-16-056, CERN, Geneva, 2017, <http://cds.cern.ch/record/2256873>.
- [102] Choudalakis, G., “On hypothesis testing, trials factor, hypertests and the BumpHunter,” 2011.
- [103] James, F. and Roos, M., “MINUIT-a system for function minimization and analysis of the parameter errors and correlations,” *Comput. Phys. Commun.*, Vol. 10, No. 6, 1975, pp. 343–67, <http://cds.cern.ch/record/873119>.
- [104] Nelder, J. A. and Mead, R., “A Simplex Method for Function Minimization,” *The Computer Journal*, Vol. 7, No. 4, 1965, pp. 308–313, <http://dx.doi.org/10.1093/comjnl/7.4.308>.
- [105] Davidon, W. C., “Variable Metric Method for Minimization,” *SIAM Journal on Optimization*, Vol. 1, No. 1, 1991, pp. 1–17, <https://doi.org/10.1137/0801001>.
- [106] Wilks, S. S., “The Large-Sample Distribution of the Likelihood Ratio for Testing Composite Hypotheses,” *Ann. Math. Statist.*, Vol. 9, No. 1, 03 1938, pp. 60–62, <https://doi.org/10.1214/aoms/1177732360>.
- [107] Gross, E. and Vitells, O., “Trial factors for the look elsewhere effect in high energy physics,” *Eur. Phys. J.*, Vol. C70, 2010, pp. 525–530.
- [108] ATLAS Collaboration, “Selection of jets produced in 13TeV proton-proton collisions with the ATLAS detector,” Tech. Rep. ATLAS-CONF-2015-029, CERN, Geneva, Jul 2015, <http://cds.cern.ch/record/2037702>.
- [109] Carrazza, S., Forte, S., and Rojo, J., “Parton Distributions and Event Generators,” *Proceedings, 43rd International Symposium on Multiparticle Dynamics (ISMD 13)*, 2013, pp. 89–96, <https://inspirehep.net/record/1266070/files/arXiv:1311.5887.pdf>.

- [110] ATLAS Collaboration, “ATLAS Run 1 Pythia8 tunes,” Tech. Rep. ATLAS-PHYS-PUB-2014-021, CERN, Geneva, Nov 2014, <https://cds.cern.ch/record/1966419>.
- [111] ATLAS Collaboration, “The ATLAS Simulation Infrastructure,” *The European Physical Journal C*, Vol. 70, No. 3, Dec 2010, pp. 823–874, <https://doi.org/10.1140/epjc/s10052-010-1429-9>.
- [112] “Geant4a simulation toolkit,” *Nuclear Instruments and Methods in Physics Research Section A: Accelerators, Spectrometers, Detectors and Associated Equipment*, Vol. 506, No. 3, 2003, pp. 250 – 303, <http://www.sciencedirect.com/science/article/pii/S0168900203013688>.
- [113] ATLAS Collaboration, “Search for low mass dijet resonances using trigger-level jets with the ATLAS detector in LHC pp collisions at  $\sqrt{s}=13$  TeV,” Tech. Rep. ATLAS-COM-PHYS-2017-415, CERN, Geneva, Apr 2017, <https://cds.cern.ch/record/2261055>.
- [114] ATLAS Collaboration, “Search for resonances in the di-jet mass distribution with one or two jets identified as  $b$ -jets in proton-proton collisions at  $\sqrt{s}=13$  TeV with the ATLAS detector,” Tech. Rep. ATLAS-COM-PHYS-2016-1561, CERN, Geneva, Nov 2016, <https://cds.cern.ch/record/2229034>.
- [115] ATLAS Collaboration, “Search for low-mass dijet resonances using trigger-level jets with the ATLAS detector in  $pp$  collisions at  $\sqrt{s}=13$  TeV,” 2018.